EFFECTS OF OFF-AXIS LOADING ON THE TIBIA'S FRACTURE RISK

THE EFFECTS OF OFF-AXIS LOADING ON FRACTURE RISK IN THE HUMAN TIBIA

By AVERY B. CHAKRAVARTY, B.Eng.

A Thesis Submitted to the School of Graduate Studies in Partial Fulfilment of the Requirements for the Degree of Master of Applied Sciences

McMaster University Master of Applied Science (2016) Hamilton, Ontario (Mechanical Engineering)

TITLE: THE EFFECTS OF OFF-AXIS LOADING ON FRACTURE RISK IN THE HUMAN TIBIA

AUTHOR: Avery B. Chakravarty, B.Eng.

SUPERVISOR: Cheryl E. Quenneville, B.Sc., M.Sc., Ph.D.

NUMBER OF PAGES: xvi, 162

Lay Abstract

Fractures of the tibia (the shin bone) are common in automotive collisions, and often lead to long-term impairment. Experimental studies on these kinds of injuries are usually performed with the lower leg aligned with the direction of impact, which does not reflect the range of postures an occupant may assume during a crash.

Cadaveric tibias were subjected to impact loading in two different postures. It was found that the specimens held further from an axial posture sustained fractures at lower forces. Two commonly-used crash test dummy legs were also impacted in these non-standard postures to test their performance. Suggestions were made for new load limits to be used with these devices in non-standard postures.

The finding that leg posture has an effect on injury risk in the tibia can be used in the future to design and evaluate better protective devices and ultimately reduce the incidence of these injuries.

Abstract

The tibia is a frequent site of injury in frontal automotive collisions. The bulk of experimental cadaveric studies on injury tolerance assume load is applied in line with the leg's long axis, leaving non-standard postures largely uninvestigated. The purpose of this work was to study the effects of non-standard postures on the tibia's injury tolerance.

A pneumatic system was designed to facilitate impact testing. This system allows the user to fire a projectile of variable mass towards a specimen at a range of velocities by varying the supplied air pressure. Impact tests were performed using pairs of isolated cadaveric tibias. Within each pair of specimens, two postures were compared by varying the angle of the bone's long axis relative to the direction of impact, representing knee extension and corresponding plantarflexion. It was found that the specimens held further from the axial posture sustained injury at lower forces. Two commonly-used Anthropomorphic Test Device legforms were impacted in these non-standard postures. New load limits were proposed for the use of these devices in off-axis impact testing.

In order to compare directly with the loads measured by the legforms, it was necessary to measure forces and moments internal to the bone's long axis. A non-invasive load estimation method was developed and tested using strain measured from the surface of four specimens. The method performed poorly under impact conditions, but may be refined in the future.

Quantifying the effect of posture on injury risk in the tibia allows for the refinement of existing injury criteria. Ultimately, this can be used to enhance the design of protective devices to reduce the incidence of tibia fractures in automotive collisions.

Acknowledgements

Firstly, I would like to thank my advisor, Dr. Cheryl Quenneville, for her mentorship and unparalleled optimism. I was always in awe of her ability to come up with creative solutions in the face of an unexpected setback, and I hope some of that skill has rubbed off on me.

I am eternally indebted to everyone who has ever helped with the test apparatus. Ron, Mark, Mike, and John in the machine shop were incredibly helpful and always patient with my seemingly endless conundrums. Thanks are due to my labmates, who all got roped into trouble-shooting, upgrades, repairs, or just listening to me vent at some point or another: Chris, Alberto, Clodagh, Ishan, Fatemeh, and Muir. I definitely owe Alberto a shawarma for putting in many long testing days and for handling the electronics.

Outside of the lab, I could always count on support from Rani, my best friend. She never hesitated to offer advice or dinner, and I am grateful for both. And from just one cubicle over, Omar inspired me with his patience and kindness.

Without my family— Mom, Jordan, and Alex— none of this would have been possible. They kept me positive during the hard times and always took an interest in my project, down to the finest details. Thanks to Alex for the brainstorming sessions, to Mom for being my cheerleader and role model since day one, and to Jordy for making me laugh when I needed it most.

Lastly, I must acknowledge McMaster University for funding me and giving me the opportunity to pursue graduate studies.

Table of Contents

List of Figures

List of Tables

List of Abbreviations and Symbols

%	Percent
”	Inch
±	Plus/minus
∥	Parallel
⊥	Perpendicular
°	Degree
A_{CS}	Cross-sectional area
AL	Anterolateral
AM	Anteromedial
AP	Anterior-posterior
ATD	Anthropomorphic Test Device
c	Perpendicular distance from a given point to the neutral axis
cm	Centimetre
CT	Computed Tomography
d_{NA}	Perpendicular distance from geometric centroid to neutral axis
E	Elastic modulus
F	Force
F_c	Critical Force
g	Gram
GPa	Gigapascals
I	Area moment of inertia
kg	Kilogram
kPa	Kilopascals
m	Metre
L	Litre
M	Moment
M_c	Critical moment
min	Minute
ML	Medial-lateral
mm	Millimetre
ms	Millisecond

NA	Neutral axis
P	Posterior
R^2	Coefficient of determination
s	Second

Declaration of Academic Achievement

The following is a declaration that the research described in this thesis was completed by Avery Chakravarty and recognises the contributions of Dr. Cheryl Quenneville, Sandra Charbonneau, and Alberto Martinez. Avery Chakravarty contributed to the study design, and was responsible for the experimental testing protocols, modification and installation of components to support experimental testing, data collection, data analysis, and writing of the manuscript. Dr. Cheryl Quenneville assisted with the study design and review of the manuscript. Sandra Charbonneau took the CT scans of the specimens, and Alberto Martinez assisted with experimental testing.

Chapter 1: Introduction

1.1 Motivation

Fractures of the lower leg and foot are a frequent occurrence in automotive collisions. Frontal collisions account for the majority (71%) of severe injuries in this region, and these injuries are caused predominantly by contact with the instrument panel and loads delivered through the floor (Huelke *et al*. 1982). While these injuries may not be life-threatening, they can cause long-term impairment, with one study reporting that 33% of patients who had suffered a severe injury in an extremity had difficulty performing self-care tasks a year after leaving the hospital (MacKenzie *et al.* 1988). These injuries often result in longer periods of disability and longer hospital stays than severe injuries sustained in other parts of the body (Huelke *et al.* 1982).

The incidence rate and consequences of these injuries has inspired a great deal of experimental work to be conducted on the injury tolerance of this body region. "Injury tolerance" refers to the critical limits of loading under which injury will not occur in a particular region of the body (Viano & King 2008). Knowing these limits can guide the design of protective devices or reveal which parts of the body are at the highest risk.

To determine the injury tolerance of a particular body segment, loads of incrementally increasing magnitude can be applied experimentally to the segment in question until injuries are produced. For practical and ethical reasons, these experiments are carried out on cadavers or other surrogates for living human subjects.

The bulk of the experimental cadaveric work on the lower extremity has looked at the intact limb, and has delivered loads to the plantar surface of the foot along the axis of the lower leg. Using whole limbs introduces a high degree of complexity that may be realistic, but makes it difficult to determine the load path within the specimen, meaning that the proportion of load taken up by a given bone as well as that dissipated by soft tissue deformation and joint articulation is difficult to quantify. Directing load axially to assess injury also does not take into account the range of postures that a person may assume while seated in an automobile due to variation in height and vehicle design, and the effects of off-axis loading compared to axial loading have not been well quantified.

Another important tool in the study of injury mechanics is the Anthropomorphic Test Device (ATD), also known as the crash test dummy. ATDs come with pre-installed instrumentation to measure loads in body segments of interest, and may represent the geometry of different populations. ATDs, being stronger and stiffer than cadaveric specimens, do not fracture under conditions that would produce injury *in vivo*. Therefore, standard load limits have to be determined, and these limits must be specific to the model of ATD used and the type of testing being performed. The Tibia Index (Mertz 1993) is an injury criterion that calculates risk based on axial force and moments measured in an ATD test. The problem with calculating risk this way is that it relies on being able to measure analogous forces and moments in a cadaveric test, which can be challenging due to the complex material properties and geometry of the specimens. Some groups have suggested that strains measured at the surface of an intact cadaveric bone may be correlated to loads experienced by a long bone (Funk & Crandall, 2006; Henderson *et al.*

2013; Untaroiu *et al.* 2007). Measuring strain using strain gauges may one day be seen as a non-invasive alternative to implanting a load cell into a cadaveric specimen, although none of the experimental methodologies described in the published literature has yet been proven accurate enough to warrant widespread adoption.

The Hybrid III-50th Percentile ATD (Humanetics, Plymouth, MI, USA) is a commonly used device for assessing safety in automotive collisions, and has been used experimentally in a range of test configurations. This range of configurations includes off-axis impacts (van der Horst *et al.* 2005). Despite being developed for automotive tests, it has been used in evaluating risk during anti-vehicular mine blasts, which tend to occur over shorter durations and at higher velocities than automotive collisions (McKay & Bir 2009). Because of concerns over the Hybrid-III's applicability to these scenarios, Humanetics has introduced the MIL-LX legform. However, the MIL-LX has yet to be evaluated under off-axis impacts.

The goals of this work were to investigate a relationship between non-standard postures and injury risk in the tibia under conditions representative of a frontal automotive collision, to evaluate the performance of the Hybrid-III and MIL-LX legforms in these non-standard postures, and to develop a strain-based method of non-invasively estimating internal loads in cadaveric specimens.

1.2 Anatomy of the Lower Leg

The lower leg refers to the segment of the body distal to the knee, comprising the shank, ankle, and foot.

The lower leg is comprised of two main long bones: the tibia and the fibula (Figure 1-1). Both extend the length of the shank, but the tibia has a much larger cross section and takes up a higher proportion of the load (estimated as 94% of axial leg load when the ankle is in a neutral posture, although this may vary with ankle eversion or inversion) (Funk *et al.* 2004). The tibia runs along the medial side of the leg and the fibula runs along the lateral side.

The ankle is a region between the shank and foot and incorporates four bones: the talus (which lies directly inferior to the tibia and fibula), the calcaneus (the heel bone of the foot), the tibia, and the fibula. The ankle is made of three joints: the talocrural joint (between the distal tibia and the talus), the subtalar joint (between the talus and the calcaneus), and the inferior tibiofibular joint (between the tibia and the fibula).

The foot is a complex structure that extends from the ankle joints to the toes. It is comprised of 26 bones, including the talus, calcaneus, cuneiforms, cuboid, navicular, metatarsals, and phalanges.

1.2.1 Anatomy of the Tibia

Like other long bones (*e.g.* the femur, the humerus), the tibia has two rounded ends or epiphyses and a long central shaft or diaphysis. The tibia interfaces directly with the femur at the knee, with its proximal articular surface being called the tibial plateau. At the distal end, called the plafond, it articulates with the talus at the ankle. Along the anterior border of the diaphysis is the anterior crest. The medial and lateral borders are less prominent than this ridge.

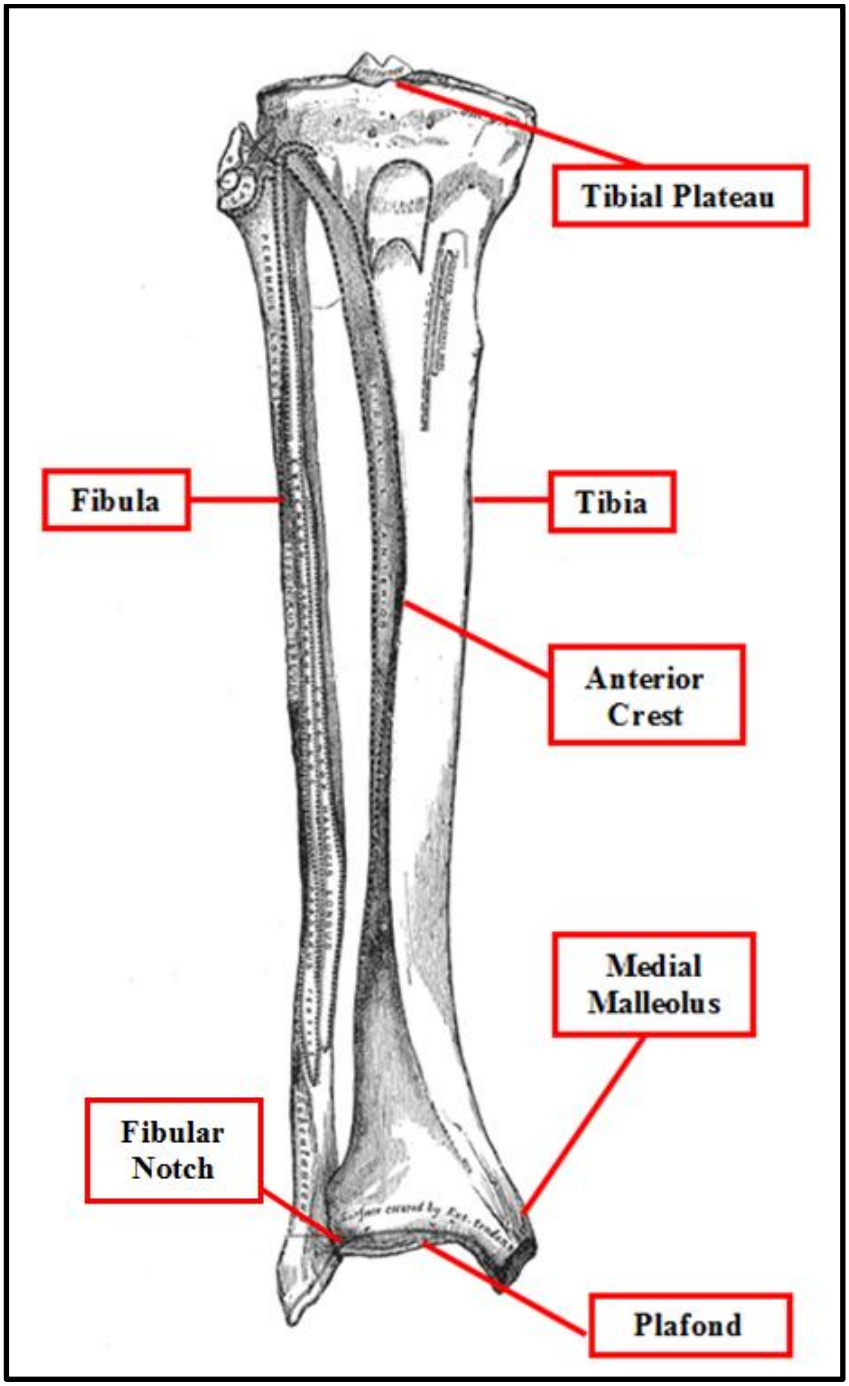

Figure 1-1: Anatomy of the Tibia and Fibula
The tibia and fibula are illustated, with their key anatomical landmarks highlighted. Adapted from (Gray 1918)**.**

The geometry at the inferior articular surface is roughly quadrilateral and concave, in order to articulate with the convex superior surface of the talus. There is a protrusion, the medial malleolus, which rests against the medial process of the talus, and serves as a ligament attachment site. The tibia's distal articular surface interfaces with the fibula at the fibular notch.

1.2.2 Anatomy of the Tibia

Like other long bones (*e.g.* the femur, the humerus), the tibia has two rounded ends or epiphyses and a long central shaft or diaphysis. The tibia interfaces directly with the femur at the knee, with its proximal articular surface being called the tibial plateau. At the distal end, called the plafond, it articulates with the talus at the ankle. Along the anterior border of the diaphysis is the anterior crest. The medial and lateral borders are less prominent than this ridge.

The geometry at the inferior articular surface is roughly quadrilateral and concave, in order to articulate with the convex superior surface of the talus. There is a protrusion, the medial malleolus, which rests against the medial process of the talus, and serves as a ligament attachment site. The tibia's distal articular surface interfaces with the fibula at the fibular notch.

1.2.3 Bone Structure and Material Properties

Bone is known to be challenging to characterize mechanically. It is inhomogeneous, and in terms of structure may be categorized as either cortical (also known as compact) or cancellous (also known as trabecular or spongy). Cortical bone is dense and composed of cylindrical functional units called osteons. It makes up the

diaphyses of long bones as well as covering the epiphyses of long bones. The osteons themselves are made of concentric ring-like or lamellar layers.

Cancellous bone is a highly porous material that is present in the epiphyses of long bones. Its structure is quite complex, being made up of an intricate network of rods and plates of bone. The porosity, the diameters of the rods, and the thickness of the plates all vary depending on the location of the sample taken (Singh 1978). Both cortical and cancellous bone have been shown to be viscoelastic and anisotropic, and their mechanical properties are dependent on their age (as bone is remodelled throughout life) and composition (as both are comprised largely of collagen fibers and apatite crystals). Cancellous bone specifically has properties that are highly dependent on its porosity (Rho *et al.* 1998).

1.3 Review of Previous Lower Leg Impact Studies

1.3.1 Axial Impact Studies

Several studies have been performed on the lower leg's axial tolerance to injury. These studies considered the lower leg as a whole, using intact lower limbs amputated at mid-femur or disarticulated at the knee. These studies used experimental apparatuses in various configurations to deliver load to a cadaveric specimen. The mechanisms used to apply load include pendulums, linear pistons, drop hammers, and projectiles.

One of the most widely-cited studies in the field was performed by Yoganandan *et al.* (1996). The specimens used were intact lower legs and feet, disarticulated at the knee and potted at the proximal tibia. Three sets of experimental data were brought together

(comprising tests on 52 specimens in total), but all experiments involved delivering load to the plantar surface of the foot with the ankle in a neutral posture, either via a pendulum (Figure 1-2a), pneumatic piston, or constant velocity loading device. The pendulum tests were conducted such that impact velocity was 7, 10, or 12 m/s, and the constant velocity loading device was set to 4.6 m/s for all specimens. Details of the impact conditions were not given for the pneumatic piston set. The results of these tests were used to develop injury risk curves based on a Weibull distribution with donor age and axial force highlighted as the major predictors of injury risk. Injury, here, included any fracture of the foot-ankle complex. Extra/intra-articular fractures of the distal tibia and calcaneus were noted, and the forces required for fracture ranged from 4.3 to 13.0 kN for all tests analysed. The Weibull analysis revealed that the risk of fracture for a 45-year-old male reached 50% at an axial load of 8.0 kN, while this value was 6.2 kN for a 65-year-old male. A risk curve for the 45-year-old specimen was used to extract injury risk limits that have been taken for use in the safety standard for occupant protection in military vehicles (an axial tibia force of 5.4 kN, corresponding to 10% injury risk) (NATO 2007) and that have been cited in determining acceptable limits in crash tests (Kuppa & Wang 2001).

The effects of muscle forces on injury tolerance under an axial impact configuration were investigated by Funk *et al.* (2002). Forty-three lower limbs were sectioned at mid-femur and installed in a linear impact test apparatus similar to the aforementioned pendulum device at 5 m/s. In 22 of the tests, tension (ramping up to a maximum load of either 1.7 or 2.6 kN) was applied to the Achilles tendon via a custom tendon gripping device in order to simulate the effects of sudden breaking. In all

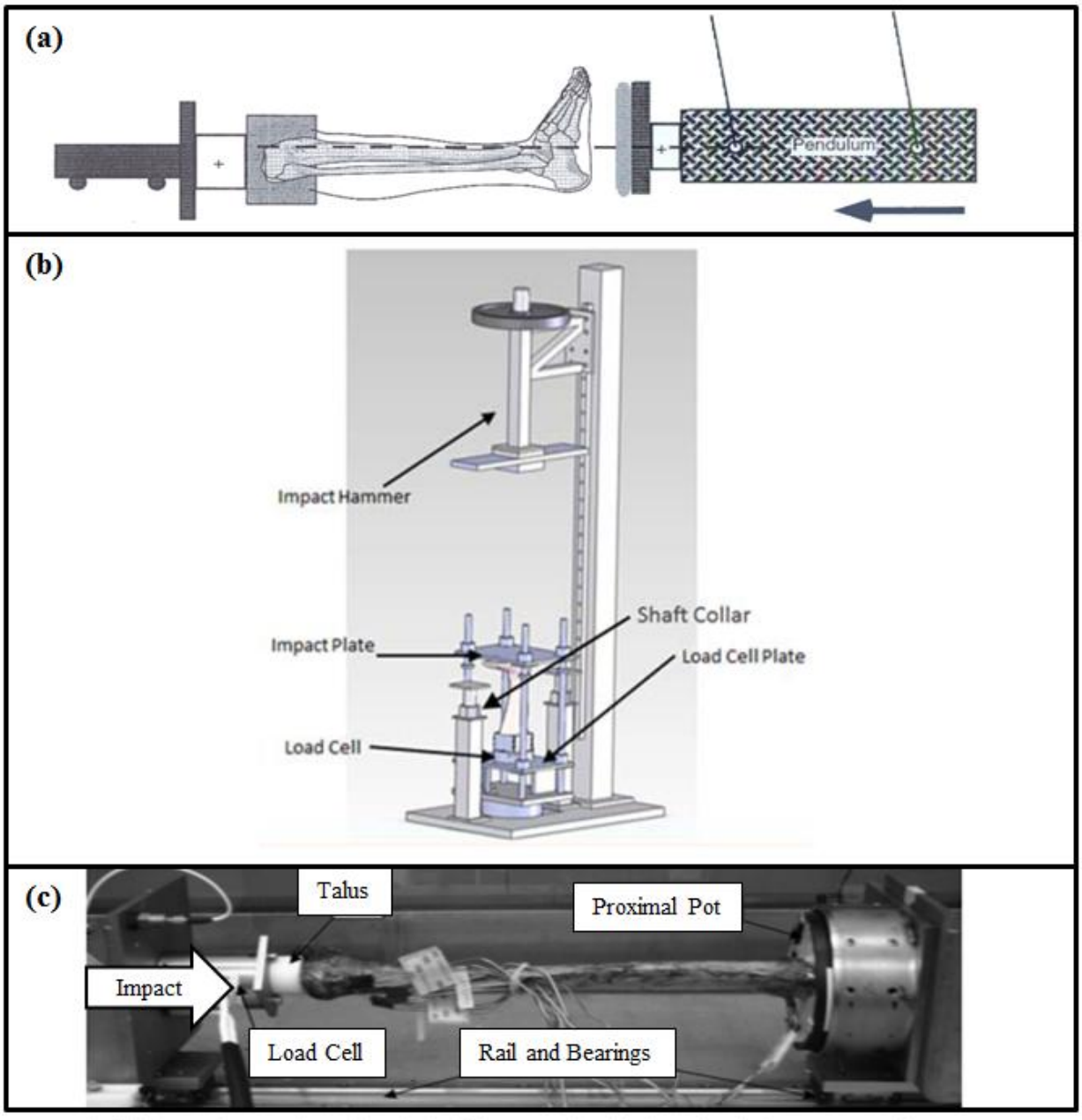

Figure 1-2: Test Set-Ups for Axial Impact Studies
(a) Pendulum apparatus used by Yoganandan *et al.* to deliver load to a cadaveric lower leg and foot (Yoganandan *et al.* 1996). (b) The drop tower apparatus is shown in detail, with the impacting hammer, impact plate, and specimen identified (Henderson *et al.* 2013). (c) The isolated tibia is shown, aligned axially with the line of impact. Impulse was delivered by a pneumatically-propelled projectile that lies outside the frame of the photograph (Quenneville *et al.* 2011).

specimens, a 9-centimeter portion of the tibial diaphysis was removed to install a five-axis load cell that measured forces and moments directly in line with the leg. Pre-compression was applied to the lower leg to simulate proximal musculature.

The effects of muscle forces on injury tolerance under an axial impact configuration were investigated by Funk *et al.* (2002). Forty-three lower limbs were sectioned at mid-femur and installed in a linear impact test apparatus similar to the aforementioned pendulum device at 5 m/s. In 22 of the tests, tension (ramping up to a maximum load of either 1.7 or 2.6 kN) was applied to the Achilles tendon via a custom tendon gripping device in order to simulate the effects of sudden breaking. In all specimens, a 9-centimeter portion of the tibial diaphysis was removed to install a five-axis load cell that measured forces and moments directly in line with the leg. Pre-compression was applied to the lower leg to simulate proximal musculature, and then impacts were delivered at a load level expected to cause injury. Fractures were produced in most tests, with the calcaneus being the most frequent site of injury (25 fractures produced in this bone). Only 11 of the specimens sustained tibial fractures, which included fractures of the plafond and medial malleolus (not including artefactual fractures at the interface of the bone and the implanted load cell). It was found that incorporating Achilles tension increased the peak axial tibia force measured at fracture, indicating that active braking worked to protect the specimen to a degree.

Henderson *et al.* (2013) used a drop tower to deliver load to cadaveric lower legs disarticulated at the knee (Figure 1-2b). The authors investigated the effects of the relatively shorter intrusion stroke that is associated with high-acceleration/short-duration

impacts when compared with automotive collision loading. Different hammer masses, drop heights, and impact plate materials were used to vary the load characteristics. Twenty tests were performed, with injury produced in 14 (11 with calcaneal fractures and three with fractures of the distal tibia). An effective strain-rate-dependent modulus for the distal tibia was calculated in each test based on readings from strain gauges placed on the surface of the bone. The authors concluded that the rate of loading played a large role in fracture mechanics and that high-rate loading leads to a stiffening of the bone. Therefore, choosing a realistic loading rate for experimental simulation affects the applicability of the experimental results to real life scenarios.

While the bulk of previous experimental cadaveric studies made use of intact lower limbs, producing mostly calcaneal and talar fractures, Quenneville *et al.* (2011) chose to study the tibia's response to impact in isolation (Figure 1-2c) to reduce the degrees of freedom and to simplify alignment as compared with tests conducted on whole lower legs. Short-duration (3.7 ms on average) axial impacts were delivered via a pneumatically-propelled projectile (either 3.9 or 6.8 kg in mass) to the distal articular surface of 14 cadaveric tibias at velocities that ranged from 3.8 to 9.4 m/s, while the specimen was free to translate on linear rails after each strike. The average force to produce intra-articular fracture in this work was 12.6 kN, and the Weibull curve produced from the findings showed a higher force tolerance than studies conducted over longer durations and lower velocities, suggesting that these parameters have an effect on injury risk.

1.3.2 Evaluation of Non-Standard Postures

While the bulk of experimental work has been done in an axial configuration, non-standard postures have been investigated for their role in injury mechanics as well. A study of the range of motion in the hip, knee, and ankle joints of 96 healthy, adult men found that the subjects' mean range of dorsiflexion was 15.3°, while the range of plantarflexion was 40°. Eversion could be performed up to mean angles of 28°, while inversion could be performed up to mean angles of 28° (Roaas & Andersson 1982).

Crandall *et al.* (1998) performed a study in which initial ankle posture during a frontal collision was investigated for its contribution to injury risk. Fifty cadaveric lower limbs were used. Specimens were amputated at mid-femur and installed in a test apparatus that simulated the hip joint, allowing for realistic rotation of the thigh during impact. Nine centimeters of the tibial diaphysis were removed to make room for an *in situ* load cell used to measure axial leg forces. Impacts were delivered via a pendulum of variable mass (9 to 27 kg) at velocities of 6 to 7 m/s (Figure 1-3a). Load was delivered normal to the plantar surface of the foot. The hip centre's location (and, consequently, the femur and tibia's angles) could be adjusted to achieve the desired ankle posture. Injury was produced in 13 cases, 10 of which included bony fractures. Seven of these were calcaneal or talar fractures, and three were fractures of the tibia. The effect of initial ankle position in terms of plantarflexion/dorsiflexion and eversion/inversion was investigated, and it was determined that an initially dorsiflexed ankle was less prone to injury than one initially held in a neutral posture, possibly due to increased contact area at the ankle joint between the tibia and talus.

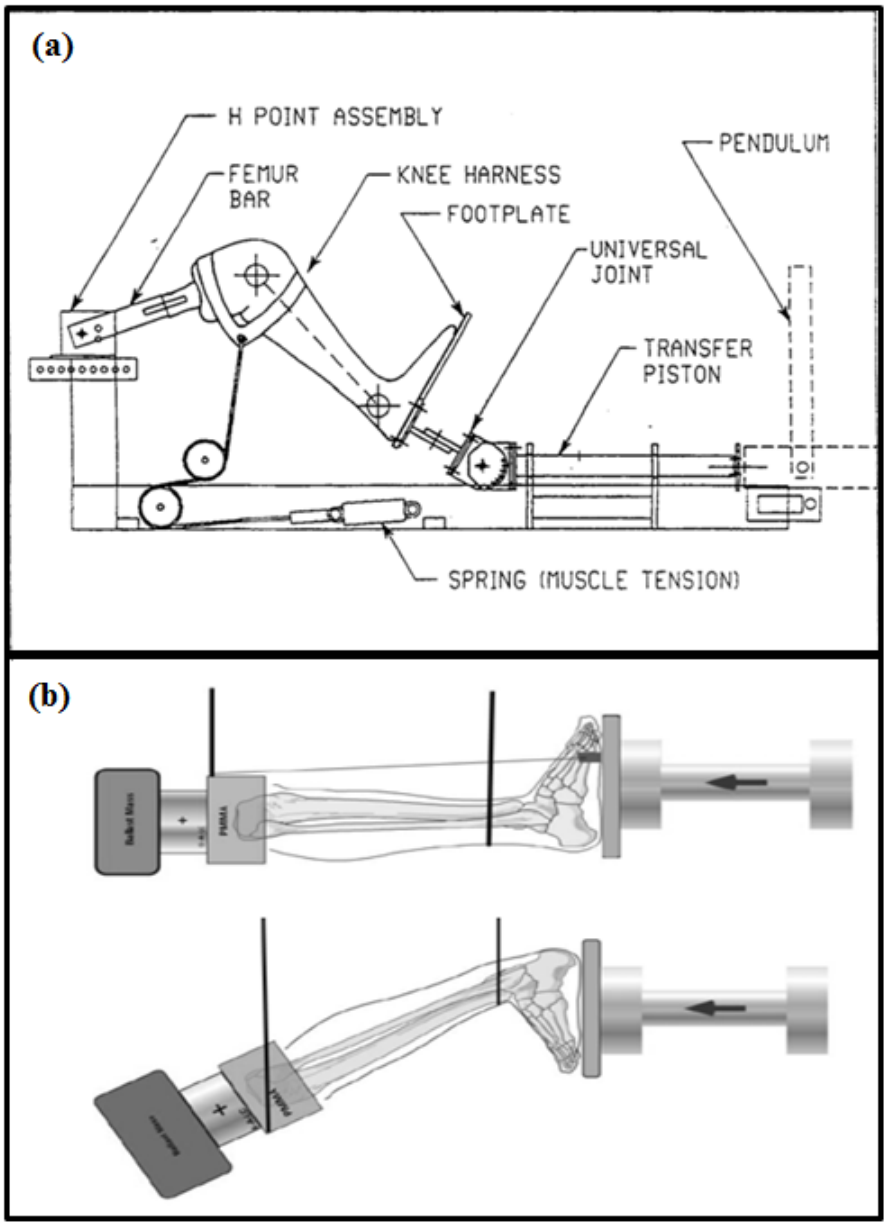

Figure 1-3: Test Set-Ups for Non-Standard Posture Studies
Test apparatuses used to simulate the loading on the lower limb typical of a frontal collision in non-standard postures. (a) Linear impacting apparatus incorporating a joint allowing the adjustment of thigh and shank angles (Crandall *et al.* 1998). (b) Pendulum set-up used to strike the specimen in a neutral posture as well as in 20° of dorsiflexion (Gallenberger *et al.* 2013).

Another investigation into initial ankle posture was conducted by Gallenberger *et al.* (2013). A linear pendulum was used to strike a cadaveric lower limb disarticulated at the knee in two different postures: neutral and 20° of dorsiflexion, with dorsiflexion achieved by changing the lower leg's angle relative to the direction of impact (Figure 1-3b). Fifteen specimens were used, with each specimen impacted between two and seven times, for a total of 60 impacts (19 in dorsiflexion). Injuries were sustained in 14 of the 15 specimens, and all injured specimens included some damage to the calcaneus. Two specimens also sustained a tibial plafond fracture.

The data gathered from these tests were used to generate Weibull injury risk functions. These functions indicated that the force required to generate a 50% risk of injury in the dorsiflexed specimen (7.9 kN) was higher than the same force in the neutral specimen (6.8 kN). Again, increased contact area in the ankle during dorsiflexion is identified as the likely cause of this difference.

Due to the numerous challenges associated with experimental cadaveric work, computational models are an attractive alternative for studying posture-specific injury mechanics. Hardin *et al.* (2004) created a two-dimensional musculoskeletal model of the driver of a vehicle during a frontal collision. Active muscle forces representative of those generated during braking were simulated. It was found that increasing the occupant's initial knee flexion angle would increase loading to the hindfoot and ankle joint, and that less knee flexion during braking was deemed to provide better protection against plafond fractures.

A finite element model developed by Dong *et al.* (2013) investigated the effects of an anti-vehicular mine blasts on the human body. Lower leg posture relative to the direction of blast was varied, and it was found that the critical floor velocity required to cause a distal tibia fracture changed with occupant's knee angle. With the feet kept flat on the floor (normal to the direction of blast loading), increasing knee extension from the initial neutral 90° angle also increased the floor velocity required to produce a fracture, indicating that a non-standard posture decreased the risk of fracture. This is in line with the findings of Hardin *et al.* (2004).

The importance of posture has also been highlighted in the upper extremity. Troy and Grabiner (2007) generated a finite element model of the wrist and the loading typical of a fall onto the hands. It was found that varying the radius's orientation relative to the direction of impact had a significant effect on its fracture tolerance. An increased proportion of off-axis load reduced the magnitude of force that the bone was able to withstand before fracture by 47%, with higher bending moments identified as the likely culprit. While these results may not be directly applicable to the lower extremity due to variations between these two regions of the body, it is worth noting both the radius and tibia are long bones, and may respond similarly to bending loads versus axial compression.

1.3.3 Tibia Index

A widely-used injury criterion for the lower leg, the Tibia Index (TI) (Mertz 1993), expresses injury risk as a linear combination of compressive and bending loads measured by an ATD:

$$TI = \frac{F}{F_c} + \frac{M}{M_c} \qquad \textbf{Equation 1-1}$$

In this equation, F and M are the applied force and moment as measured by an ATD's load cell, and F_c and M_c are critical force and moment values, initially proposed by Mertz to be 35.9 kN and 225 Nm for a 50th percentile adult male and 22.9 kN and 115 Nm for a small (5th percentile) female. In the initial formulation, a TI value of 1 or greater corresponded to fracture risk. Due to concerns about the derivation of these critical loads, a Revised Tibia Index was suggested with critical values of 12 kN and 240 Nm for a 50th percentile male (Kuppa 2001). Both of these formulations were based on results from quasi-static mechanical tests of the tibia's strength at midshaft, with compression and bending being tested independently of one other.

It has been found that the natural curvature of the tibia can induce bending loads even when the leg is loaded axially (Funk *et al.* 2004). Multiple attempts have been made to reformulate the Tibia Index in order to account either for the curvature of a natural bone or for the unrealistic geometry of an ATD legform (Funk *et al.* 2004; Zuby 2001). It should be noted that none of the reformulations mentioned used specimens outside the typical 50th percentile male demographic, and that critical values for force and moment were not derived under dynamic conditions. Therefore, despite the frequent use of TI in injury studies, there is certainly potential for further reformulation, especially when conducting experiments in less commonly-used test configurations.Use of Anthropomorphic Test Devices

ATDs are commonly used experimentally to evaluate risk in simulated collisions (Figure 1-4). The Humanetics Hybrid III (Humanetics Innovative Solutions, Plymouth,

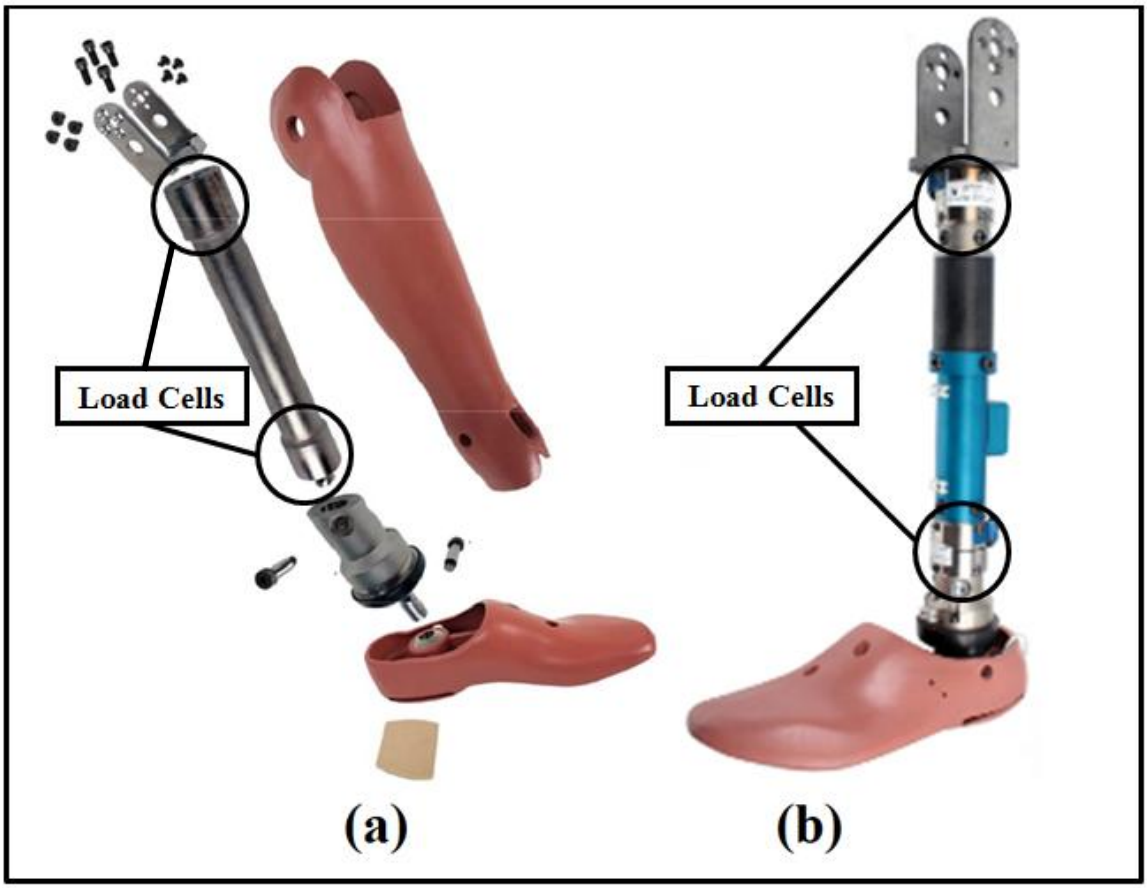

Figure 1-4: Humanetics Legforms
(a) Hybrid III-50th Percentile legform (adapted from Humanetics Innovative Solutions 2015a) and (b) MIL-LX legform (adapted from Humanetics Innovative Solutions 2015b).

MI, USA) dummy is the most commonly used in automotive studies. This device is available in different sizes representing different demographics, with the 50th-percentile male typically taken to represent the "average" occupant. The anthropometrics (including stature and weight) were taken based on those of the average adult American male between 1970 and 1980 (Carpanen *et al.* 2016).

The response of the Hybrid III to off-axis loading in non-standard postures has been both experimentally determined and computationally modelled by van der Horst *et al.* (2005). It was shown that the ATD measured lower forces in the axial direction when the knee was moved out of the standard 90° flexion posture, although load was still delivered normal to the foot's plantar surface. However, only one non-standard shank posture was evaluated, so it could not be determined if the magnitude of this difference was proportional to the extension angle chosen.

Based on concerns about the biofidelity of the Hybrid III's response to the high-rate loading typical of an anti-vehicular mine blast, Humanetics developed the MIL-LX. This legform includes a compliant element and geometric changes from the Hybrid III model that made it more suited to high-rate loading. While both legforms can be instrumented with upper and lower load cells, typically the measurement taken to evaluate the risk of injury comes from the lower tibia load cell in the Hybrid III legform and from the upper tibia load cell in the MIL-LX legform (Carpanen *et al.* 2016). The MIL-LX has been evaluated in seated versus standing posture, with the finding that the standing posture allows for higher peak forces (Newell *et al.* 2013). The legform, however, has not been evaluated in alternate seated postures as the Hybrid III has.

1.4 Use of Strain Gauges to Estimate Bone Loads

The need to experimentally measure loads in cadaveric specimens analogous to those sensed by load cells in an ATD has driven researchers to either implant a load cell into a long bone such as the tibia or to mount a load cell external to the specimen. For the implantation strategy, it is necessary to remove a section of the bone's diaphysis from a cadaveric specimen, fix the ends of the natural bone in a custom jig, and bolt the load cell in place (Funk *et al.* 2007; McKay & Bir, 2009; Rudd *et al.* 2004; Takebe *et al.* 1984). This alters the material properties and geometries of the specimen as a whole, and may introduce artefactual fractures at the site of implantation. Externally-mounted load cells offer a non-invasive alternative to this practice (Crandall *et al.* 1998; Quenneville *et al.* 2011; Yoganandan *et al.* 1996), but depending on the configuration of the specific experimental setup and the type of specimen used, the loads measured by these devices may not be equal to those experienced by a region of interest within the specimen.

An alternative is to find some way to estimate loads internal to the specimen non-invasively using strain data. There have been several previous attempts to mathematically model long bones such as the tibia as cantilever beams and to estimate forces and moments based on strain distribution. Using the beam approach, it should theoretically be possible to calculate internal stresses anywhere in the bone's diaphysis based on applied external loads, known material properties, and/or strain measured from the bone's surface.

1.4.1 Funk and Crandall, 2006

Funk and Crandall were the first in the literature to study strain as a predictor of internal loading in the human tibia under quasistatic bending and compression. They stated explicitly that the motivation for their work was to find a method to replace implanted load cells in cadaveric testing. They obtained two cadaveric lower legs and applied three rectangular strain gauge rosettes to the tibia at midshaft. Quasistatic axial compression tests were performed on the specimens by potting the foot and applying load up to 2000 N via the knee with the lower leg held vertical. After this, the tibias were removed from the lower leg, cleaned of soft tissues, and subjected to quasistatic four-point bending tests, to a maximum force of 700 N and moment of 28 Nm. All tests were non-injurious and performed at a rate of 10 mm/min. The elastic modulus of the bone was estimated based on the results of the bending tests, and it was noted that there was a linear relationship between the load applied and the strain measured by the gauges.

CT scans were taken of the specimens to quantify geometric properties such as the location of the centroid of the cross section at the level of the gauges and area moments of inertia about the centroidal axes. The location and orientation of the neutral axis was also estimated relative to the centroidal axes by assuming a linear strain profile throughout the cross section, interpolating between the gauges for three points of zero strain, and fitting a line through these points.

In the axial tests, it was assumed that a combination of bending and compression would actually be applied to the tibia's midshaft due to bone curvature and the difficulty of ensuring that the bone was aligned axially with load application within an intact lower

leg. Strain values were decomposed into bending and axial strains based on the distance from the neutral axis to the centroid (assuming that in pure bending, the neutral axis would pass through the centroid). The axial load and bending moment were then calculated based on these strain values and compared to the loads applied by the materials testing machine, with the assumption that the fibula bore 10% of the load, leaving 90% for the tibia. However, when calculating the loads based on the measured strain and geometric properties, the axial loads had relative errors up to 50%. This was believed to be due to the fact that based on the decomposition of measured strain values, bending strain was many times higher than the axial compression strain. This indicated that bending appeared to dominate loading at midshaft even in a compression configuration, likely due to tibial curvature.

1.4.2 Untaroiu *et al.* 2007

Untaroiu *et al.* (2007) applied a similar methodology to Funk and Crandall's to full-body cadaveric vehicle-pedestrian side impact tests, in which each subject was struck once by a sled, inducing primarily bending. Twelve uniaxial strain gauges in total were applied to bones in the specimen: four gauges were applied to each of the femurs and to one tibia (for a total of twelve gauges per post-mortem human subject). After impact, the bones were dissected, re-instrumented in the chance that strain gauges were damaged during impact, and subjected to controlled quasistatic three-point bending tests in a materials testing machine. The sled tests produced a variety of soft tissue injuries and fractures, including tibial plateau and fibular fractures, but there were no fractures at the midshaft of the bones under examination.

The basic assumptions used to correlate strain to load were similar to those used by Funk and Crandall: that the bones behaved as long beams under bending and compression, and that shear and torsion were negligible. However, geometric properties were not calculated about an assumed neutral axis. Instead, moments were resolved along two orthogonal axes at every time step of testing, and strain at each gauge was assumed to be a linear combination of these moments and axial loading. Geometric properties about these axes were used to solve these linear equations. Because four gauges were used, it was possible to solve these equations using three of the gauges and to predict strain at the redundant gauge. Solving for the loads applied and the geometric properties of the cross sections of interest required a custom MATLAB program, but ultimately the prediction of the fourth gauge's strain readings showed good agreement with the measured data, with 10-15% relative error at the time of peak loading.

1.4.3 Henderson *et al.* 2013

In an attempt to calculate the strain-rate-sensitive stiffness of the tibia under axial loading, Henderson *et al.* (2013) used Funk and Crandall's method of estimating the neutral axis and shifting it to decompose loading into bending and compression. The calculated axial strain was not used to recalculate applied loads, but instead to determine an effective stiffness of the specimen based on the known values of load and strain. In order to overcome the challenges faced by Funk and Crandall, Henderson *et al.* used six uniaxial strain gauges arranged circumferentially instead of three rosettes, in order to more accurately calculate the location and orientation of the neutral axis. As well, the gauges were arranged at the distal tibia instead of at midshaft, with the assumption that

due to curvature, the contribution of bending loads would be less at this location. The strain data were used to determine that the specimen was effectively stiffer at higher loading rates.

1.5 Study Rationale and Overview

Most of the reviewed experimental studies on impact loading do not take into account non-standard lower leg postures. The effects of impact velocity and acceleration, and off-axis loads were also frequently not considered. Additionally, very few tibial fractures were produced experimentally across the reviewed studies, despite the fact that they are an expected outcome of a dynamic impact scenario such as a frontal automotive collision. Tibia fractures made up 19.1% of the severe fractures noted in a review of frontal crash injuries in the lower extremity (6.7% plafond fractures, 6.7% tibial shaft fractures, 5.7% tibial plateau fractures). The most frequent locations of fractures in the reviewed studies were the calcaneus and talus, which only had an incidence rate of 14.3% (8.2% talar and 3.1% calcaneal fractures) (Taylor *et al.* 1997). Therefore, there is still a need for experimental work to determine the tibia's resistance to fracture under dynamic impact loading in a non-standard posture that produces off-axis loading.

In this work, 12 (six pairs) isolated cadaveric tibias were used for impact testing. The use of isolated bones removed some of the ambiguity about the distribution and dissipation of load that is present when using specimens with multiple types of tissues and joints. These tibias were instrumented with strain gauges and their geometries were captured via CT scans. The specimens were then installed in a custom-built test apparatus that allowed the user to fire a projectile of variable mass at each specimen until

fracture occurred. This apparatus was developed with the intention of being able to realistically simulate the conditions of a frontal automotive collision.

The angle between the line of impact and the bone's long axis was used to represent a non-standard lower leg posture (knee extension and corresponding plantarflexion), and one specimen from each donor was held at an angle of 15° while the contralateral was held at 30°. This use of paired specimens allowed for a close look at the effect that posture has on the bone's fracture tolerance. After fractures were produced, data gathered from the impact tests were analysed to determine the best contributors to injury risk. These contributors were incorporated into a Weibull survivability plot.

Two ATDs were also evaluated in the aforementioned non-standard postures to examine their behaviour when subjected to increasingly off-axis loading. The forces and moments registered by their internal load cells were compared to those measured by the externally-mounted load cell in the cadaveric tests, and these data were used to suggest guidelines for testing in non-standard postures.

Prior to impact testing, four of the specimens (two pairs) were subjected to quasistatic bending tests that were later used, in conjunction with geometric data obtained from the CT scans, to estimate loads internal to the bone during dynamic testing. The calculated loads were compared to those measured by the external load cell to assess the value of this method for determining loading in long bones.

Ultimately, the goal of this work was to develop a posture-specific injury criterion for the tibia. This will be useful in the design of protective measures by allowing engineers to design for the most injurious postures an occupant may choose to take on.

1.5.1 Objectives and Hypotheses

The objectives of this thesis were:

1. a) To develop the pneumatic system for an experimental apparatus that allows the user to fire a projectile of variable mass at specimens under parameters representative of a frontal automotive collision.

   b) To experimentally develop an injury risk function for the tibia under off-axis dynamic loading, and, if possible, to reformulate existing injury criteria to account for the effect of posture on fracture risk.
2. To investigate the response of two Anthropomorphic Test Devices (Humanetics Hybrid III – 50^{th} and MIL-LX) under dynamic impact in these same non-standard lower leg postures, and
3. To investigate the applicability of strain gauges to non-invasively estimate loads internal to long bones.

The corresponding hypotheses were:

1. The force tolerance of the tibia would be lower as the component of off-axis load increased due to the larger component of bending relative to axial compression.
2. The MIL-LX would be less sensitive to off-axis impact configurations than the Hybrid III due to the MIL-LX's enhanced design features.
3. A positive relationship between surface strains and internal bone loads would be found that would allow for non-invasive estimate of forces and moments delivered to the tibia during impact testing. Higher measured surface strains would correspond to higher internal bone loads.

1.6 References

Carpanen, Diagarajen, Spyros Masouros, and Nicolas Newell. 2016. "Surrogates of Human Injury." In *Blast Injury Science and Engineering: A Guide for Clinicians and Researchers*, edited by Anthony M. J. Bull, Jon Clasper, and Peter F. Mahoney, 189–98. Springer.

Crandall, J. R, S. M. Kuppa, G. S. Klopp, G. W. Hall, W. D. Pilkey, and S. R. Hurwitz. 1998. "Injury Mechanisms and Criteria for the Human Foot and Ankle under Axial Impacts to the Foot." *International Journal of Crashworthiness* 3 (2): 147–62.

Dong, Liqiang, Feng Zhu, Xin Jin, Mahi Suresh, Binhui Jiang, Gopinath Sevagan, Yun Cai, Guangyao Li, and King H. Yang. 2013. "Blast Effect on the Lower Extremities and Its Mitigation: A Computational Study." *Journal of the Mechanical Behavior of Biomedical Materials* 28. Elsevier: 111–24.

Funk, James R., and Jeff R. Crandall. 2006. "Calculation of Tibial Loading Using Strain Gauges." *Biomedical Sciences Instrumentation* 42 (2): 160–65.

Funk, James R., Jeff R. Crandall, Lisa J. Tourret, Conor B. MacMahon, Cameron R. Bass, and James T. Patrie. 2002. "The Axial Injury Tolerance of the Human Foot/Ankle Complex and the Effect of Achilles Tension." *Journal of Biomechanical Engineering* 124 (6): 750.

Funk, James R., Rodney W. Rudd, Jason R. Kerrigan, and Jeff R. Crandall. 2007. "The Line of Action in the Tibia during Axial Compression of the Leg." *Journal of Biomechanics* 40: 2277–82.

Funk, James R, Rodney W Rudd, Jason R Kerrigan, and Jeff R Crandall. 2004. "The Effect of Tibial Curvature and Fibular Loading on the Tibia Index." *Traffic Injury Prevention* 5 (2): 164–72.

Gallenberger, Kathryn, Narayan Yoganandan, and Frank Pintar. 2013. "Biomechanics of Foot / Ankle Trauma with Variable Energy Impacts." *Annals of Advances in Automotive Medicine*, no. 1997: 123–32.

Gray, Henry. 1918. *Anatomy of the Human Body*. Edited by Warren H. Lewis. 20th ed. New York: Bartleby.com.

Hardin, E.C., A. Su, and A.J. van den Bogert. 2004. "Pre-Impact Lower Extremity Posture and Brake Pedal Force Predict Foot and Ankle Forces during an Automobile Collision." *Journal of Biomechanical Engineering* 126 (6): 770–78.

Henderson, Kyvory A, Ann M Bailey, John J Christopher, Fred Brozoski, and Robert S

Salzar. 2013. “Biomechanical Response of the Lower Leg under High Rate Loading.” *2013 IRCOBI Conference Proceedings*, 145–57.

Huelke, Donald F., James O’Day, and John D. States. 1982. “Lower Extremity Injuries in Automobile Crashes.” *Accident Analysis and Prevention* 14 (2): 95–106.

Humanetics Innovative Solutions. 2015a. “Hybrid III 50th Male Dummy.” http://www.humaneticsatd.com/crash-test-dummies/frontal-impact/hybrid-iii-50th.

Humanetics Innovative Solutions. 2015b. “MIL-LX Legs.” http://www.humaneticsatd.com/crash-test-dummies/aerospace-military/mil-lx-legs.

Kuppa, S, and J Wang. 2001. “Lower Extremity Injuries and Associated Injury Criteria.” In *17th ESV Conference*. Vol. No. 457.

MacKenzie, E J, J H Siegel, S Shapiro, M Moody, and R T Smith. 1988. “Functional Recovery and Medical Costs of Trauma: An Analysis by Type and Severity of Injury.” *The Journal of Trauma* 28 (3): 281–97.

McKay, Brian J, and Cynthia A Bir. 2009. “Lower Extremity Injury Criteria for Evaluating Military Vehicle Occupant Injury in Underbelly Blast Events.” *Stapp Car Crash Journal* 53: 229–49.

Mertz, H. 1993. “Anthropomorphic Test Devices.” In *Accidental Injury, Biomechanics, and Prevention*, edited by A. Nahum. Springer-Verlag.

NATO. 2007. “Test Methodology for Protection of Vehicle Occupants against Anti-Vehicular Landmine Effects. Final Report of HFM-090 Task Group 25.”

Newell, Nicolas, Spyros D. Masouros, and Anthony M J Bull. 2013. “A Comparison of MiL-Lx and Hybrid III Responses in Seated and Standing Postures with Blast Mats in Simulated under-Vehicle Explosions.” In *2013 IRCOBI Conference Proceedings*, 135–44.

Quenneville, Cheryl E, Stewart D McLachlin, Gillian S Greeley, and Cynthia E Dunning. 2011. “Injury Tolerance Criteria for Short-Duration Axial Impulse Loading of the Isolated Tibia.” *The Journal of Trauma: Injury, Infection, and Critical Care* 70 (1): E13–18.

Rho, Jae Young, Liisa Kuhn-Spearing, and Peter Zioupos. 1998. “Mechanical Properties and the Hierarchical Structure of Bone.” *Medical Engineering and Physics* 20 (2): 92–102.

Roaas, Asbjørn, and Gunnar B. J. Andersson. 1982. “Normal Range of Motion of the Hip, Knee and Ankle Joints in Male Subjects, 30–40 Years of Age.” *Acta*

Orthopaedica 53 (2): 205–8.

Rudd, Rodney, Jeff Crandall, Steven Millington, Shepard Hurwitz, and Niklas Höglund. 2004. "Injury Tolerance and Response of the Ankle Joint in Dynamic Dorsiflexion." *Stapp Car Crash Journal* 48: 1–26.

Singh, Inderbir. 1978. "The Architecture of Cancellous Bone." *Journal of Anatomy* 127 (Pt 2): 305–10.

Takebe, K, A Nakagawa, H Minami, H Kanazawa, and K Hirohata. 1984. "Role of the Fibula in Weight-Bearing." *Clinical Orthopaedics and Related Research* 184: 289–92.

Taylor, Andrew, Andrew Morris, Pete Thomas, and Angus Wallace. 1997. "Mechanisms of Lower Extremity Injuries to Front Seat Car Occupants - an in Depth Accident Analysis." In *1997 IRCOBI Conference Proceedings*, 53–72.

Troy, Karen L., and Mark D. Grabiner. 2007. "Off-Axis Loads Cause Failure of the Distal Radius at Lower Magnitudes than Axial Loads: A Finite Element Analysis." *Journal of Biomechanics* 40 (8): 1670–75.

Untaroiu, Costin, Jason Kerrigan, Check Kam, Jeff Crandall, Kunio Yamazaki, Keisuke Fukuyama, Koichi Kamiji, Tsuyoshi Yasuki, and James Funk. 2007. "Correlation of Strain and Loads Measured in the Long Bones with Observed Kinematics of the Lower Limb during Vehicle-Pedestrian Impacts." *Stapp Car Crash Journal* 51 (October): 433–66.

van der Horst, M.J., C.K2 Simms, R. Van Maasdam, and Leerdam P.J.C. 2005. "Occupant Lower Leg Injury Assessment in Landmine Detonations under a Vehicle." In *IUTAM Proceedings on Impact Biomechanics*, 41–49. doi:10.1007/1-4020-3796-1_5.

Viano, David C, and Albert I King. 2008. "Biomechanics of Chest and Abdomen Impact." In *Biomechanics: Principles and Applications*, edited by Donald R. Peterson and Joseph D. Bronzino, 2nd ed., 7–2. Boca Raton, FL: Taylor & Francis Group.

Yoganandan, Narayan, Frank a Pintar, Melbourne Boynton, Paul Begeman, Priya Prasad, Shashi M Kuppa, Richard M Morgan, and Rolf H Eppinger. 1996. "Dynamic Axial Tolerance of the Human Foot-Ankle Complex." *Society of Automotive Engineers, Inc.* 962426: 207–18.

Zuby, D S, J S Nolan, and C P Sherwood. 2001. "Effect of Hybrid III Geometry on Upper Tibia Bending Moments." *Society of Automotive Engineers Biomechanics Research and Development SP1577*, no. 724: 1–14.

Chapter 2: Design of a Pneumatic Impulse-Generation System to Support Impact Testing

2.1 Motivation

"Injury tolerance" refers to the ability of a tissue to withstand impact loading without failing (Viano & King 2008). This limit can be incorporated into the design criteria for protective devices and equipment, ultimately leading to a lower incidence of injuries to this body region. Due to practical constraints, it is difficult to determine injury tolerance in a controlled, accurate manner from real traumatic events. Therefore, experimental tests are conducted to simulate real-world conditions on Anthropomorphic Test Devices (ATDs) or cadaveric specimens. The apparatuses used to conduct these tests are usually custom-built for the purposes of each individual test site. An apparatus must be able to deliver an impact to a specimen in a controlled manner, as realistically as possible. The range of impact characteristics that a system is capable of producing depends heavily on its design.

Published results on impact testing rarely gives a lot of detail on the design of the test apparatus used, although this may have a strong influence on the quality and data one is able to gather from an experiment. A review of the impulse-generation subsystems of test apparatuses described in the literature follows. Details of testing that was conducted with these apparatuses is discussed in Section 1.3.

2.2 Review of Impulse-Generation Systems Described in the Literature

2.2.1 Pendulum

With a pendulum system, a mass is suspended at a fixed point, lifted to a predetermined height, and then released and allowed to swing in an arc until it makes contact with the specimen. Using this kind of system to deliver impulse has the advantage of relying on gravity to provide consistent acceleration in every test. By placing a specimen at the bottom of the pendulum's arc, the user can deliver repeatable loads in a horizontal direction for simulation of footwell intrusion in a frontal collision. Crandall *et al.* (1998) had their pendulum strike a horizontal transfer piston, which itself was connected to a universal joint and a footplate, which also allowed the ankle to flex realistically during intrusion.

The pendulum's drop height and mass, as well as the material properties of the hammer or any intermediate protective layers (such as foams or honeycomb structures) can be varied to control impact velocity, energy, force, and duration. As well, the reliance on gravity, which provides a consistent acceleration vector for the impacting mass, likely leads to highly repeatable impulse generation.

However, this reliance on gravity also limits the range of impact velocities possible in comparison with devices that can attain various magnitudes of impactor acceleration. Additionally, alignment of the specimen with the exact bottom point of the pendulum's arc may be challenging, and off-axis loading may unintentionally be induced if the specimen is placed at another point along the arc.

2.2.2 Linear Impactor

In this type of device, a piston-driven linear actuator moves towards the specimen along a purely linear path. Generally, impacts are applied in the horizontal direction, meaning that gravity does not play a role in the motion of the impactor. These types of systems may be driven by pneumatic or hydraulic actuators, which allow the user to vary the impacting hammer's acceleration within the manufacturer's specifications. As with other types of test rigs, the material properties of the impacting hammer or any intermediate materials may be varied to modulate impact characteristics.

The fact that the user potentially has control over the impactor's acceleration may provide an advantage over pendulum systems in terms of the system's flexibility. The actuator's fixed stroke length also provides a highly repeatable magnitude of intrusion and therefore impact duration (McKay & Bir 2009). Like with a pendulum system, the material properties of the impacting hammer and the intermediate layers can be varied to change impact characteristics.

However, the impacting hammer itself does not move freely of the impulse generation system, making it difficult to quantify impact energy (as velocity may be known, but mass cannot be isolated). Additionally, the use of compressed fluids to drive the actuator can pose a safety risk to the user. Finally, the actuator used in a system such as this may be an off-the-shelf component, and as such would be limited by the manufacturer's specifications. If commonly available specifications do not meet the needs of the team performing the experiments, it may be necessary to have an actuator custom-made.

2.2.3 Drop Tower

A drop tower consists of a specimen held below an impacting hammer, which can be released to simply fall onto the specimen or any intermediate layers.

Drop towers, due to their vertical configuration, may allow the designer to be efficient with their use of floor space compared with other methods of impulse generation. They also rely on gravity in a very similar manner to pendulums, which brings a consistency of acceleration upon which the user can rely. Unlike with a linear impactor, it is easy to vary the mass of the impacting hammer in a drop tower. Varying the drop height also allows fine control over impact velocity. By measuring the drop height and impact velocity, it also becomes easy to perform an energy balance to determine any losses due to friction or the deformation of the intermediate layers, if this is of interest to the user. Finally, once again, changing the intermediate layers can offer the user control over impact characteristics.

One of the challenges of designing a drop tower is determining how to create realistic boundary conditions for the movement of the specimen after impact. Any constraint of the specimen following impact will introduce reaction forces (Henderson *et al.* 2013). Allowing free motion of the specimen after impact in simulation of a real traumatic event (in which impulse would be delivered from below, not above) is very challenging in this test configuration. The specimen may need to be placed on a platform supported by springs or other deformable elements in order to allow some motion after impact, although this may provide a stiffer boundary condition than would exist in real life.

Additionally, as with a pendulum system, the reliance on gravity for acceleration may limit the range of velocities that can be achieved. For example, assuming no losses due to friction or deformation, a drop height of 5.1 m would be necessary to achieve a velocity of 10 m/s, which would be very impractical in many facilities.

2.2.4 Vertical Accelerator

Similar to the drop tower design previously discussed, Yoganandan *et al.* (2015) chose a vertical configuration, but instead of dropping masses directly onto a specimen, they used a lever and fulcrum system to apply loads from below. The Vertac system allows the user to drop masses from a variety of heights on one side of its frame. The masses fall onto a lever arm, which pivots at its other end to deliver impulse to the specimen from below. The pivot point can be changed to alter the lever arm ratio, which in turn changes the force and velocity of impact delivered to the specimen.

The vertical configuration of this device allows for recreation of traumatic events in their natural orientation (*e.g.,* with the lower limb vertical and the plantar surface facing downwards). The ability to change the pivot point of the system also provides more adjustability in terms of impact velocity and acceleration than is usually found in a simple drop tower. Additionally, as with all other systems, the impact duration, force, and energy can be modulated by changing the intermediate layers between the specimen and the point of impact.

The challenge with implementing this system is that, unlike a simple drop tower, it covers quite a bit of floor space as well as vertical height. It is also difficult to allow the specimen to move freely after impact, and the specimens tested in Vertac are

constrained to move along a linear rail mounted on one column of its frame. These limitations may be the reason that no similar apparatus has previously been described in the literature.

2.2.5 Pneumatic Projectile Impactor

An alternative to the previously-described systems is to have a freely moving projectile strike the specimen. The projectile can be propelled with compressed air within a sealed acceleration tube. The pressure of the supplied compressed air as well as the projectile's initial starting position relative to the specimen can be varied to change the impact velocity. By making the projectile's design modular, it is also possible to change the magnitude of the impacting mass.

Because the projectile is freely moving, there is no ambiguity about its mass, allowing for easy calculation of impact energy. As well, the use of compressed air as a propellant and a variable starting position can provide a lot of flexibility in terms of acceleration and impact velocity. Once again, impact characteristics can be varied by changing the properties of the intermediate layers between the projectile's strike point and the specimen.

However, the use of compressed gas raises safety concerns. All components of the pneumatic system must therefore be carefully sealed prior to pressurisation, and there must be controls in place to avoid exceeding the safe working pressure of the system. Because there is so much potential for flexibility with this kind of system, it is also necessary to perform calibration tests for each desired mass and distance combination

prior to an experiment (Quenneville *et al.* 2010), as the acceleration is not guaranteed to be consistent the same way it would be in a gravity-driven system.

2.2.6 Impact Characteristics Generated

The requirements for the system's capabilities were determined based on reported impact characteristics from the literature (Table 2-1). Reported impacting masses varied from 3.3 to 61.2 kg, and impact velocities varied from 1.5 to 11.6 m/s. These values were kept in mind when determining the requirements of the system described herein.

2.3 Previous Work on Current Test Apparatus

The test apparatus used for this work was modelled closely on the one used by Quenneville *et al.* at Western University (2010). The specimen is suspended within a test chamber by chains of adjustable length. Changing the lengths of the chains allowed the user to set the orientation of the specimen relative to the direction of impact. The chains were connected to an overhead rail and bearing system that allowed the specimen to translate freely after impact. The rail and bearing system and the components that supported the specimen were all housed within a test chamber made of steel tubing and enclosed with polycarbonate shielding.

Impulse was delivered to the specimen by a pneumatically-propelled projectile. The projectile had a modular design, with components that could be added or removed from a length of threaded rod. It had a small head, which could enter the test chamber a fixed distance to deliver impulse, while the rest of its components were of a larger diameter. These included two stabilising washers made of nylon that had an 0.03" (0.76

Table 2-1: Summary of Impact Characteristics Described in the Published Literature
The various impact test apparatuses described in the literature are compared in terms of the types of loading they were able to generate.

Paper	**Type of System**	**Type of Loading**	**Masses Used (kg)**	**Velocities Generated (m/s)**
(Crandall *et al.* 1998)	Pendulum	Axial and off-axis at plantar surface of foot	9-27	6-7
(Funk *et al.* 2002)	Linear actuator	Axial at plantar surface of foot	Not provided	5
(Gallenberger *et al.* 2013)	Pendulum	Axial and off-axis at plantar surface of foot	3.30, 5.70, 12.32	1.5-9
(Henderson *et al.* 2013)	Drop tower	Axial at plantar surface of foot	38.5-61.2	4.09-5.93
(Kitagawa *et al.* 1998)	Pendulum	Axial at plantar surface of foot	18	2.91-3.99
(McKay & Bir 2009)	Linear actuator	Axial at plantar surface of foot	Not provided	7.2, 9.0, 11.6
(Quenneville *et al.* 2010)	Projectile	Axial at distal articular surface of tibia	3.9, 6.8	2.3-13.9
(Seipel *et al.* 2001)	Pendulum	Axial at plantar surface of foot	Not provided	2.2-6.7
(Yoganandan *et al.* 1996)	Pendulum	Axial at plantar surface of foot	16	3.4-7.6
(Yoganandan *et al.* 2015)	Vertical accelerator	Axial at plantar surface of foot	36.3, 61.2	1.0-11.0

mm) clearance with the inner diameter acceleration tube, and which kept the projectile upright as it travels while also reducing contact area and friction with the tube. Besides these washers, there were slightly smaller (3.75" or 95.25 mm) cylindrical steel masses, each weighing approximately 1 kg. These masses could be added or removed to change the projectile's mass. The larger components could not enter the test chamber and kept the projectile from exiting the acceleration tube.

The projectile head struck an intermediate plate, which could translate on linear bearings. Foam layers could be added to the projectile side of this plate to modulate impact duration. On the other side of the plate, a six axis load cell (IF-625, Humanetics Innovative Solutions, Plymouth, MI, USA) of 20 kN capacity was mounted in place. The specimen rested against this load cell, which measured reaction forces and moments generated during impact. As the projectile head entered the test chamber, it passed two optical sensors (PZ-V31P, Keyence Corporation, Osaka, Japan) that were used to calculate velocity at the point of impact.

A more detailed account of the operation of this apparatus is provided in Chapter 3.

The mechanical components of the impact testing apparatus were already constructed and assembled prior to the start of this work (Figure 2-1). This included the test chamber, the specimen support and angle adjustment systems, the projectile components, the acceleration tube and associated support structure. A pneumatic system capable of propelling the projectile was still needed.

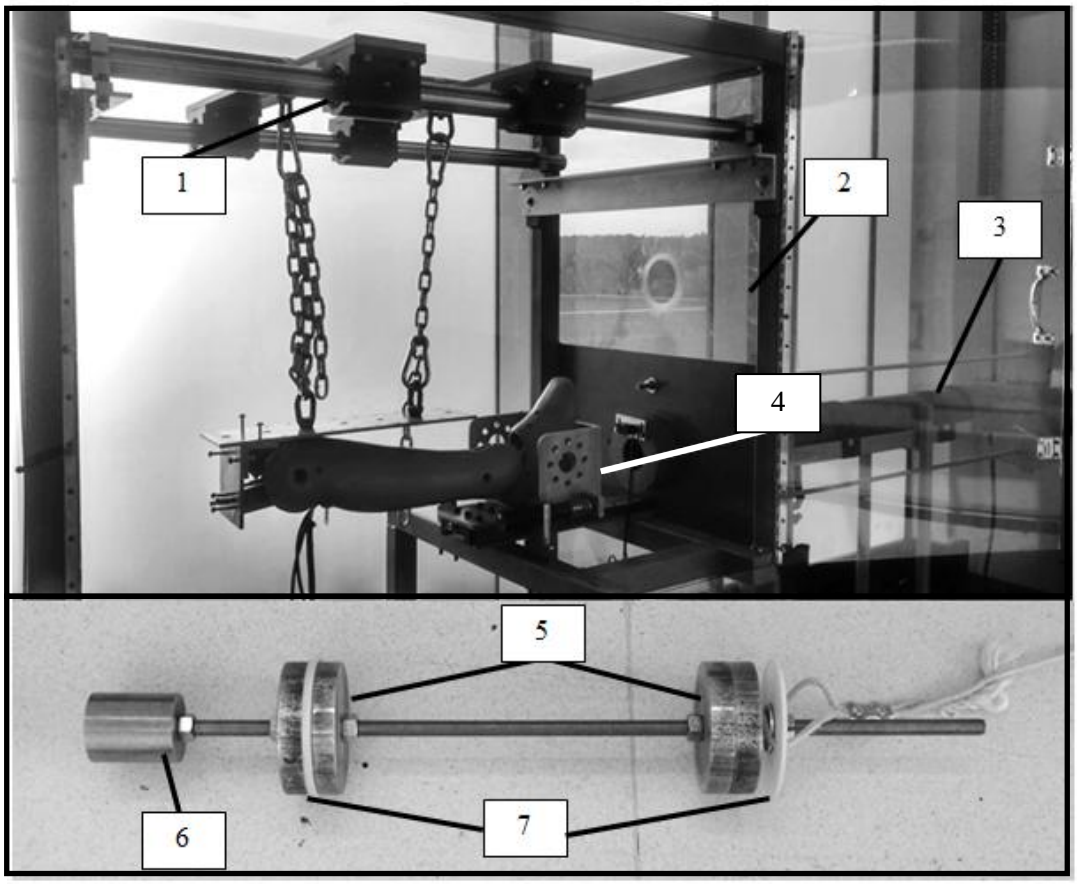

Figure 2-1: Previously Constructed Apparatus Components
Components of the test apparatus constructed and installed prior to the start of this work: (1) Specimen support/angle adjustment system, (2) test chamber, (3) acceleration tube and associated supporting structure, (4) intermediate footplate, (5) projectile masses, (6) projectile impacting head, (7) stabilising washers.

2.4 Design and Assembly

2.4.1 Design Objectives

Drawing upon the capabilities of systems described in the literature in order to maximise the system's versatility, it was decided that the objectives of the system were:

1. All components must be sealed and secured to ensure the operator's safety up to the highest possible system pressure.
2. It must take up the least floor space possible, while still allowing access for loading the projectile, maintenance, and disassembly.
3. It must be able to release a large volume of air quickly into the acceleration tube so that pressure remains relatively constant during the acceleration of the projectile.
4. All losses to the flow's energy must be minimised wherever possible, including friction within the pipe, unnecessary length and bends in the pipe, and changes in the pipe's diameter. Losses must be minimised such that the highest impact velocity required for testing is achievable with the highest required projectile mass before reaching the maximum supplied pressure of 60 psi (41.3 kPa).
5. It must ultimately be able to propel projectiles of a range of masses (approximately 5-20 kg) so that they can achieve a wide range of impact velocities (approximately 5-12 m/s) in a repeatable manner. This will allow the system to generate a range of impacts that would be comparable to those generated by a variety of other test apparatuses described in the literature.

6. The system must allow for high repeatability, with the standard deviation of the impact velocities generated by a single mass-pressure combination being no more than 10% of the mean of the velocities over repeated trials.

2.4.2 System Components

The system can be broken down into three subsystems: air accumulation, air release, and projectile acceleration tube. These components are described in detail below, with reference to their numbering in Figure 2-2.

2.4.2.1 Air Accumulation

Compressed air is piped in from the building supply at 60 psi (413.7 kPa). A 0.5" (12.5 mm) hose runs from the connection point to a filter/regulator/lubricator unit (NBC-400, Royal Fluid Power, Burlington, ON, Canada) (Item #1 in Figure 2-2), which allows the user to reduce the pressure to the desired level. This feeds into an air reservoir (A10040-MOD, Samuel Pressure Vessel Group, Marinette, WI, USA) (Item #2) 30 gallons (113.6 L) in capacity, which is fitted with a digital pressure gauge (DG25, Ashcroft, Stratford, CT, USA) (Item #3) that is used to measure the accumulated air pressure. The reservoir's capacity plus the capacity of the other accumulation components (approximately 115 L) was intended to be at least ten times the volume of the pneumatic system after the air release point (approximately 11 L), measured to the end of the acceleration tube. This was done to ensure that air is supplied consistently without a substantial reduction in pressure throughout the release duration. To resist the effects of recoil after release, the tank is secured to the laboratory floor using concrete anchors.

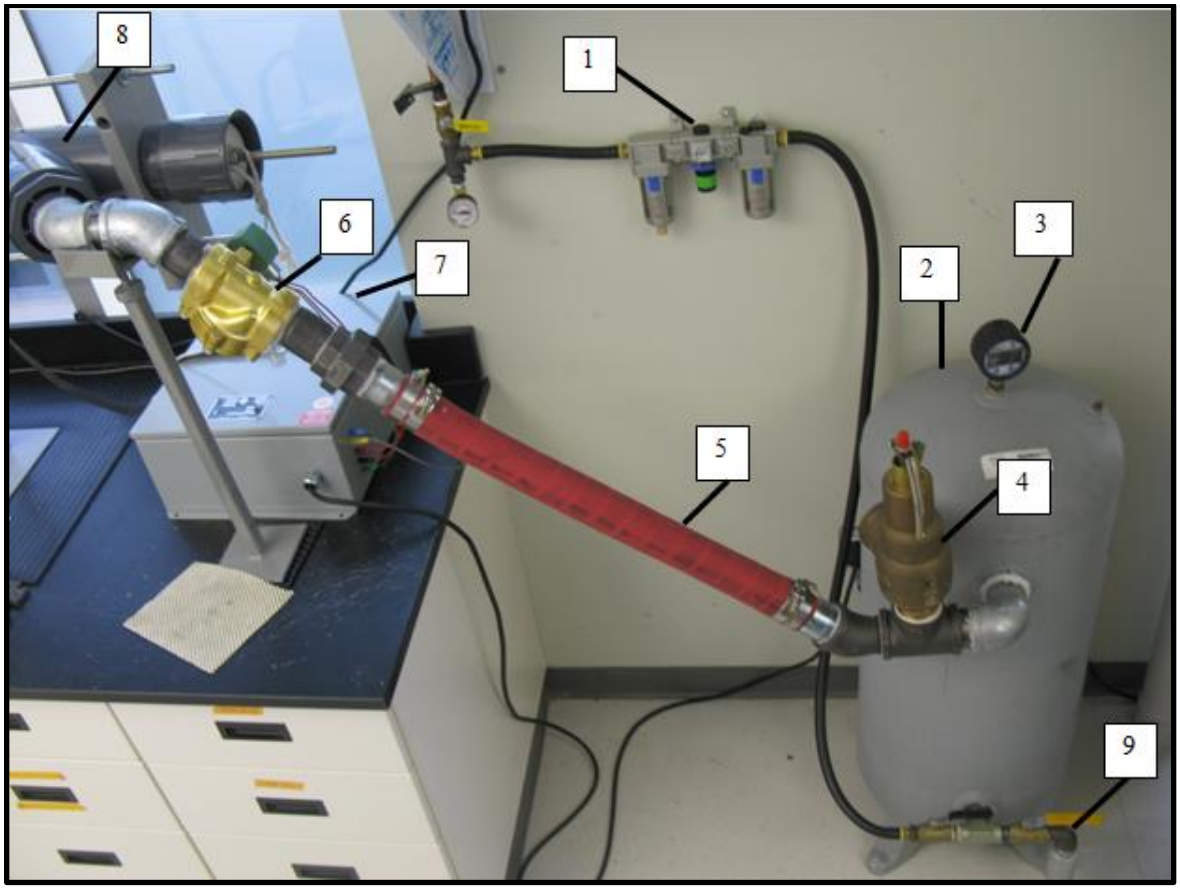

Figure 2-2: Key Components of the Pneumatic Impulse Generation System.
(1) Filter/regulator/lubricator unit connected to wall air used to set pressure of air fed into reservoir, (2) 30 gallon reservoir that allows accumulation, (3) digital pressure gauge used to measure accumulated air pressure, (4) pressure relief valve, (5) flexible hose, (6) normally-closed fast-acting solenoid valve that releases accumulated air in a short burst when triggered, (7) electrical panel containing smart relay used to trigger solenoid valve, (8) 4" PVC wye ("Y") fitting that has air fed through one leg and the impacting projectile loaded through the other, (9) muffler connected to one of the reservoir's outlets, which allows for the safe discharge of air after testing is completed.

The tank has one inlet and two outlets. One outlet leads to a ball valve, which allows for the release of accumulated air after testing is completed. There is also a muffler (item 9) on this outlet to reduce the noise of air discharge, and the outlet is directed at the ground to reduce risk of injury to the operator. The other outlet leads to the projectile acceleration tube. This outlet is 2" (5.08 mm) in diameter and leads to a steel T-fitting, which connects to a pressure relief valve (60100JHM01-KM, Kunkle, Stafford, TX, USA) (Item #4) that will activate if the supplied air pressure exceeds the maximum allowable working pressure of the tank, 200 psi (1379 kPa). This pressure limit is also higher than the maximum pressure of the supplied air, thus allowing for a factor of safety even if the incoming airline is modified at a later date (for example, if it is connected directly to a compressor). Under normal conditions, air will continue to flow through the T-fitting to a street 45° fitting, and then a 2" (5.08 mm) hose barb. The barb connects to a flexible length of hose (Item #5), which can bend to compensate for misalignment or recoil. Another hose barb connects the other end of the hose to a union fitting, which allows for an easy point of disassembly in case maintenance is required.
The hose is secured with two hose clamps at each end, and all steel fittings are sealed with pipe dope compound.

2.4.2.2 Air Release

At the end of the flexible hose, the accumulated air is held by a fast-acting, normally-closed solenoid valve (8210 103 245VDC, ASCO, Florham Park, NJ, USA) (Item #6), which is controlled by a smart relay (Zelio Logic 2, Schneider Electric, Rueil-Malmaison, France) housed in a custom-built electrical panel (Item #7). The relay is

triggered by an analog output signal (5V) from the data acquisition system (PXIe-1082, National Instruments, Austin, TX, USA). After the voltage signal is sent, the valve is opened for a predetermined duration of time (adjustable from 0.1 to 99 s). This releases air into the acceleration tube.

2.4.2.3 Projectile Acceleration Tube

The released compressed air feeds into one leg of a 4" (101.6 mm) schedule 80 PVC wye fitting (Item #8). The projectile is loaded through the other leg of the fitting and is positioned prior to each test so that its trailing end sits beyond the wye. The compressed air is then able to push against the projectile to accelerate it down the acceleration tube (4" (101.6 mm) schedule 80 PVC pipe) towards the test chamber.

2.5 System Capabilities

All components of the system are rated for at least 100 psi (690 kPa), although the maximum pressure of the supplied air is 60 psi (414 kPa). The velocity that any given air pressure can generate depends on the mass of the projectile used. Calibration data for predicting impact velocity based on various projectile masses and supplied air pressures are included in 0 for projectiles of 2.8 to 14.7 kg. Velocities were achieved from 4.0 to 13.5 m/s. Figure 2-3 shows a representative calibration curve for a projectile of mass 2.8 kg. Pressures are reported in psi as this is the unit of the digital pressure gauge. The data were highly linear (R^2=0.991).

Projectile masses greater than 14.7 kg were also needed for impact testing. Because the impact testing protocol described in Chapter 3 was only to be carried out at

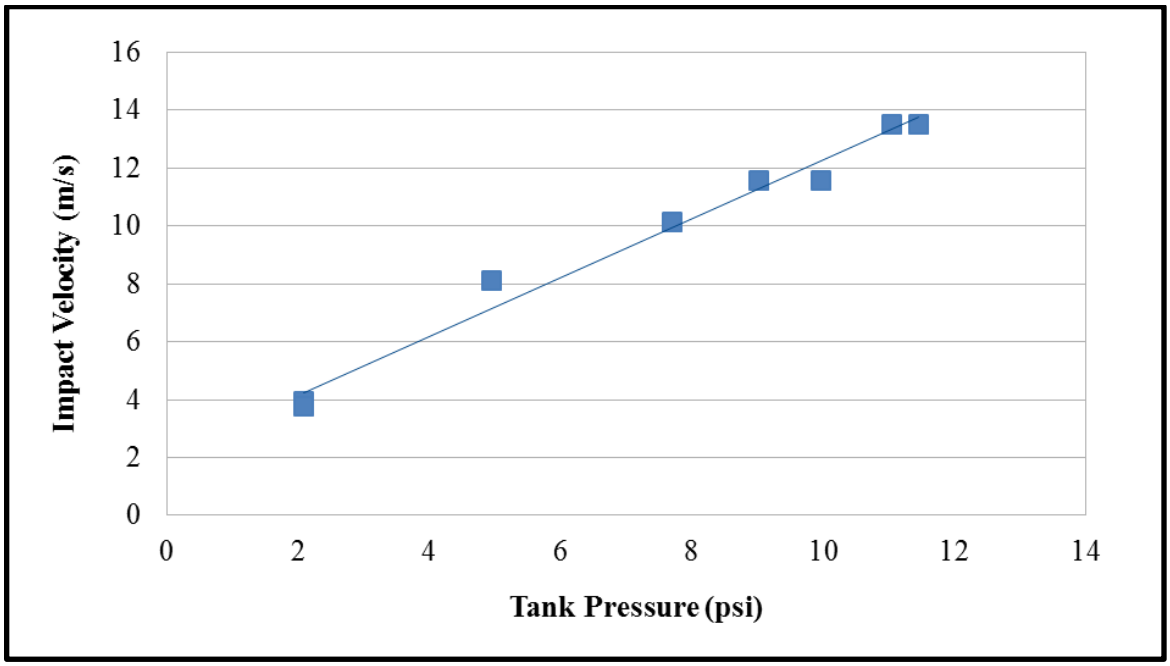

Figure 2-3: Pressure-Velocity Calibration Curve for 2.8 kg Projectile
A representative calibration curve is presented. A linear trendline has been fit to the data, with an R^2 value of 0.991.

one single velocity of 6 m/s, calibration curves were not generated for these masses across multiple velocities. Instead, for each new mass, the pressure was increased slightly from the previous appropriate value. The pressure would then be adjusted by approximately 1 psi (6.9 kPa) per kilogram of increased mass until the desired velocity had been achieved. Figure 2-4: Pressure-Mass Curve for 6 m/s Impacts shows how pressure was increased to achieve impacts of 6.0 (±0.5) m/s velocity with increasing projectile mass. The data were highly linear (R^2=0.993).

2.5.1 Repeatability

The system needed to produce impacts of a desired velocity with a high degree of repeatability. Care was taken to prevent leaks in the system, to minimise losses to the flow by geometrically arranging fittings to avoid unnecessary bends, and to create a standardised test protocol that ensured set-up was performed the same way in each test session. In order to evaluate system repeatability prior to testing, one mass-pressure combination was chosen for evaluation (4.2 kg at 8.5 psi, or 58.6 kPa).

A piece of wood was installed in the test chamber in place of a cadaveric specimen, and the projectile was fired five times at the prescribed pressure. The projectile's impact velocity was noted for each test. The system was completely drained of air and the regulator pressure was set to 0 between tests to simulate variation that would happen between multiple days of testing. The impact velocities were recorded in Table 2-2.

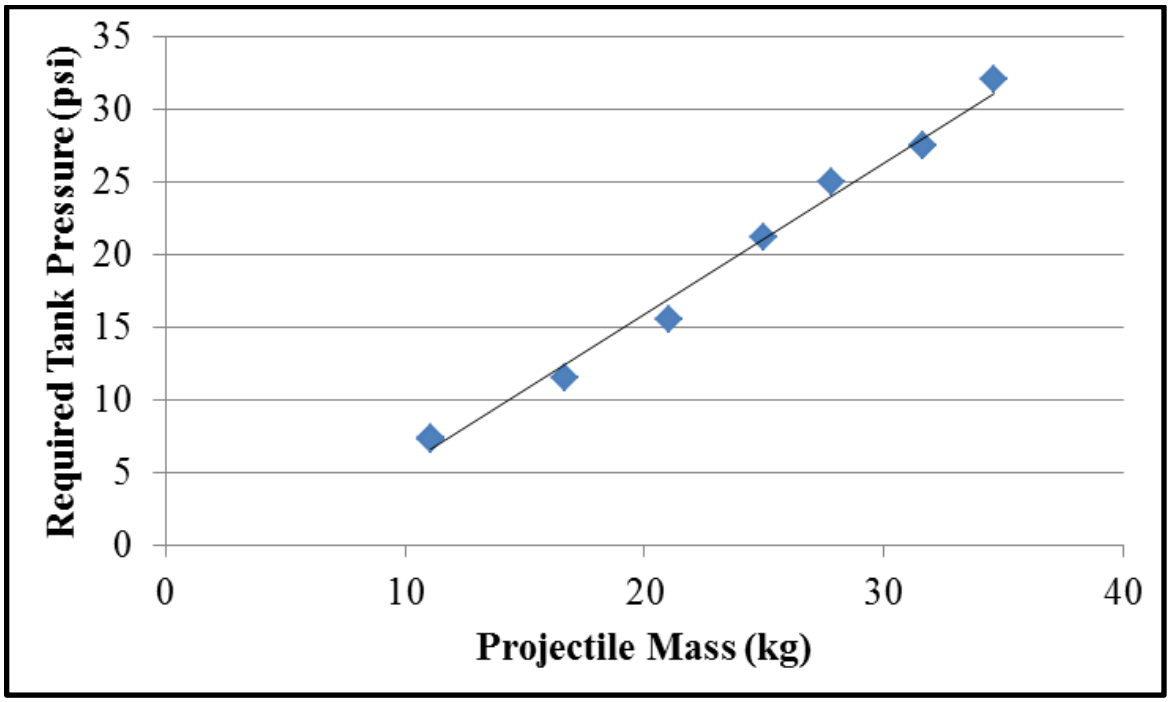

Figure 2-4: Pressure-Mass Curve for 6 m/s Impacts
The figure shows a linear (R^2=0.993) relationship between the mass of the projectile and the pressure required to achieve an impact velocity of 6.0 (±0.5) m/s.

Table 2-2: Results of Pneumatic System Repeatability Analysis

One mass-pressure combination (4.2 kg, 8.5 psi) was used to assess repeatability across five impacts.

Trial	**Impact Velocity (m/s)**
1	10.6
2	10.6
3	10.6
4	9.8
5	10.6
Mean (SD)	**10.4 (0.4)**

The mean impact velocity across the five trials was 10.4 m/s, with a standard deviation of 0.4 m/s. The standard deviation was 4% of the mean value, indicating high repeatability of the system.

2.6 Discussion

In order to accurately simulate the conditions of a frontal collision on a cadaveric specimen, an experimental apparatus that would deliver loads at prescribed velocities was needed. The developed system uses compressed air to propel a projectile to generate an impact, with projectile mass and air pressure being the factors that control velocity. This makes it more flexible than experimental systems that rely on gravity to accelerate an impacting mass.

The system has been calibrated for projectile masses of 2.8 to 14.7 kg, achieving a variety of velocities for each calibrated mass. In addition, higher projectile masses (up to 28 kg) were tested in this work, although individual calibration curves are not available for these masses. Instead, operators were able to increase pressure while also incrementing mass to achieve the specific velocity required for testing. This range of masses exceeds the range originally desired for the system. Furthermore, a broad range of velocities were achieved for many of the lighter masses, as low as 4 m/s and as high as 12 m/s.

Most of the calibration curves fit a linear trend, with generally high values of R^2 (0.677-0.996, refer to 0 for details). Usually, when one velocity was targeted, as mass was increased, there was also a linear increase in the required air pressure. However, these trends did not always hold true for all tested data points. The major sources of error

were thought to be friction between the projectile and the acceleration tube as well as flow losses after release of the compressed air. Friction may have increased through the testing process, as wear was likely induced in the acceleration tube where it made contact with projectile components. To overcome this, it was recommended that the relevant pressure-mass combinations be verified shortly prior to a test. This would give the tester confidence about the expected velocity output.

However, it was more critical that the system be repeatable than to determine a consistent linear relationship between mass-pressure combinations and velocity. The analysis of repeatability found that, for the chosen mass-pressure combination, the system was highly repeatable, with the standard deviation of the velocities only 4% of the mean.

Components were chosen for their ease of procurement, assembly, and maintenance, as well as their ability to perform the functions required of the system. The maximum supplied air pressure is 60 psi and all components are rated for at least 100 psi, ensuring that a factor of safety is applied to the system. All joints were also checked for leaks and sealed as per supplier recommendations.

Instructions for the safe operation of the pneumatic impulse-generation system, including measures to take against accidental triggering of the solenoid valve, are included in Appendix B.

The goal of this work was to design, construct, and install a pneumatic system capable of supporting the previously-developed mechanical components of an impact testing apparatus. This pneumatic system was needed to propel a projectile of variable mass at a specimen, while offering the user control over the projectile's impact velocity

and energy. A range of projectile masses and pressures were used to achieve a wide span of impacts. This system can produce impacts with characteristics up to and beyond the values reported for many similar systems described in the published literature. It may be used in a range of future studies on injury biomechanics, and has been already used in a study on the posture-specific fracture tolerance of the tibia (Chapter 3).

2.7 References

Crandall, J. R, S. M. Kuppa, G. S. Klopp, G. W. Hall, W. D. Pilkey, and S. R. Hurwitz. 1998. "Injury Mechanisms and Criteria for the Human Foot and Ankle under Axial Impacts to the Foot." *International Journal of Crashworthiness* 3 (2): 147–62.

Funk, James R., Jeff R. Crandall, Lisa J. Tourret, Conor B. MacMahon, Cameron R. Bass, and James T. Patrie. 2002. "The Axial Injury Tolerance of the Human Foot/Ankle Complex and the Effect of Achilles Tension." *Journal of Biomechanical Engineering* 124 (6): 750.

Gallenberger, Kathryn, Narayan Yoganandan, and Frank Pintar. 2013. "Biomechanics of Foot / Ankle Trauma with Variable Energy Impacts." *Annals of Advances in Automotive Medicine*, no. 1997: 123–32.

Henderson, Kyvory A, Ann M Bailey, John J Christopher, Fred Brozoski, and Robert S Salzar. 2013. "Biomechanical Response of the Lower Leg under High Rate Loading." *2013 IRCOBI Conference Proceedings*, 145–57.

Kitagawa, Yuichi, Hideaki Ichikawa, and Chinmoy Pal. 1998. "Lower Leg Injuries Caused by Dynamic Axial Loading and Muscle Testing." In *16th International Technical Conference on the Enhanced Safety of Vehicles*, 2:1597–1607.

McKay, Brian J, and Cynthia A Bir. 2009. "Lower Extremity Injury Criteria for Evaluating Military Vehicle Occupant Injury in Underbelly Blast Events." *Stapp Car Crash Journal* 53: 229–49.

Quenneville, Cheryl E, Gillian S Fraser, and Cynthia E Dunning. 2010. "Development of an Apparatus to Produce Fractures from Short-Duration High-Impulse Loading with an Application in the Lower Leg." *Journal of Biomechanical Engineering* 132 (1): 14502.

Seipel, Robert C, Frank a Pintar, Narayan Yoganandan, and Melbourne D Boynton. 2001. "Biomechanics of Calcaneal Fractures: A Model for the Motor Vehicle." *Clinical Orthopaedics & Related Research*, no. 388: 218–24.

Viano, David C, and Albert I King. 2008. "Biomechanics of Chest and Abdomen Impact." In *Biomechanics: Principles and Applications*, edited by Donald R. Peterson and Joseph D. Bronzino, 2nd ed., 7–2. Boca Raton, FL: Taylor & Francis Group.

Yoganandan, Narayan, Frank a. Pintar, Michael Schlick, John R. Humm, Liming Voo, Andrew Merkle, and Michael Kleinberger. 2015. "Vertical Accelerator Device to Apply Loads Simulating Blast Environments in the Military to Human

Surrogates." *Journal of Biomechanics*. Elsevier, 1–5.

Yoganandan, Narayan, Frank a Pintar, Melbourne Boynton, Paul Begeman, Priya Prasad, Shashi M Kuppa, Richard M Morgan, and Rolf H Eppinger. 1996. "Dynamic Axial Tolerance of the Human Foot-Ankle Complex." *Society of Automotive Engineers, Inc.* 962426: 207–18. doi:10.4271/962426.

Chapter 3: Injury Tolerance of the Tibia Under Off-Axis Impact Loading

3.1 Introduction

The lower leg is a frequent site of injury in frontal automotive collisions. While these injuries are not usually life-threatening, they can result in long-term pain and impairment (Read *et al.* 2004). Axial impact loading through the foot has been identified as a common mechanism of these fractures, but it is not the only loading mode present in this scenario. Bending has also been identified as a frequent cause of fractures to the distal tibia, and the most frequent mechanism of tibial shaft fractures in one review of car crash injuries (Ivarsson *et al.* 2008).

A widely-used injury criterion for the tibia (Tibia Index, or TI) takes both compression and bending into account when calculating injury risk:

$$TI = \frac{F}{F_c} + \frac{M}{M_c} \qquad \textbf{Equation 3-1}$$

In this equation, the value of TI corresponds to a risk of injury, F and M are applied axial force and resultant moment respectively, and F_c and M_c are critical values obtained from isolated cadaveric testing. This equation was first proposed by Mertz (1993) and later revised by Kuppa and Wang (2001). In the revised TI formulation, F_c has a value of 12 kN and M_c has a value of 240 Nm. These values were obtained from quasistatic compression and bending tests performed on isolated cadaveric tibias from male donors. TI values obtained from previous cadaveric testing were fit to a Weibull

model, resulting in the following guidelines: a TI value of 0.91 corresponds to a 25% fracture risk, a TI value of 1.0 corresponds to a 33% fracture risk, and a TI value of 1.16 corresponds to 50% fracture risk. TI can compute injury risk in a cadaveric specimen as well as help to establish limits for loads measured by an Anthropomorphic Test Device's (ATD's) internal load cell. However, there are several problems with TI that have driven researchers to revise it multiple times (*e.g.*, Zuby *et al.* 2001; Funk *et al.* 2004). These problems include the facts that the curvature of the tibia relative to the straight geometry of an ATD legform will have an effect on the bending moments induced by axial compression, and that the critical values were obtained from quasistatic tests despite the fact that the index is meant to be applied to dynamic crash tests. Because of this, it is important to more completely investigate the applicability of TI to assessing injury risk in the tibia.

While the response of the leg under axial dynamic impact has been thoroughly investigated experimentally (*e.g.*, Yoganandan *et al.* 1996), there is much less work that incorporates dynamic bending. Studies that do account for the effect of bending tend to only consider bending induced by tibia curvature in an axial compression set-up (Funk *et al.* 2004) or bending caused by impacts delivered perpendicular to tibial shaft (Untaroiu *et al.* 2008). Dynamic off-axis loading of the distal tibia due to a non-neutral posture of the lower leg relative to the line of action of the collision load delivered through the vehicle floor is largely uninvestigated, and has not been studied in terms of the isolated tibia's injury tolerance.

One of the goals of this work was to experimentally assess the effects of off-axis loading on injury risk in the tibia for two different non-standard postures, and to generate a new injury risk function for this loading scenario that takes posture into account. A secondary goal was to evaluate the performance of two ATDs in these non-standard postures.

3.2 Methods

3.2.1 Specimens

Twelve fresh-frozen cadaveric isolated tibiae (six pairs) were used for this study. Specimens from female donors, aged 48-73, with a mean (standard deviation) age of 64 (10.7) years were available for this study (Appendix A). This demographic gave a conservative estimate of injury risk, as it is known that the bones of older women tend be mechanically weaker and geometrically smaller than that of the general driving population. Specimens were kept and tested in pairs to allow for direct comparison of the effects of two different postures while controlling for some of the variation in geometry and mechanical properties among individuals.

Each specimen was fixed by its proximal end in a section of 4" (101.6 mm) PVC pipe (Figure 3-1) using dental cement (Denstone Golden, Heraeus Kulzer, South Bend, IN, USA) to a depth of approximately 3" (76.2 mm). Alignment was accomplished using a custom jig and laser levels, with each specimen centred proximally in the pipe section. The anterior crest at midshaft was used to define the vertical direction in the frontal plane, and the midpoint of the medial malleolus was used for the sagittal plane. Cement was

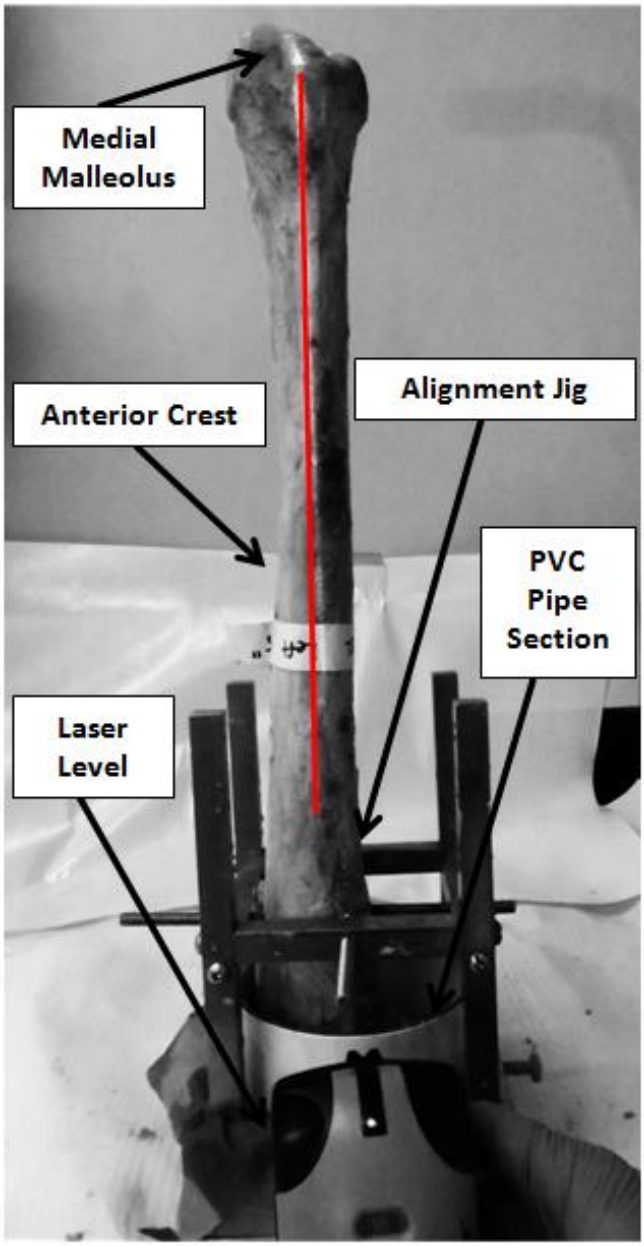

Figure 3-1: Alignment of a Cadaveric Specimen Before Potting
Specimen being aligned within a PVC pipe section, with the distal end pointing up. The red line represents a laser line projected onto the medial side of the specimen. The anatomical landmarks used for alignment (the medial malleolus and anterior crest at midshaft) are indicated.

prepared and then poured to fill around the bone up to the top of the pipe section. After this pour had set, the specimen was flipped upside down and any gaps or voids left at the bottom of the cement were filled. Once the cement was fully set, each specimen was weighed. Subsequent to potting, strain gauges were applied to each bone (Figure 3-2). Two different protocols were used for strain gauge placement. For the first protocol (used for eight of the specimens), two rectangular stacked rosettes were applied, one at the distal and one proximal end. For the second protocol (used for the remaining four specimens), only the proximal rosette was applied, and three uniaxial gauges were applied around the bone's circumference in place of the distal rosette. These specimens were used to develop and test methods for estimating internal bone loads based on strains taken from the bone's surface, which will be discussed in further detail in Chapter 4.

The rosettes (UFRA-5-350-23-3LT, Tokyo Sikki Kenkyujo, Japan) were placed along the posterior surface of the bone. Laser levels were used to scribe lines along this surface for the placement of the rosettes. The distal rosette was placed 50 mm from the edge of the plafond and the proximal rosette was placed 50 mm from the bone-cement interface. The locations of the gauges were first roughly estimated and marked, and then the bone in that region was sanded to remove any remaining soft tissue and the periosteum. A drop of cyanoacrylate adhesive was then applied to the sanded area and spread by applying finger pressure through a piece of clear tape. This glue was meant to serve as a protective layer between the gauges and any fluids internal to the bone. Once the drop of adhesive had dried, the tape was removed and the newly-applied glue was sanded smooth. The strain gauge rosette was then affixed to the bone with glue, with the

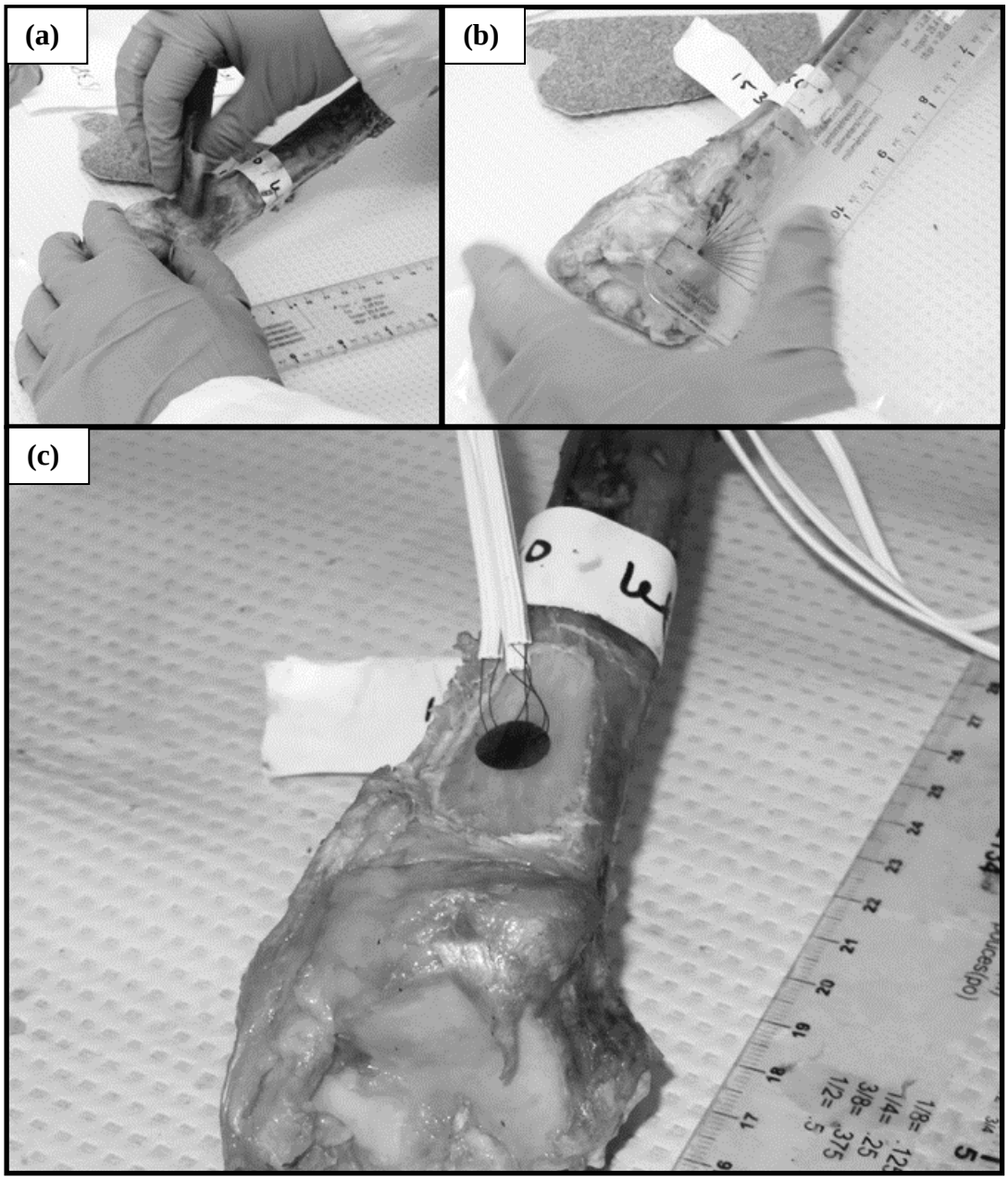

Figure 3-2: Strain Gauge Application Process.
The images show a stacked 45 degree strain gauge rosette being applied at the distal location on a specimen (50 mm from the plafond). (a) First, the specimen was sanded at the approximate location of the gauge to remove soft tissue and the periosteum and to provide a smooth surface for application of the rosette. (b) The desired location of the gauge was then measured and marked. (c) Using cyanoacrylate, the rosette was aligned by its central gauge and applied to the sanded bone.

central gauge in each rosette aligned with the scribed posterior line. After a minute, the pressure was removed from the gauge, and the tape was carefully peeled off. The gauge was sealed by applying a protective polymer top coat. Specimens were returned to the freezer after this process and remained there until testing. Prior to testing, they were thawed for a minimum of four hours.

3.2.2 Cadaveric Impact Test Protocol

Impact testing was conducted in a custom-built test apparatus (Figure 3-3). Each specimen was installed in a mounting fixture using set screws and suspended in the test chamber. The specimen was installed so that the proximal surface faced approximately upwards within the test chamber. The distal articular surface rested against a rapid-prototyped artificial talus that was based off of CT geometry extracted from a full cadaveric left lower leg specimen. Because only one specimen was available for geometry extraction, the part was mirrored to generate a "right" talus in addition to the left talus generated from the original geometry. The appropriate talus was used for each test.

The specimen was rotated about its long axis within the mounting fixture and its height within the test chamber was adjusted to achieve optimal contact between the talus and the distal articular surface. Contact was evaluated by visual inspection and the goal was to have the largest mating surface area possible.

In order to vary the simulated occupant posture, two different leg angles were set to simulate two different postures: 15° and 30° from the horizontal and, correspondingly, the line of impact. One specimen from each donor was tested at the 15° posture, with the

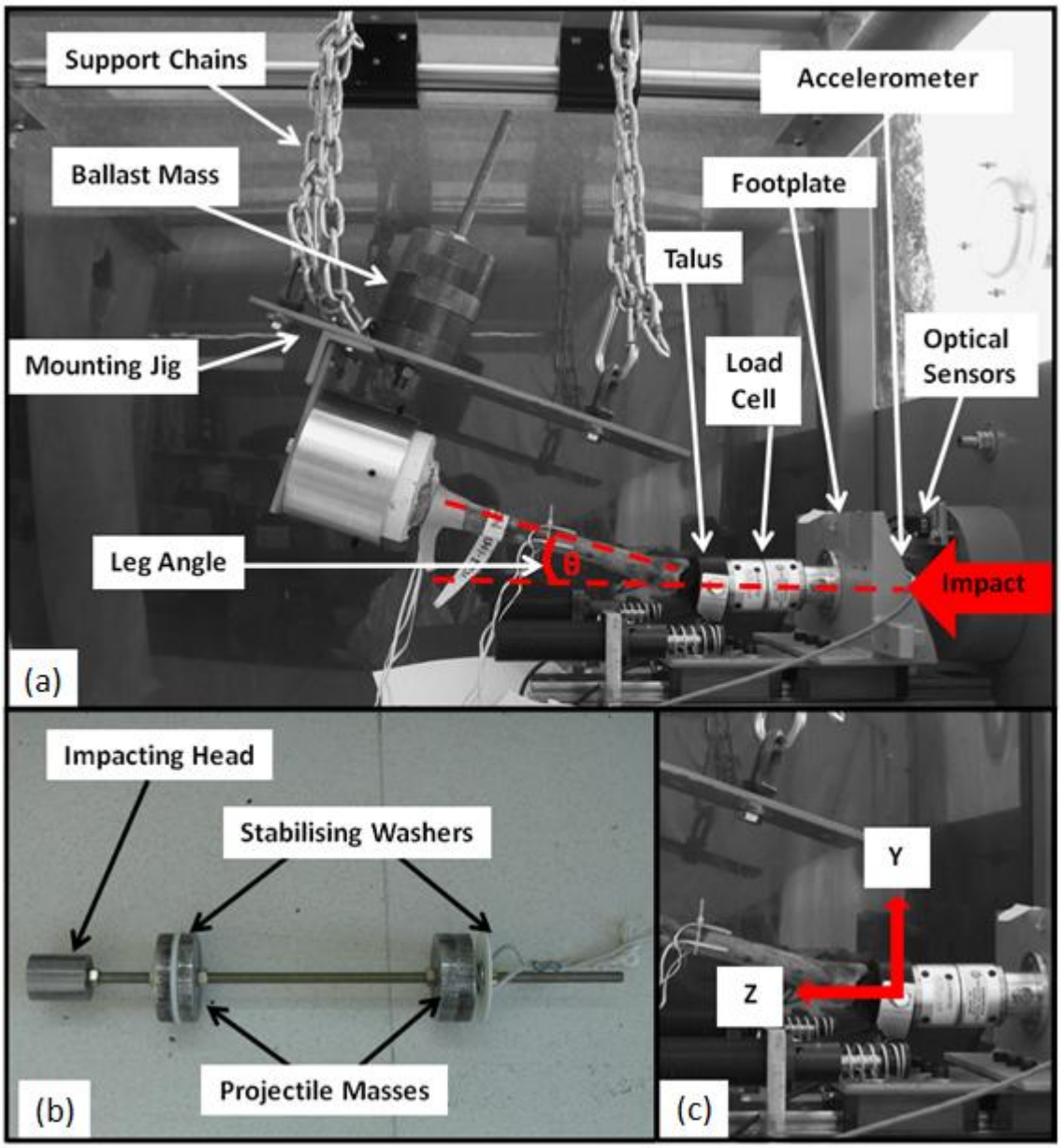

Figure 3-3: Components and Configuration of Test Set-Up
(a) Direction of impact, leg angle, important mechanical components, and instrumentation are identified in this photo of the set-up in the test chamber prior to impact; (b) projectile components; (c) key directions z and y based on the external load cell's coordinate system.

contralateral at 30°, with right and left specimens split equally between the groups. The angle was set by changing the lengths of the suspension chains used to hold the specimen up within the test chamber (Figure 3-3a). A protractor was used to check the angle of the specimen's diaphysis relative to horizontal. Ballast masses were added to the mounting fixture to simulate the inertial effects of the rest of the leg during a frontal collision. The total mass was targeted to be 12.9 kg, which corresponds to the mass of a 50^{th} percentile male adult leg (Huston 2013). This allowed for direct comparison with the ATD tests that were later conducted using 50^{th} percentile male legforms.

During a test, impulse was delivered to the specimen by the projectile. The projectile, as mentioned in Chapter 2, has a modular design consisting of a length of threaded rod, a steel impacting head, two nylon stabilising washers, and steel masses that can be added or removed to change the overall mass of the projectile (Figure 3-3b). The projectile was propelled by the pneumatic system down an acceleration tube towards the test chamber. Two optical sensors (PZ-V31P, Keyence Corporation, Osaka, Japan) mounted over the projectile head's point of entry into the chamber were used to calculate velocity by dividing the distance between the sensors by the difference in their activation times. The head of the projectile did not strike the specimen directly but instead hit an intermediate footplate. An accelerometer (MMA1200, Freescale Semiconductor, Austin, TX, USA) was fixed to the back of the footplate and a six axis load cell (IF-625, Humanetics Innovative Solutions, Plymouth, MI, USA) was mounted to the front. The key loads measured by this device will be referred to using the following symbols: F_z (horizontal force, in line with the projectile's travel), F_y (vertical force), M_x (moments

about a horizontal axis perpendicular to the projectile's travel, corresponding to moments induced by posteroanterior bending). Resultant forces and moments were also taken by summing load vectors in directions of interest (Figure 3-3c). The previously-mentioned rapid prototyped talus was mounted to the other end of this load cell.

The apparatus was controlled using a custom-written LabVIEW (National Instruments, Austin, TX, USA) program. Signals were collected with a National Instruments data acquisition system (PXIe-8135, National Instruments, Austin, TX, USA) at 50 kHz. Video was captured at 1250 frames per second by a high speed camera (IL3 100-L, Fastec Imaging Corporation, San Diego, CA).

A projectile impact velocity of 6 m/s was chosen, in order to be in the range of the results of a frontal crash simulation by Crandall *et al.* (1998) that reported a floor velocity of 5 m/s. Similarly, an impact duration of 20 ms was targeted for each strike to correspond to a value representative of an automotive collision (McKay & Bir 2009). The projectile's mass was incremented between trials to keep these conditions constant while also increasing load. Only two strikes were intended to be delivered to each specimen: one sub-failure impact, and one failure impact. This allowed for identification of the magnitudes of load between which failure occurs while minimising accumulated damage. Visual inspection of the distal tibia was performed after each impact. Repeated testing also allowed for the collection of sub-failure strains, which may be used in the validation of future finite element studies modelling impact to the tibia.

Two specimens (1640R and 1653L) were used for pilot testing to find an appropriate starting mass. In the pilot protocol, specimens were first struck with a

projectile of 11 kg, with mass increased by approximately 3 kg for each subsequent strike. Based on the results of this protocol, the rest of the specimens were first impacted with a projectile mass of 17 kg, with mass increased approximately 3-4 kg for each subsequent strike. These steps were taken to reduce accumulated damage. Failure was considered to have occurred when it was seen that the bone had split into two distinct sections. This did not include cracks in the articular cartilage that did not extend into the epiphysis.

3.2.3 ATD Impact Test Protocol

Impact testing was also performed on two ATDs: the Humanetics Hybrid III 50th percentile male and the Humanetics MIL-LX legforms. The goal of this testing was to compare the legforms' performance, and to find the magnitudes of load sensed by the legforms' internal load cells under conditions similar to those created during the cadaveric impact testing. These loads may be used in the development of new limits for off-axis impact testing.

Instead of using the potting fixture, each device was bolted into the mounting fixture by the legform's knee clevis (Figure 3-4). The ballast mass was adjusted to keep the total mass of the specimen at 12.9 kg. Custom-made acrylic angled wedges (Appendix E) were used to cover the end of the distal load cell and were fixed in place using the mount typically used for the attachment of the ATD's foot. The wedges were machined so that their impacting faces would be flush with the intermediate plate when the device was installed, providing a large surface area over which load could be distributed, and keeping the distal load cell protected against point loading.

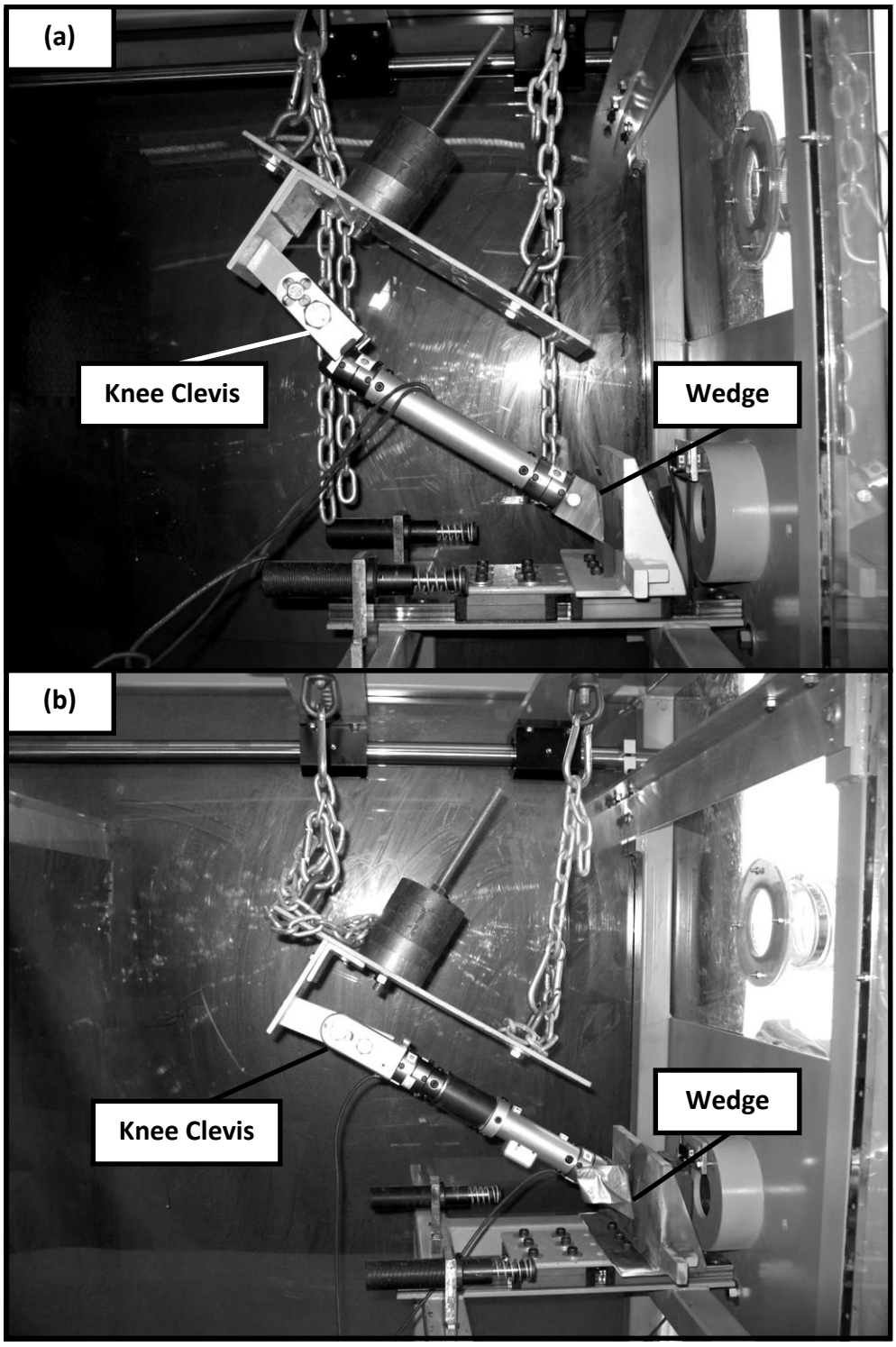

Figure 3-4: ATD Test Set-Up
Shown above are the (a) Hybrid III and (b) MIL-LX legforms, each secured in the mounting jig by the knee clevis. The photos show both legforms at a 30° leg angle.

Because it was known that the stiffness of the Hybrid III is higher than that of natural bone (Quenneville & Dunning 2012), it was unlikely that it would be able to sustain the magnitude of impacts delivered to the cadaveric specimens, even in the non-injurious tests, without exceeding the devices' load capacities. Therefore, impacts were delivered (all at approximately 6 m/s) starting with a small projectile. Mass was increased in small increments, while the changes in the measured loads were monitored.

For each projectile mass, five impacts were performed in order to assess the consistency of the measurements. The loads were later averaged within each projectile mass to assess the device's performance. The lightest projectile mass used was 6.7 kg, and the heaviest was 16.7 kg. Because it was difficult to reach the target velocity exactly, impacts were accepted if the velocity fell between 5.5 and 6.5 m/s.

3.2.4 Data Analysis

The results of all cadaveric impact tests, injurious or otherwise, were included in a best subsets regression analysis. In this analysis, the response of the model was 1 if the test resulted in fracture, and 0 otherwise. The factors included in the best subsets regression analysis were leg angle, impact velocity, projectile mass, peak acceleration of the footplate, peak F_y, peak F_z, peak resultant force (the vector summation of forces in the y and z directions), peak resultant moment (the vector summation of moments in the x and y directions), and applied impulse (the summation of impulse vectors, themselves the integral of force-time curves extracted from the load cell, in the x, y, and z directions). A model was chosen based on the best value of adjusted R^2.

Paired t-tests were performed to compare the values obtained from specimens held in the 15° posture versus those held in the 30° posture. These values were inspected for a statistically significant difference, with $\alpha = 0.05$ for all tests. Resultant force vectors were also compared in terms of their direction and magnitude. The angles of these vectors were calculated using the constituent force magnitudes in the orthogonal z and y directions at the time point at which the peak resultant force was achieved.

TI values were also computed for all injurious tests, as well as the test preceding fracture for each specimen. The formulation suggested by Kuppa and Wang (2001) was used for its critical values. The force value was taken as the magnitude of resultant force, as this was thought to be the closest available analog to the axial force measured by an ATD legform's in-line load cell. The moment value was taken as the resultant moment measured by the external load cell (the vector summation of moments about the x and y axes), again to provide the best analog to moments measured by an ATD's in-line load cell.

A Weibull model was used to generate injury risk curves based on the results of the cadaveric testing as well. The factors used to predict injury risk were: the linear equation generated by the best subsets regression analysis, the peak resultant force measured by the load cell, and TI value.

Finally, curves were generated to investigate the relationship between loads measured by an in-line load cell from an ATD and projectile mass (holding projectile velocity constant across all trials). These curves were made using the mean load value for each projectile mass used. The curves were compared between postures to see how leg

angle affected each legform's sensitivity to increased projectile mass. TI values were also computed to compare the predicted injury risk to what was actually observed in the cadaveric tests, and these values were used to generate another set of curves.

A Weibull model was used to determine the projectile mass corresponding to 10% and 50% injury risk across all of the cadaveric impact tests, and this critical mass was substituted into the equations for the mass-force and mass-TI curves. The projected ATD forces and TI values were used to compare the results of this work against previously-established load limits.

3.3 Results

3.3.1 Results of Cadaveric Impact Testing

Fractures were produced in all specimens (Figure 3-5). On average, it took a mean (standard deviation) of 2.7 (0.9) strikes to produce fracture. The targets for impact characteristics were a velocity of 6 m/s and a duration of 20 ms for all tests, and the mean (standard deviation) achieved velocity across all impacts was 6.0 (0.8) m/s and the duration of impact was 22.3 (8.8) ms.

The data gathered in trials resulting in fracture were summarised for both postures tested (Table 3-1, Table 3-2).

The results of the best subsets regression analysis indicated that the best linear model would incorporate leg angle, projectile mass, peak F_z, peak resultant force, and peak resultant moment. The model was chosen based on the highest possible adjusted R^2 value of 0.61.

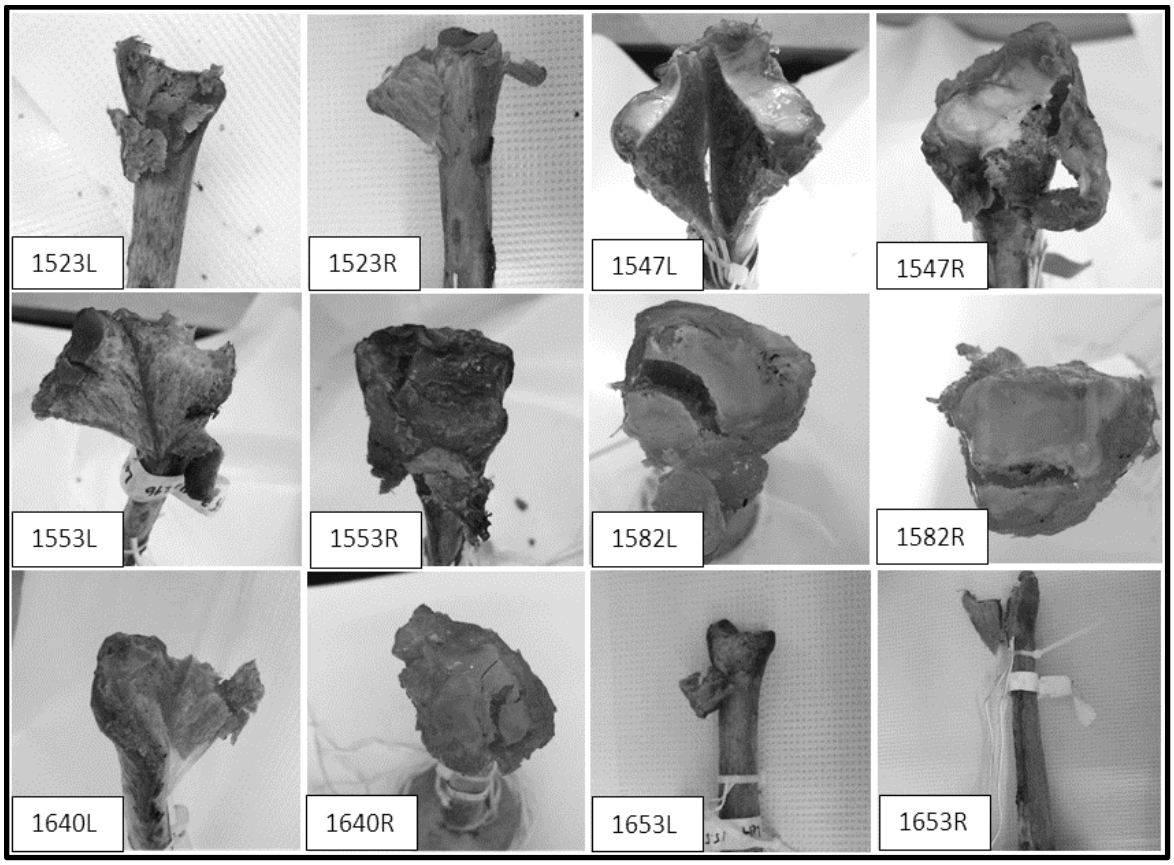

Figure 3-5: Fractures Produced in All Specimens Tested
All photos are of the distal tibia, with fracture defined as the bone being in at least two distinct pieces.

Table 3-1: Results of Fracture Impact Tests for 15° Specimens

Data taken from impact tests resulting in fracture for specimens assigned a 15° leg angle.

Specimen	**Projectile Mass (kg)**	**Peak Footplate Acceleration (g)**	**Peak F_y (N)**	**Peak F_z (N)**	**Peak Resultant Force (N)**	**Peak Resultant Moment (Nm)**	**Impulse (Ns)**
1547L	21	153.0	4419	5540	7064	214	30.7
1582L	25	66.5	2392	6823	7319	124	21.3
1640L	21	164.4	3272	6186	6316	133	19.9
1653R	21	196.8	3048	8663	8849	139	21.8
1523R	25	76.8	2730	4136	4838	135	25.8
1553R	28	123.8	2821	4606	5422	133	30.1

Table 3-2: Results of Fracture Impact Tests for 30° Specimens

Data taken from impact tests resulting in fracture for specimens assigned a 30° leg angle.

Specimen	**Projectile Mass (kg)**	**Peak Footplate Acceleration (g)**	**Peak F_y (N)**	**Peak F_z (N)**	**Peak Resultant Force (N)**	**Peak Resultant Moment (Nm)**	**Impulse (Ns)**
1547R	21	158.2	4129	4596	5628	196	20.4
1582R	28	100.5	4573	6115	7554	209	39.5
1640R	17	72.6	2635	2711	3780	140	21.8
1653L	21	120.2	3770	4414	5484	107	27.5
1523L	21	117.5	4183	5530	6403	205	21.3
1553L	21	121.3	1177	3612	4954	179	22.3

It was noted that in some cases, peak forces, peak moments, and applied impulse were not highest in the impact leading to fracture but in a prior test (Figure 3-6). As such, the highest overall value was considered in the paired t-test analysis as well as fracture values in order to represent the maximum tolerance of the bone. The number of impacts, highest achieved value of resultant force, and highest achieved value of TI are summarised in Table 3-3**Table 3-3**.

Many of the strain gauge rosettes were damaged between their application and the time of data collection due to broken leadwire connections. Principal strains were calculated from each rosette for both the injurious trial and the last non-injurious trial, but due to the small number of rosettes left intact, no statistically significant trends could be observed in the strain magnitudes in terms of posture or location. The strain magnitudes are included in Appendix F.

3.3.2 Effect of Leg Angle on Impact Characteristics Leading to Fracture

There was a statistically significant difference ($p=0.032$) between the peak resultant forces measured in the 15° and 30° cases (Figure 3-7a). For the 15° case, the mean (standard deviation) resultant force was 7516 (910) N, and for the 30° case, the mean (standard deviation) resultant force was 5822 (1649) N. There was also a statistically significant difference between the highest achieved values of force in the z direction ($p = 0.027$) (Figure 3-7b). Again, the fracture force tended to be higher in the 15° case. For the 15° case, the mean (standard deviation) F_z value was 6791 (1048) N, and for the 30° case, the mean (standard deviation) value was 4661 (1463) N.

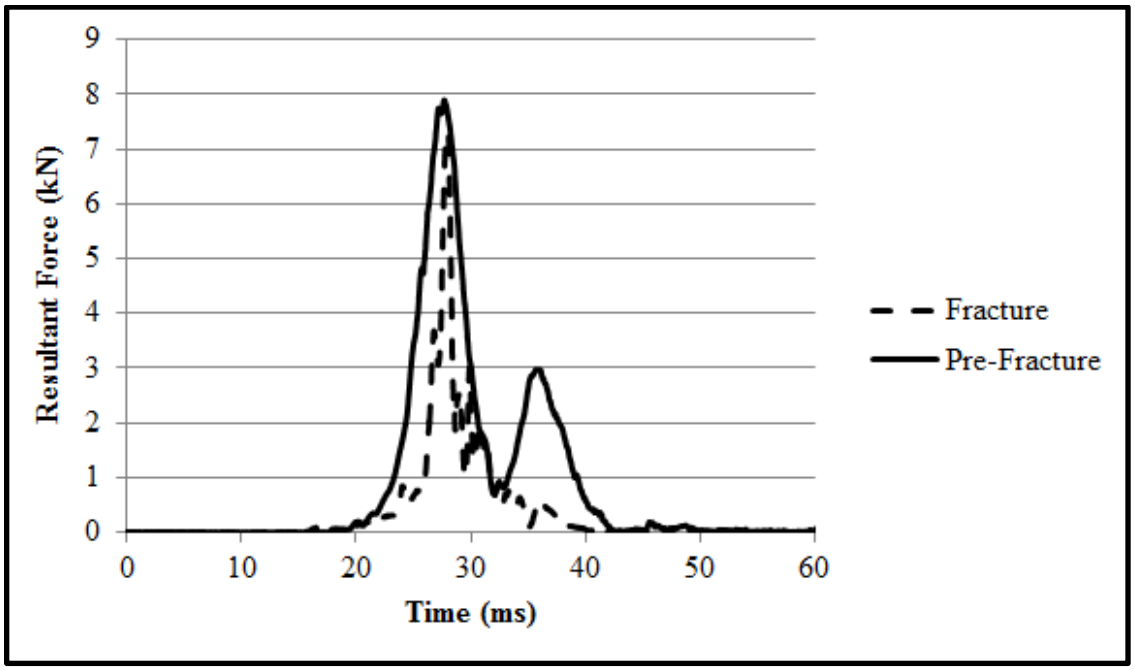

Figure 3-6: Comparison of Force-Time Curves in Fracture vs Pre-Fracture Tests
Force-time curves are shown for a representative specimen (1582L). Note that in the case of fracture, the area under the curve is much smaller than in the case preceding fracture, despite the fact that the peak resultant forces are similar.

Table 3-3: Summary of Repeated Impacts and Highest Achieved Loads

Because loads were not always highest in the impact resulting in fracture, pertinent pre-fracture data is summarised. For each specimen, the number of strikes required to produce fracture, the highest achieved values of resultant force and TI as measured by the external load cell, and the point in testing at which these highest achieved values occurred are listed.

Specimen	Number of Strikes to Failure	Highest Resultant Force (N)	Strike on Which Highest Resultant Force was Achieved	Highest TI Value	Strike on Which Highest TI Value was Achieved
1547L	2	7064	2nd	1.48	2nd
1547R	2	5628	2nd	1.29	2nd
1582L	3	7893	2nd	1.46	2nd
1582R	4	8683	1st	1.86	1st
1640L	1	6316	1st	1.08	1st
1640R	3	3780	3rd	0.90	3rd
1653L	4	5484	4th	1.01	2nd
1653R	2	8849	2nd	1.41	1st
1523L	2	6403	2nd	1.39	2nd
1523R	3	8023	2nd	1.63	2nd
1553L	2	4954	2nd	1.16	2nd
1553R	4	6949	2nd	1.29	2nd

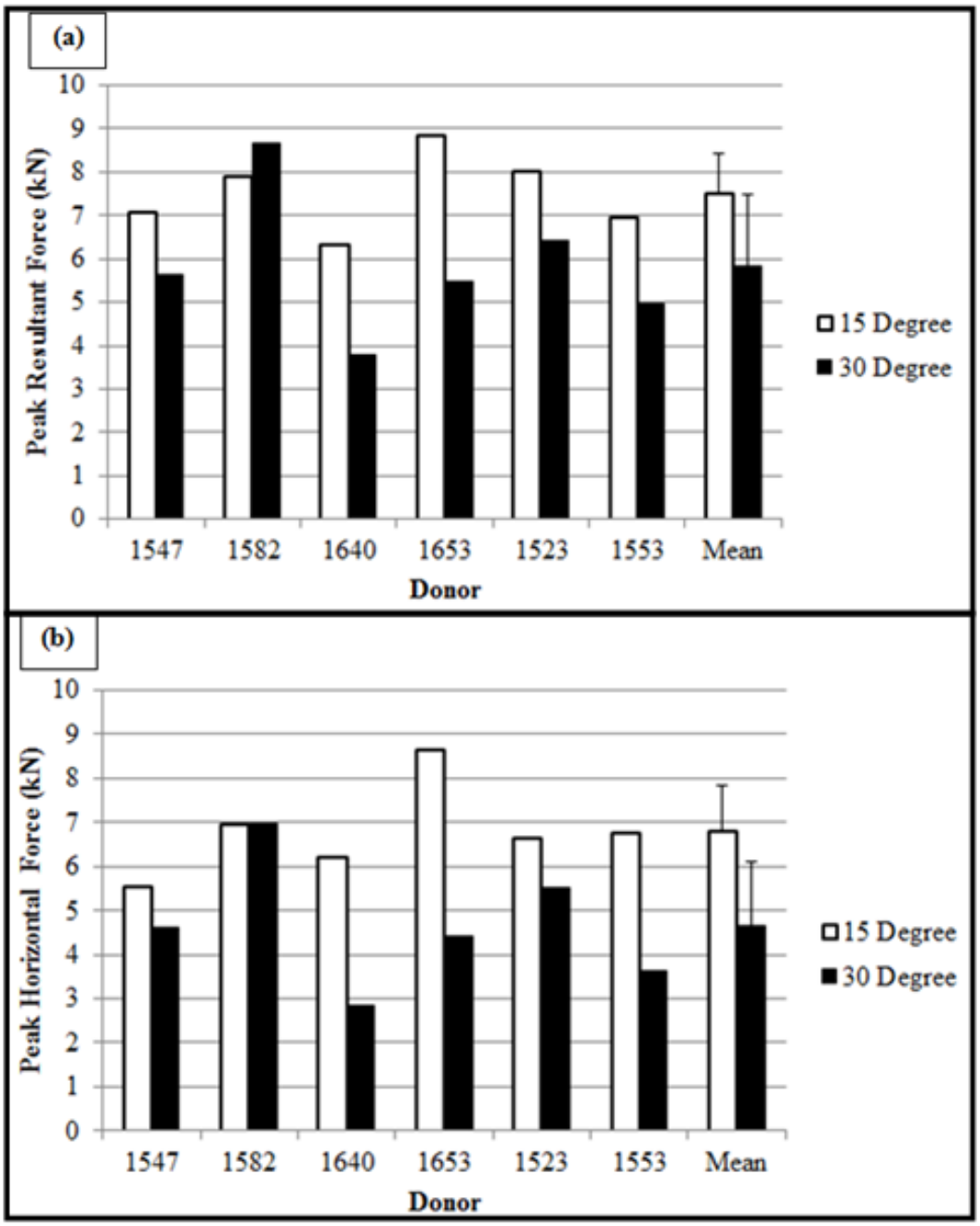

Figure 3-7: Comparison of Highest Achieved Forces Between Postures
The figures show the highest achieved (a) resultant force magnitude and (b) horizontal force (F_z) in each specimen, compared by posture. Mean values of force are provided with error bars representing standard deviation.

The resultant force vectors were also compared in terms of their directions.

The vectors were plotted (Figure 3-8), and their angles were calculated from trigonometry. The directions varied quite a bit among the specimens tested at 15°, for which the mean (standard deviation) angle was 25 (11)°. For the specimens tested at 30°, the variation was much less, with a mean (standard deviation) value of 42 (4)°. Despite the variations, there was a statistically significant difference (p=0.006) in the angles of the vectors between the two tested postures. Values that were tested but found to not be significantly different between the two postures included fracture projectile mass (p=0.230), velocity (p=0.841), acceleration (p=0.537), impact energy at fracture (p=0.555), impulse at fracture (p=0.906), peak impulse achieved (p=0.420), vertical force (F_y) at fracture (p=0.630), highest achieved vertical force (p=0.570), horizontal force (F_z) at fracture (p=0.134), resultant force at fracture (p=0.235), resultant moment at fracture (p=0.236), and highest achieved resultant moment (p=0.860).

Because resultant moments were used to calculate TI, they were also graphed (Figure 3-9). For the specimens tested at a leg angle of 15°, the mean (standard) resultant moment was 146 (34) Nm, and for the specimens tested at 30°, this value was 173 (41) Nm.

3.3.3 Performance of Tibia Index

The TI values are listed in the table below (Table 3-4) for the pre-fracture and fracture tests for each specimen. Pre-fracture cases in which the TI value was lower than 1.16 are highlighted in green, as are fracture cases in which TI exceeded this value (*i.e.* when the TI's prediction was correct). Therefore, cases not highlighted in green represent

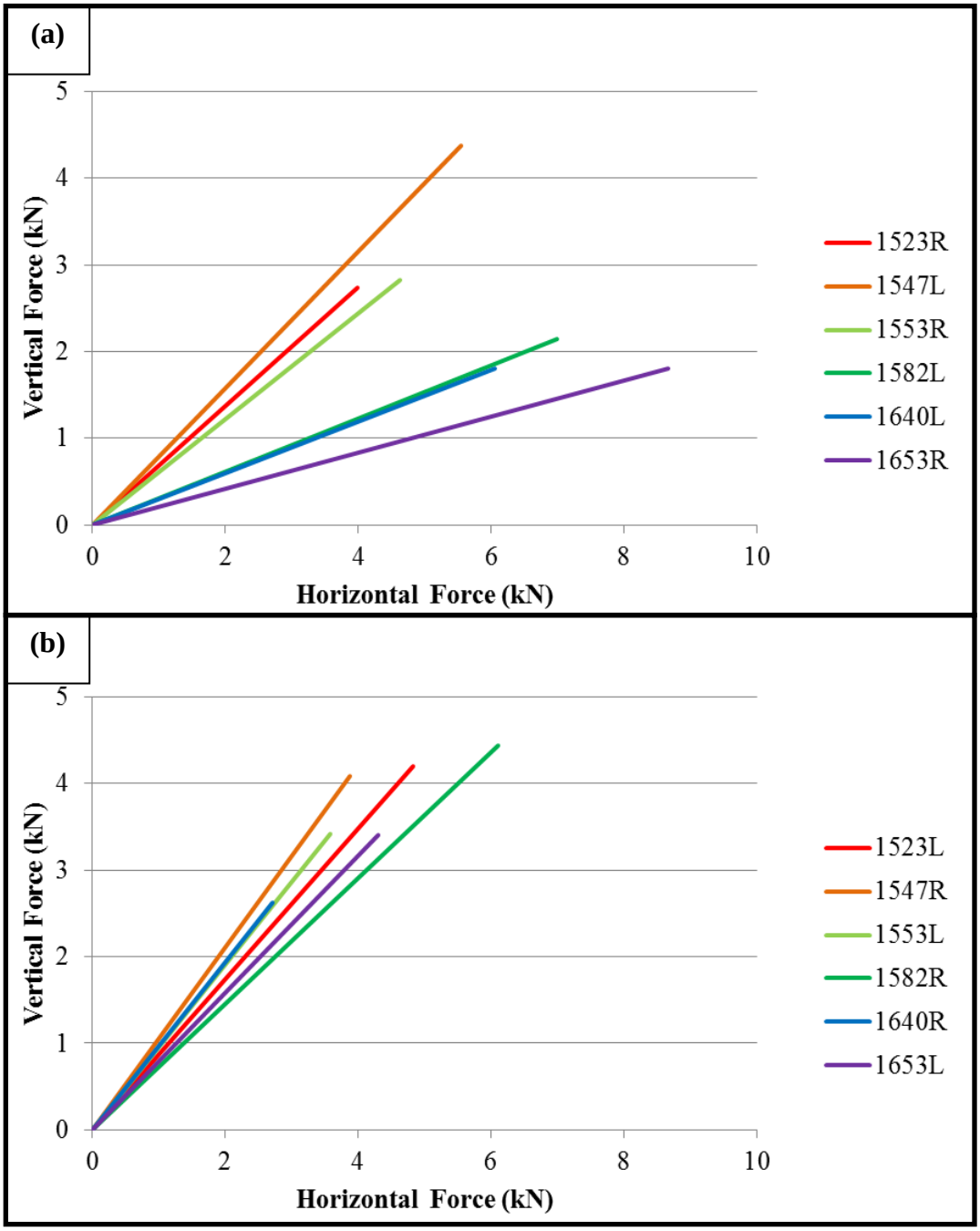

Figure 3-8: Resultant Force Vectors
Values taken from fracture tests. Specimens within the same pair have been assigned the same colour in the two graphs, with (a) showing angles for specimens held at 15° and (b) showing angles held at 30°.

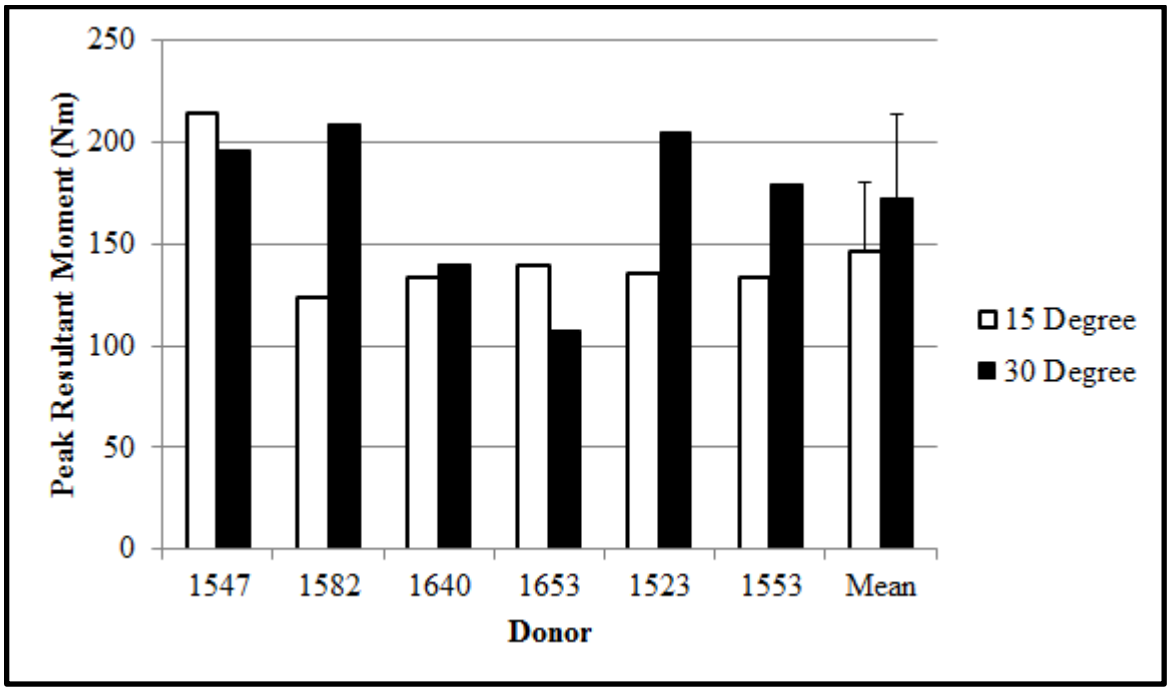

Figure 3-9: Peak Resultant Moment Compared by Leg Angle
The figures show the highest achieved resultant moment in each specimen, compared by posture. Mean values of force are provided with error bars representing standard deviation.

Table 3-4: Tibia Index Values for Pre-Fracture and Fracture Impact Tests

TI values computed from resultant forces and moments measured by the external load cell and evaluated based on the injury risk curve generated by Kuppa & Wang (2001) for their formulation of TI. Pre-fracture values highlighted in green had TI values corresponding to less than 50% fracture risk and fracture values highlighted in green had TI values equal to or exceeding 50% fracture risk.

Specimen	Pre-Fracture Tibia Index Value	Fracture Tibia Index Value
1547L	0.75	1.48
1547R	0.89	1.29
1582L	1.46	1.13
1582R	1.48	1.50
1640L	-	1.08
1640R	0.87	0.90
1653L	0.90	0.90
1653R	1.41	1.32
1523L	0.69	1.39
1523R	1.63	0.96
1553L	0.69	1.16
1553R	0.85	1.01

either pre-fracture strikes in which TI exceeded 1.16 or fracture strikes in which TI was lower than 1.16.

3.3.4 Injury Risk Curves

The results of the best subsets regression analysis were used to generate a linear equation for injury risk (Equation 3-2):

$$\begin{aligned} Fracture\ Risk = {} & 0.085 + 0.01197 * Leg\ Angle\ (degrees) \\ & - 0.03415 * Impulse\ (Ns) - 0.000266 * F_z\ (N) \\ & + 0.000403 * Resultant\ Force\ (N) \\ & - 0.00431 * Resultant\ Moment\ (Nm) \\ & + 0.0407 * Projectile\ Mass\ (kg) \end{aligned}$$

Equation 3-2

This linear equation was used to generate injury risk curves using a Weibull survivability model for a general case as well as posture-specific cases for the two leg angles tested (Figure 3-10). The R^2 value for the general Weibull model was 0.93, 0.92 for the 15°, and 0.96 for the 30°.

As most of the previous experimental studies on fracture tolerance in the lower leg use force as the sole predictor, the Weibull model was also applied to the highest achieved resultant force values for each posture (Figure 3-11). According to these models, for the 15° posture (R^2 = 0.93), a resultant force of 5.9 kN corresponds to a 10% risk of fracture. For the 30° posture (R^2 = 0.86), the corresponding force value is 3.3 kN.

The model was also applied to the highest achieved values of Tibia Index based on the formulation used by Kuppa and Wang (2001) (Figure 3-12). In that formulation, a TI value of 1.16 was reported to correspond to a 50% fracture risk. In the model

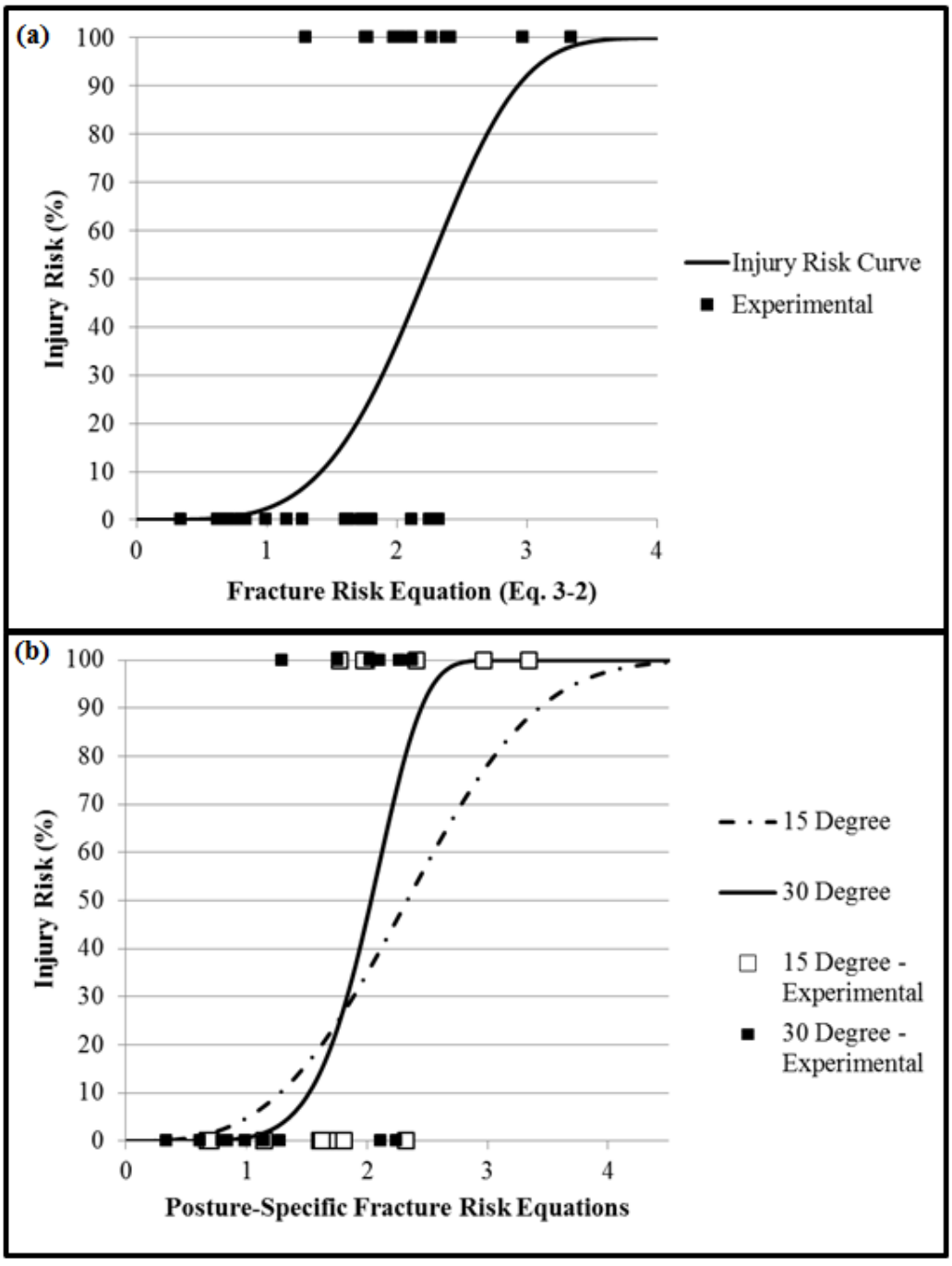

Figure 3-10: Injury Risk Curves Based on Leg Angle, Impulse, Forces, Moment, and Projectile Mass

(a) Injury risk curve for all specimens, and (b) posture-specific injury risk curves. Experimental data provided for reference, either at 0% (for non-fracture values) or 100% (for fracture values).

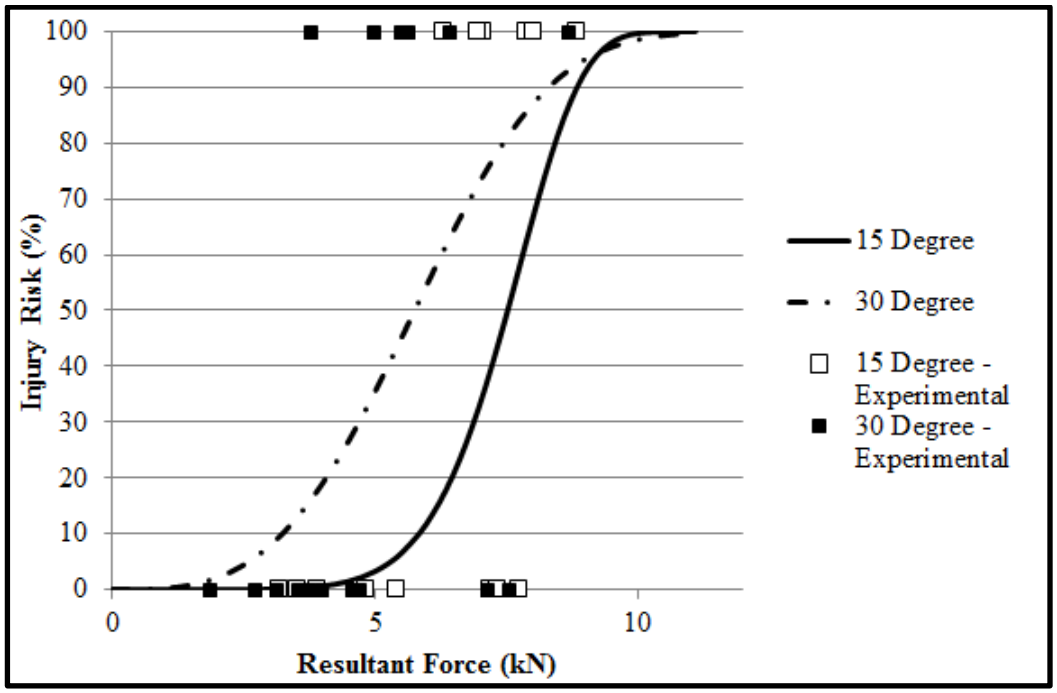

Figure 3-11: Posture-Specific Injury Risk Curves Based on Resultant Force
Experimental data provided for reference.

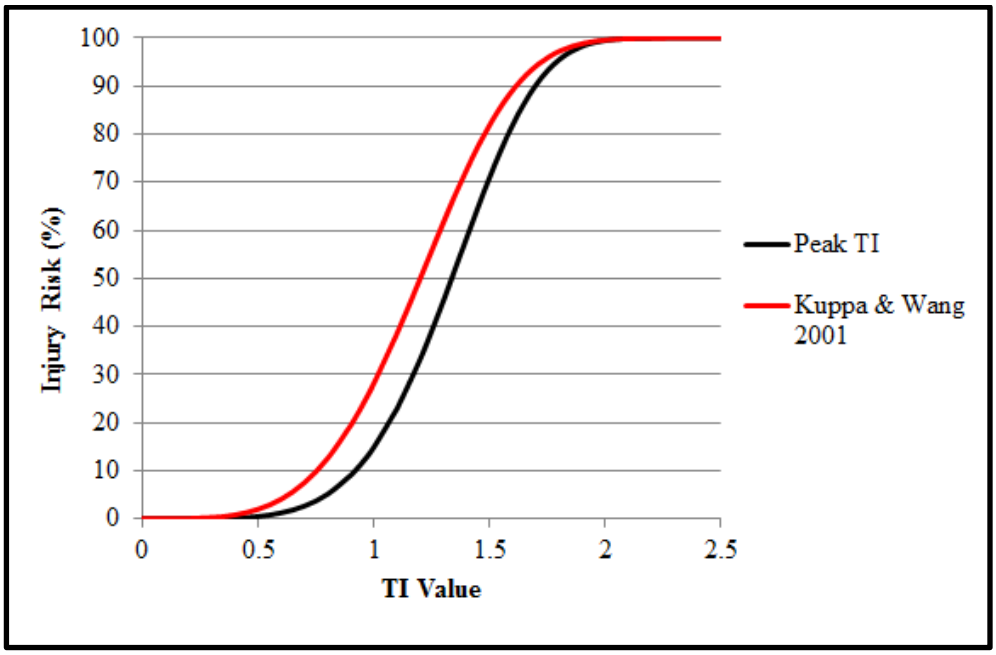

Figure 3-12: Injury Risk Curve Based on Tibia Index Values

Data from the current study was used to generate a curve that can be compared to the one proposed by Kuppa and Wang (2001). Kuppa and Wang predicted that a TI value of 1.16 would correspond to 50% fracture risk, while the equivalent value for this study was higher at 1.33.

developed based on the current work (R^2 = 0.97), a TI value of 1.33 corresponds to a 50% fracture risk.

3.3.5 Evaluation of ATD Performance Under Off-Axis Impact

The mean (standard deviation) velocity of all impact tests performed on the Hybrid-III legform was 6.0 (0.21) m/s. The average distal axial force and the projectile mass from each set of impacts were fit to a linear model (R^2=0.99 for the Hybrid-III tested in the 15° posture and R^2=0.94 at 30°). The legform was more sensitive to mass changes (*i.e.*, had a steeper slope) in the 15° posture than in the 30° posture (Figure 3-13a).

The mean (standard deviation) velocity of all impact tests performed on the MIL-LX legform was 5.9 (0.22) m/s. Forces were taken from the proximal load cell, and mean forces were plotted against projectile mass, and the data were fit to linear models. For the 15° posture, R^2=0.99, and for the 30° posture, R^2=0.97. Like the Hybrid III, this legform was more sensitive to mass changes in the 15° posture than the 30° posture. However, the difference in slope was much less than for the Hybrid III (Figure 3-13b).

Tibia Index values were also computed for each impact and averaged as the axial force values had been to generate TI-mass plots (Figure 3-14). Again, the data were fit to linear models. The R^2 values for these models were 0.94 for the Hybrid III in the 15° posture, 0.85 for the Hybrid III in the 30° posture, 0.94 for the MIL-LX in the 15° posture, and 0.80 for the MIL-LX in the 30° posture.

A Weibull injury risk model was generated for projectile mass based on the results

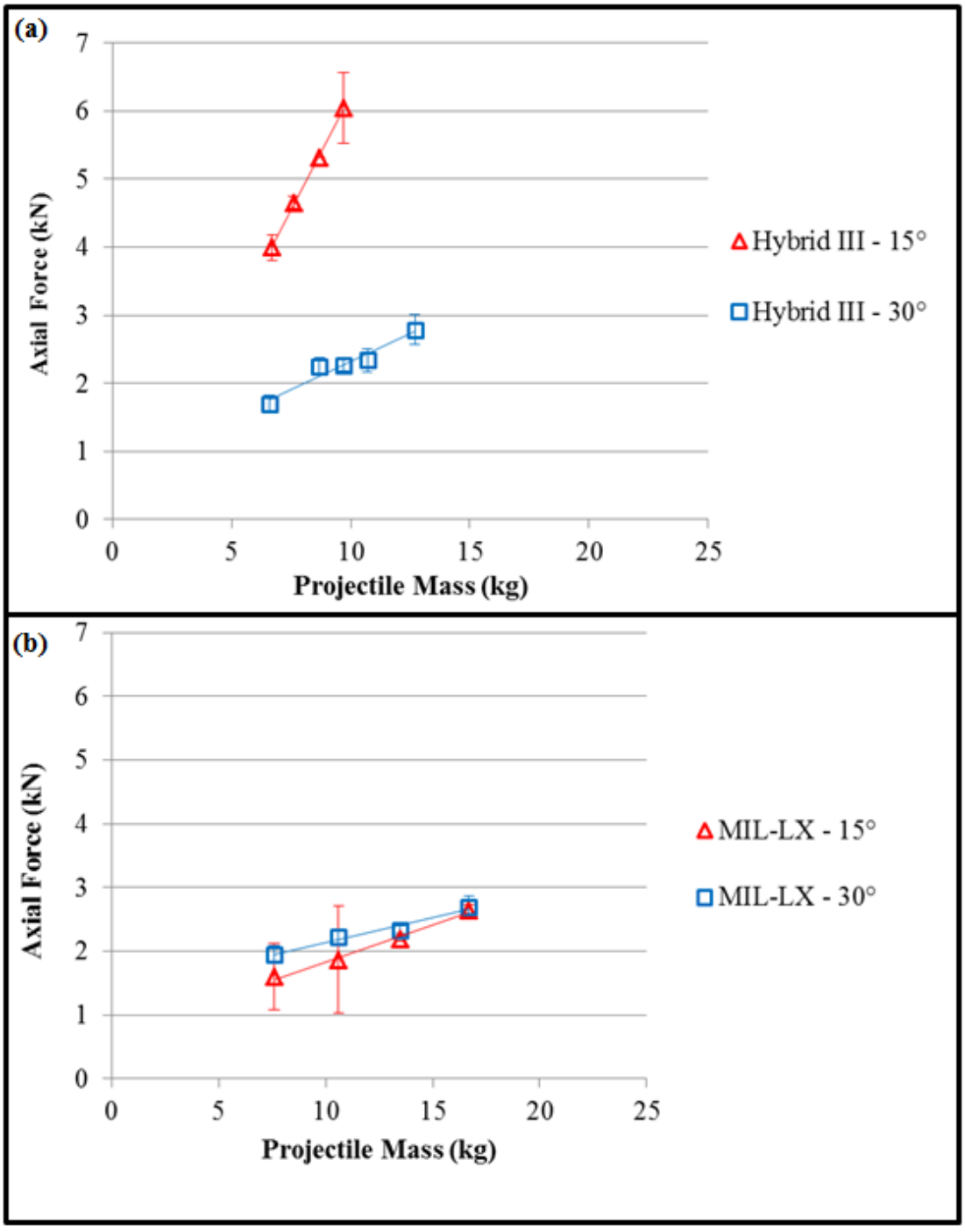

Figure 3-13: Force-Mass Curves for ATDs
Posture-specific curves for (a) the Hybrid III legform and (b) the MIL-LX legform. Standard deviations are indicated by error bars.

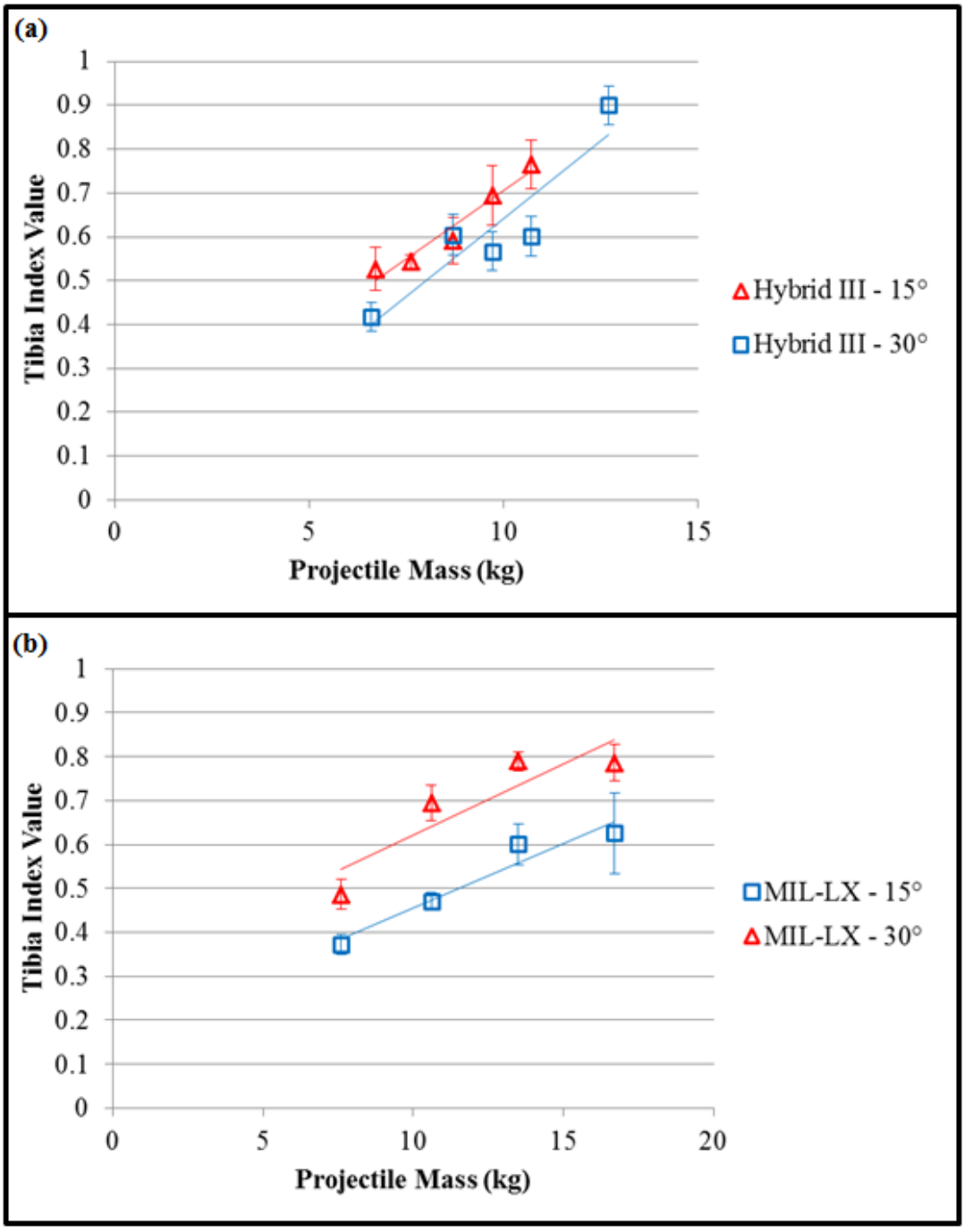

Figure 3-14: TI-Mass Curves for ATDs
Posture-specific curves for (a) the Hybrid III legform and (b) the MIL-LX legform. Standard deviations are indicated by error bars.

of the cadaveric impact data. In order to estimate the loads that would have been measured under the conditions producing fracture in a cadaveric specimen, the linear models were extrapolated to the masses corresponding to 10% and 50% injury risk in the cadaveric impact tests (16.7 and 22.7 kg, respectively) (Table 3-5).

3.4 Discussion

This study examined the tibia's response to complex loading that may be seen in a real automotive collision due to posture variations, and compared the effects of two different postures on fracture tolerance at the distal tibia. The resulting off-axis loading had not previously been investigated in depth experimentally.

Impacts were applied incrementally to each bone until fracture. During the repeated testing, impulse was observed to decrease between the pre-fracture and fracture strikes. This is likely due to the dissipation of energy as a crack propagated through the bone.

Based on the results of the best subsets regression analysis, the best predictors of injury risk were leg angle, projectile mass, peak F_z, peak resultant force, and peak resultant moment. This is much more complex than the risk functions generally used in the literature (which commonly use axial force, age, or TI value) (Yoganandan *et al.* 1996; Quenneville *et al.* 2011; Kuppa & Wang 2001), and indicates that values besides those typically considered may be of interest in future studies. However, this exact linear combination would not be useful unless the test set-up used in this work was recreated, since many of the parameters are specific to the methods used.

These values, as well as others collected during testing, were compared between

Table 3-5: Projected Measured ATD Forces Under Injurious Conditions
Linear force-mass and TI-mass curves for each legform in each posture were extrapolated to projectile masses corresponding to relevant injury risk levels from cadaveric testing.

Legform	**Posture (°)**	**Projected Force at 10% Risk Condition (kN)**	**Projected TI Value at 50% Risk Condition**
Hybrid-III	15	10.7	1.49
Hybrid-III	30	3.4	1.54
MIL-LX	15	2.6	0.82
MIL-LX	30	2.7	1.04

the two tested postures. It was found that while most of the values compared were similar between the two postures, there was a significant difference in the specimen's highest achieved F_z and resultant force magnitudes. In both cases, the specimens held in the 15° could withstand higher force magnitudes than the 30° specimens. The mean values of resultant force were 7.5 kN for the 15° posture, and 5.8 kN for the 30° posture. These are in the range of previously published data. Quenneville *et al.* (2011) reported an average fracture force of 12.6 kN when isolated male tibias were subjected to axial (*i.e.*, 0°) impact loading in a very similar test apparatus to the one used in this work. Due to the use of female specimens in non-axial postures, it is unsurprising that the forces required for fracture were lower in this case. It should be noted, however, that Quenneville *et al.* used very short impact durations (<10ms), which may also affect direct comparison between these studies.

The difference in injury tolerance between the postures was expected to be caused by the increased bending induced at 30° compared with 15° as a result of a larger component of off-axis loading. However, the difference in bending moments between postures was not statistically significant, and it is possible that measurements made by the external load cell did not accurately reflect loads internal to the bone. As the load cell and the specimen were not coupled in any way, there was not much potential to generate and measure high reaction loads (including bending moments) between the articular surface and the load cell. In another test configuration, these measured loads may have been higher.

The injury risk function generated based on applied resultant force found that for any given magnitude of load, the 15° posture was at less risk of sustaining an injury than the 30° posture. This was consistent with the findings of the paired t-test analysis. According to this risk function, a resultant force of 5.9 kN corresponds to 10% risk of injury in the 15° posture, while the corresponding value is 3.3 kN for the 30° posture. The value for the 15° posture exceeds the commonly cited 5.4 kN derived from axial impact tests conducted by Yoganandan *et al.* (1996). However, Yoganandan's figure came from an injury risk curve for all injuries of the foot and ankle, not just the distal tibia. The results of this analysis are consistent with those reported by Quenneville *et al.* (2011), who found in their study on axial impacts delivered to isolated tibias that a force of 7.9 kN corresponded to 10% risk.

It is important to mention that previous experimental studies on off-axis loading of the lower leg have reported that non-standard postures can reduce the risk of injury (Crandall *et al.* 1998; Gallenberger *et al.* 2013). However, these studies looked at the intact lower leg and considered injuries to structures other than the tibia. In an intact specimen, the presence of an intact fibula and talus may change the way load is distributed, mitigating the effects of off-axis loading on the tibia.

The prediction of fracture based on TI was correct in about half of the tests analysed, but the prediction was only consistently accurate (*i.e.*, true for both the pre-fracture and fracture strikes) for four of the twelve specimens tested, which suggests that the formulation used (developed based on the results of testing male specimens under

quasistatic conditions, in isolated compression and bending) may not be fully applicable to the case studied here (female specimens under off-axis dynamic loading).

In keeping with this analysis, the Weibull curve generated based on TI values showed that, for a given TI value, Kuppa and Wang's model predicted a higher risk of injury than the new model. For example, the value of 1.33 corresponding to 50% risk may be taken in place of the 1.16 reported by Kuppa and Wang. Again, this is surprising due to the use of female specimens in this work. It should also be noted that the TI values were based on the resultant force and moment values taken from an external load cell held at an angle relative to the specimen, not an inline load cell as is used in other formulations. Because the angle of the resultant force vector did not consistently match the specimen's leg angle, this is not a direct analog to the in-line loads that would be sensed by an ATD, for which TI was developed. However, it appears that some adjustment of the critical values may improve the applicability of TI to this testing configuration.

It was found that both the Hybrid III and the MIL-LX were sensitive to posture in terms of the loads they sensed. Generally, when impacted at a constant velocity with increasing mass, both legforms registered smaller changes in force in the 30° posture than in the 15° posture. However, the relationships varied greatly between legforms and postures. Projections were also made for axial force and TI limits to be used in these non-standard postures based on the results of the cadaveric testing and assuming a linear response between mass and force. Further testing may be necessary to determine whether or not the response would continue to fit a linear trendline at higher projectile masses.

In the 15° posture, the Hybrid III's projected force of 10.7 kN was much greater than the commonly-cited 5.2-5.4 kN used for axial testing(NATO 2007; Kuppa & Wang 2001), but in the 30° posture, the projected force was only 3.4 kN. This suggests that the previously-established limit should not be extended to these non-standard postures. However, the MIL-LX performed well considering its established limit of 2.6 kN for axial impacts (NATO 2011), suggesting that this limit may be extended to non-standard postures. In terms of TI values, the Hybrid III had projected values exceeding the previously published limit of 1.16 (Kuppa & Wang 2001), but the MIL-LX had projected values well under this cut-off. This may be due to the higher stiffness of the Hybrid III relative to the MIL-LX, and should be considered in the future use of these devices.

Strain gauges were frequently damaged during specimen storage, installation, and testing, and as a result could not be used for later analysis. The magnitudes of measured strains also varied greatly among specimens tested. Because of these factors, strain was not included in further analysis of injury risk. However, the strain data gathered from these tests may be helpful in the validation of future finite element studies.

Because of the non-standard postures used in this work, it proved very challenging to align each specimen prior to impact and to ensure full contact with the articular surface of the rapid-prototyped talus. Efforts were taken to ensure that alignment was consistent, but it must be considered that variation in tibial curvature and distal articular geometry may have had an effect on specimen loading. However, the two postures used were chosen to be far apart enough that the difference between them was clearly visible to the user, so that the effects of variation in the leg angle would be minimised. Additionally,

the use of both a left and right rapid-prototyped talus was hoped to improve contact at the distal articular surface.

The use of repeated testing may raise concerns about accumulated damage. The pilot test protocol allowed for adjustment of the starting projectile mass so that repeated impacts would be limited. The goal was to achieve fracture in two strikes, because if fracture was achieved on the first strike, it would be impossible to know if a lower load may have produced the same result. The mean number of strikes required to produce fracture across all specimens, including those in the pilot protocol, was 2.7 (0.9), higher than the desired two strikes. However, the collection of non-injurious data also allowed for the identification of factors other than force that may be able to predict injury risk using the best subsets regression analysis.

The testing described in this chapter has led to a better understanding of the effect of non-standard postures on the injury tolerance of the isolated tibia under impact loading. Specimens held further from an axial posture tended to have a lower tolerance to force, and factors other than force were identified as contributors to injury risk. A commonly-used injury criterion for tibia fractures was also evaluated, and it was found that the cadaveric specimens tested could withstand greater loads than this criterion would suggest. Finally, two ATD legforms were evaluated for their performance in non-standard postures, and loads were predicted corresponding to injurious conditions. The Hybrid III had very different responses in the two postures, but the MIL-LX performed well according to its previously established load limit in both configurations.

3.5 References

Crandall, Jeff R., Peter G. Martin, Edwin M. Sieveka, Walter D. Pilkey, Patricia C. Dischinger, Andrew R. Burgess, Timothy D. O'Quinn, and Carl B. Schmidhauser. 1998. "Lower Limb Response and Injury in Frontal Crashes." *Accident Analysis and Prevention* 30 (5): 667–77.

Funk, James R, Rodney W Rudd, Jason R Kerrigan, and Jeff R Crandall. 2004. "The Effect of Tibial Curvature and Fibular Loading on the Tibia Index." *Traffic Injury Prevention* 5 (2): 164–72.

Gallenberger, Kathryn, Narayan Yoganandan, and Frank Pintar. 2013. "Biomechanics of Foot / Ankle Trauma with Variable Energy Impacts." *Annals of Advances in Automotive Medicine*, no. 1997: 123–32.

Huston, Ronald L. 2013. *Fundamentals of Biomechanics*. Taylor & Francis Group.

Ivarsson, B. Johan, Abhijit Manaswi, Daniel Genovese, Jeff R. Crandall, Shepard R. Hurwitz, Christine Burke, and Samir Fakhry. 2008. "Site, Type, and Local Mechanism of Tibial Shaft Fracture in Drivers in Frontal Automobile Crashes." *Forensic Science International* 175 (2–3): 186–92.

Kuppa, S, and J Wang. 2001. "Lower Extremity Injuries and Associated Injury Criteria." In *17th ESV Conference*. Vol. No. 457.

McKay, Brian J, and Cynthia A Bir. 2009. "Lower Extremity Injury Criteria for Evaluating Military Vehicle Occupant Injury in Underbelly Blast Events." *Stapp Car Crash Journal* 53: 229–49.

Mertz, H. 1993. "Anthropomorphic Test Devices." In *Accidental Injury, Biomechanics, and Prevention*, edited by A. Nahum. Springer-Verlag.

NATO. 2007. "Test Methodology for Protection of Vehicle Occupants against Anti-Vehicular Landmine Effects. Final Report of HFM-090 Task Group 25."

NATO. 2011. "Procedures for Evaluating the Protection Level of Armoured Vehicles." Vol. 2.

Quenneville, Cheryl E, and Cynthia E Dunning. 2012. "Evaluation of the Biofidelity of the HIII and MIL-Lx Lower Leg Surrogates under Axial Impact Loading." *Traffic Injury Prevention* 13 (1): 81–85. doi:10.1080/15389588.2011.623251.

Quenneville, Cheryl E, Stewart D McLachlin, Gillian S Greeley, and Cynthia E Dunning. 2011. "Injury Tolerance Criteria for Short-Duration Axial Impulse Loading of the Isolated Tibia." *The Journal of Trauma: Injury, Infection, and Critical Care* 70

(1): E13–18.

Read, Kathleen M., Joseph A. Kufera, Patricia C. Dischinger, Timothy J. Kerns, Shiu M. Ho, Andrew R. Burgess, and Cynthia A. Burch. 2004. "Life-Altering Outcomes after Lower Extremity Injury Sustained in Motor Vehicle Crashes." *The Journal of Trauma: Injury, Infection, and Critical Care* 57 (4): 815–23.

Untaroiu, Costin D., Johan Ivarsson, Dan R. Genovese, Dipan Bose, and Jeff R. Crandall. 2008. "Biomechanical Injury Response of Leg Subjected to Combined Axial Compressive and Bending Loading." *Biomedical Sciences Instrumentation* 44 (FEBRUARY): 141–46.

Yoganandan, Narayan, Frank a Pintar, Melbourne Boynton, Paul Begeman, Priya Prasad, Shashi M Kuppa, Richard M Morgan, and Rolf H Eppinger. 1996. "Dynamic Axial Tolerance of the Human Foot-Ankle Complex." *Society of Automotive Engineers, Inc.* 962426: 207–18.

Zuby, D S, J S Nolan, and C P Sherwood. 2001. "Effect of Hybrid III Geometry on Upper Tibia Bending Moments." *Society of Automotive Engineers Biomechanics Research and Development SP1577*, no. 724: 1–14.

Chapter 4 : Development of a Strain-Based Method to Non-Invasively Measure Internal Bone Loads

4.1 Motivation

In a frontal collision, load is transmitted through the vehicle floor, applying compressive force to the plantar surface of the foot through the pedals, and this may induce loading in a range of geometrically and mechanically complex structures (including the numerous bones of the lower extremity, soft tissues, and muscles). Because of the many factors present in this scenario, it is difficult to determine the proportion of load experienced by a structure of interest (such as the tibia, for example). Additionally, curvature of the bone and variation in occupant posture makes it difficult to determine how much of a role bending plays in the bone's loading, as opposed to pure axial compression.

Anthropomorphic Test Devices (ATDs), or crash test dummies, are frequently used as tools for predicting the risk of injuries in crash scenarios. The "tibias" of many of these devices come installed with load cells in line with the leg's long axis, and the forces measured from these devices are frequently used in injury analysis. Injury limits are defined in terms of forces measured by these load cells. However, as mentioned before, it is difficult to relate these loads to those experienced by the actual tibia in an impact event, because those real loads are challenging to characterise. Therefore, it is important that researchers find a way to experimentally measure or estimate the tibia's internal loads to provide an analog to those measured by an ATD.

In some previous studies investigating injury mechanics in the lower extremity, the technique used to measure loads internal to the tibia was to remove a section of the bone and install a load cell in its place (Takebe *et al.* 1984; Funk *et al.* 2004; McKay & Bir 2009). This allows the user to measure loads in line with the bone, in the same orientation as used by an ATD, but implantation increases the stiffness and changes the geometry of the specimen. Furthermore, artefactual fractures may be produced at the site of load cell implantation, which can call into question any injuries occurring near this area.

A number of groups have attempted to use strain data to estimate internal tibia loads as a way to avoid implanting a load cell (Funk & Crandall 2006; Untaroiu *et al.* 2007; Henderson *et al.* 2013). Strain can be measured non-invasively by applying gauges to the bone's outer surface at a region of interest. Using known geometric properties, it is then possible to model the bone as a long beam subjected to combined compression and bending. Gathered strain can be used to estimate the stress profile at a specific cross section, and the beam model allows for the calculation of applied loads based on this profile.

Specifically looking at the experiments conducted in this work, it would be highly impractical to implant a load cell into an isolated tibia as there would be very little natural tissue left. Additionally, while an external load cell was used to measure experimental forces and moments, the off-axis impact configuration used did not allow for direct measurement of loads internal to the specimen. Therefore, a strain-based method was

developed and tested to estimate internal bone loads during impact testing to provide an analog to loads measured by an ATD in the same configuration.

4.2 Methods

4.2.1 Specimen Preparation

Four specimens from two donors were selected to be used for strain-based load estimation. These two pairs were chosen at random from the six pairs that were subjected to impact testing as outlined in Chapter 3. All specimens were aligned within PVC pipe sections and potted in dental cement following the general protocol outlined previously.

In order to provide a useful analog to loads measured by an ATD, an attempt was made to place the gauges in a location that would be as similar as possible to the location of a load cell within commonly-used ATD legforms. Both the Hybrid III and MIL-LX legforms have load cells at the distal and proximal ends of their tibias. This unfortunately is a region of high curvature in the natural tibia, and the distal epiphysis was expected to be a site of fracture in impact testing. These two factors made both strain gauge application and load estimation difficult at this location, and so the gauges were applied to the distal diaphysis at a location of low curvature. Based on inspection of the specimens, this was 90 mm proximal to the plafond of the tibia as measured along the length of the bone.

Three uniaxial strain gauges (UFLA- 5-350-23-3L, Tokyo Sikki Kenkyujo, Japan) were applied to the bone, aligned with the bone's long axis, using the same gluing technique described previously (Section 3.2.1). Because the cross section of the bone is

roughly triangular at the chosen location, one gauge was placed in the approximate centre of each of the three faces: on the anterolateral (AL), anteromedial (AM), and posterior (P) surfaces.

4.2.2 CT Image Acquisition

Computed Tomography (CT) scans (120 kV, 11.88 mAs, slice thickness = 0.625 mm, in-plane resolution = 0.254 mm) were taken of all specimens (Figure 4-1) so that geometric properties could be quantified. The specimens were aligned on the scanner bed by the anatomical axes that were described previously.

4.2.3 Calibration Tests

External loads were applied to each specimen in a materials testing machine (5967, Instron, Norwood, MA, USA) to calibrate the relationship between strain to applied loads. Two configurations were used: cantilever bending (with load applied at the distal end perpendicular to the long axis) and axial compression (with load applied longitudinally via the distal articular surface) (Figure 4-2).

In the cantilever loading protocol, each specimen was supported at its potted (proximal) end and loaded by a platen at the distal end at 7 mm/min to a final load of 20 N. This was repeated in an AP orientation (posterior side up, in tension) and an ML orientation (medial side up, in tension). The point at which the bone contacted the platen was measured in order to quantify the moment arm and thus calculate the applied moment. In the axial loading protocol, each specimen was loaded at a rate of 2 mm/min to a final load of 200 N. In each test, the specimen was loaded cyclically four times so that relaxation and hysteresis effects could be observed. The peak strain in each gauge

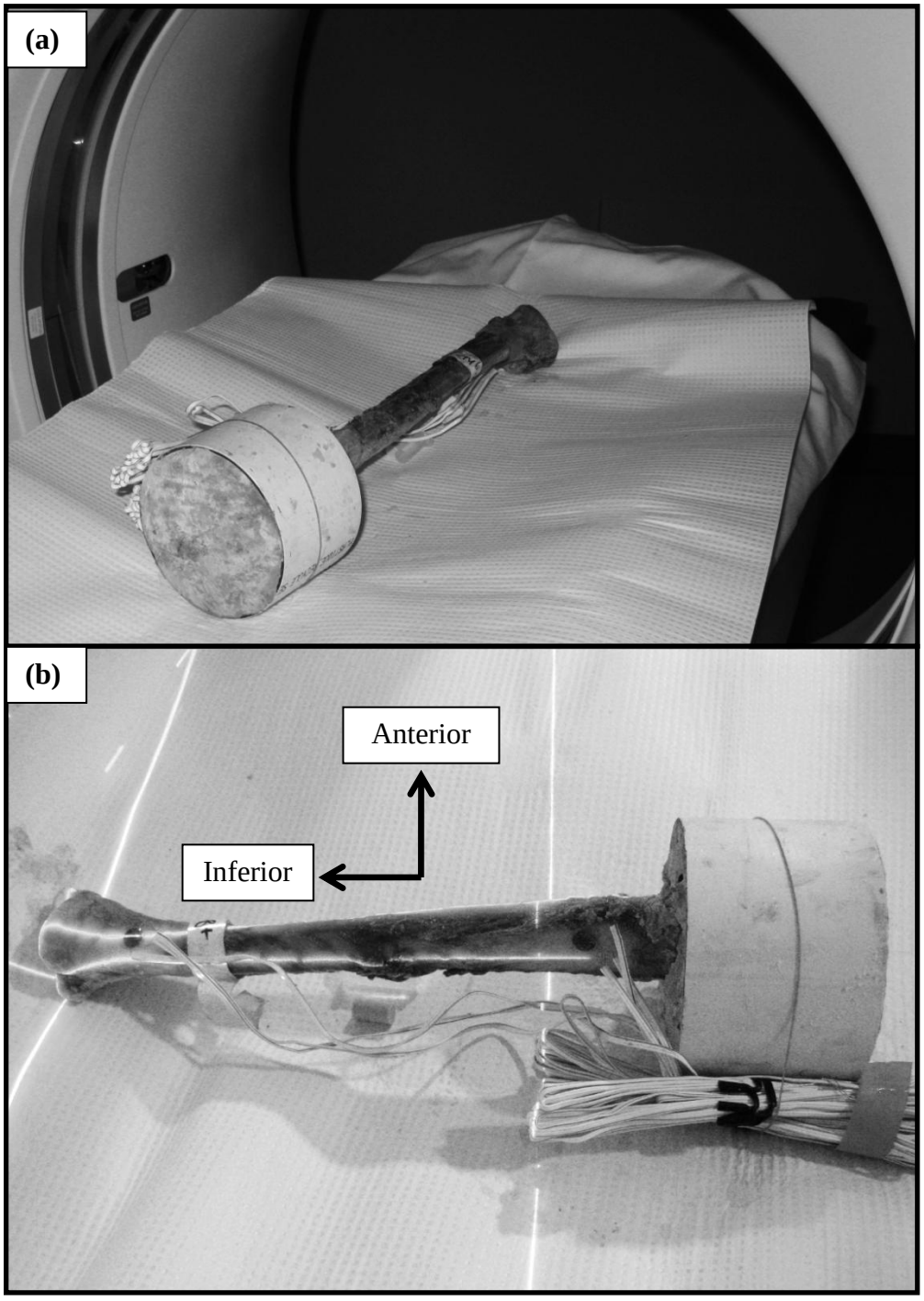

Figure 4-1: CT Scanning a Specimen
(a) A potted, strain-gauged specimen placed on the bed of the CT scanner for imaging. (b) The superior-inferior and anterior-posterior directions are shown explicitly, and were used to align the bone axes with the laser lines of the scanner.

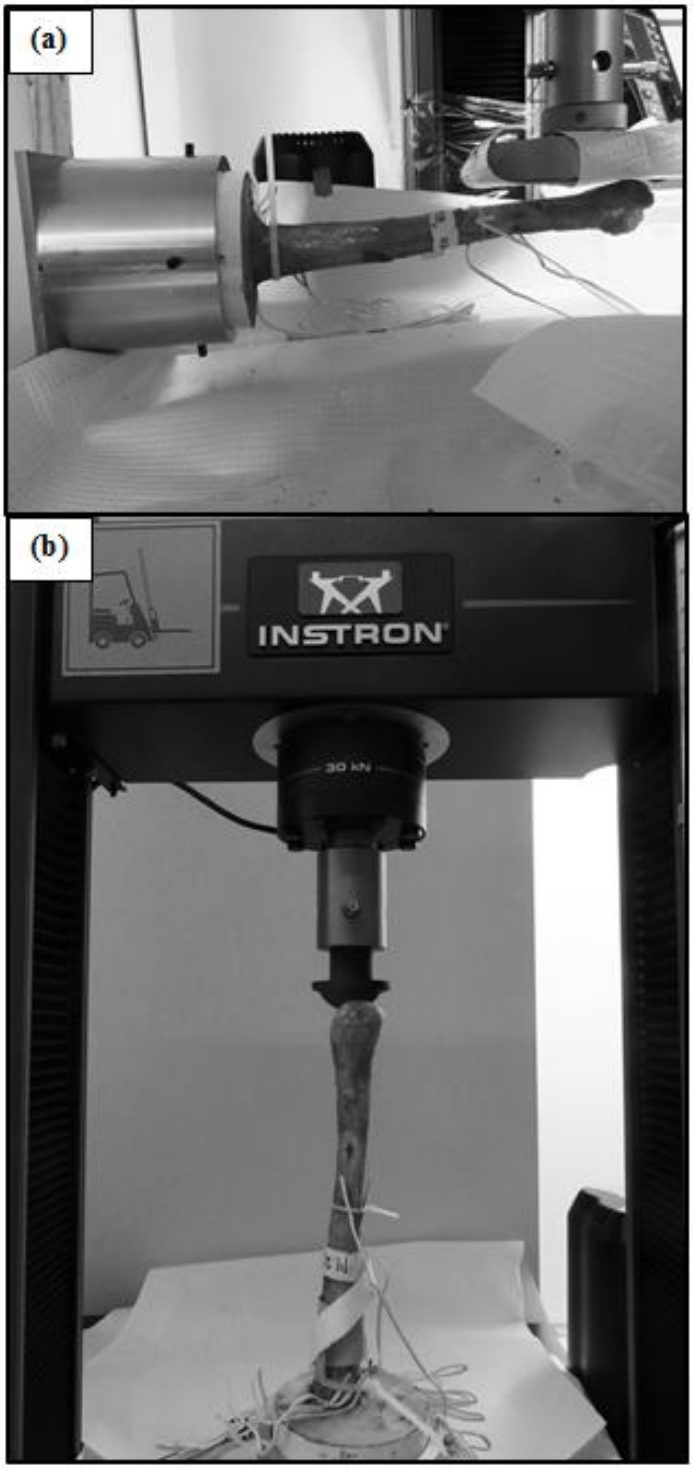

Figure 4-2: Configurations of Calibration Loading Protocols
(a) Cantilever loading configuration, and (b) axial compression loading configuration.

was then identified from the fourth loading cycle, as was the peak force measured by the Instron system.

For the compression test, load was transmitted through the distal articular surface and distributed by a rapid-prototyped talus, the geometry of which came from a male lower leg specimen. This talus was incorporated to reduce stress concentrations that could have arisen by loading the highly curved articular surface with a flat platen.

The peak loads for both tests were selected to be well below the threshold for injury so that repeated testing could be performed without compromising the specimen's mechanical properties before impact testing. Cantilever loads were kept under 84 N, which would produce a moment of 31.1 Nm at the proximal end of the longest specimen, which in turn is 10% of the quasistatic bending strength of the tibia as measured by Schreiber *et al.* (1998). Axial loads were kept under 270 N, corresponding to 5% of 5.4 kN, which is the load level corresponding to a 10% injury risk in an adult male (Yoganandan *et al.* 1996). Strain data were collected at 1000 Hz using a quarter-bridge completion compact data acquisition system (9236, National Instruments, Austin, TX, USA) and a custom-written LabVIEW (National Instruments, Austin, TX, USA) program. For every test, strain was collected for all time steps from all three gauges. At the same time, the materials testing machine recorded force and displacement data at every time step, with a frequency of 1000 Hz.

After calibration, all four specimens were subjected to impact tests as described in Chapter 3. Strain data were collected from these impact tests at 50 kHz, and impact

forces and moments were measured at the tibial plafond by an externally-mounted load cell in line with the direction of impact.

4.2.4 Load Estimation

4.2.4.1 Linear Combination Method

The first method used to predict loads from strain involved relating stress and strain to a linear combination of externally-applied moments and forces. Assuming that no torsion or shear would be induced during impact testing, any stress (σ) developed in the specimen at a given location *i* would be due only to a combination of bending and compressive stresses:

$$\sigma_i = \frac{M_{AP} * c_{i,AP}}{I_{AP}} + \frac{M_{ML} * c_{i,ML}}{I_{ML}} + \frac{F_{axial}}{A_{CS}} \qquad \textbf{(Equation 4-1)}$$

In this equation, M_{AP} and M_{ML} are moments about the AP and ML axes, respectively, F_{axial} is axial compressive force along the superior-inferior axis, $c_{i,AP}$ and $c_{i,ML}$ are the perpendicular distances from the point of interest to the two axes, I_{AP} and I_{ML} are area moments of inertia of the cross section of interest about the two axes, and A_{cs} is the area of the cross section of interest.

Assuming that this stress is developed under linear elastic conditions and that throughout the cross section there is a uniform elastic modulus E, it can be said that the strain at any given location (*e.g.* at the location of an applied strain gauge) is also related to these external loads:

$$\varepsilon_i = \left(\frac{1}{E}\right) * \left(\frac{M_{AP} * c_{i,AP}}{I_{AP}} + \frac{M_{ML} * c_{i,ML}}{I_{ML}} + \frac{F_{axial}}{A_{CS}}\right) \quad \textbf{Equation 4-2}$$

Assuming now that geometric and material properties are constant throughout testing in various configurations, Equation 4-2 can be reduced to a simple linear equation relating strain measured from a gauge to external loads:

$$\varepsilon_i = a_i * M_{AP} + b_i * M_{ML} + c_i * F_{axial} \quad \textbf{Equation 4-3}$$

In Equation 4-3, the coefficients a_i, b_i, and c_i are specific to each gauge, and are a function of the local geometric (c, I, and A) and material (E) properties. In order to calculate all three coefficients for the three applied gauges, at least nine measurements were required. With this in mind, each specimen was subjected to three bending tests (with load applied in the anterior-posterior (AP) direction, in the medial-lateral (ML) direction, and a combined test in which the specimen is loaded at a point 45° between the two anatomical axes) and one compression test.

In order to assess the efficacy of this method before applying it to the impact scenario, the coefficients a_i and b_i were calculated for each gauge based on AP and ML bending tests. The specimen was then rotated 45° and subjected to the third bending test and the previously-calculated coefficients were used to predict strain in this configuration (with the applied load decomposed along the two anatomical axes). These predicted strains were then compared with the actual strains measured in this test.

4.2.4.2 Extraction of Material and Geometric Properties

In order to perform a more sophisticated analysis, the CT images of each specimen were used to quantify geometric properties in ImageJ (version 1.49) open

source software (National Institutes of Health, Bethseda, MD, USA) using the BoneJ plugin (version 1.4.0). Key geometric data are listed in Appendix G.

The stack of images for each specimen was inspected for the location of the strain gauges, which showed up bright white in the CT scans. The first slice, starting from the distal end and moving proximally, that showed all three gauges was taken as the cross section of interest for each specimen.

The stack was also inspected for the orientation of the anatomical axes. Although care was taken to align the specimens in the CT scanner, they all had a tendency to roll out of the ideal alignment. By inspecting the scans of the plafond, the orientation of the ML axis within the frame of the scan was set based on the centre of the malleolus and the fibular notch. The AP axis was perpendicular to this axis in the plane of the slice (Figure 4-3). When setting the orientation of these axes in ImageJ, the central point lines up with the centre of the image frame, but the area moments of inertia are calculated about the geometric centroid of the material within a user-defined region of interest.

BoneJ was used to quantify the cross-sectional area (A_{CS}), the location of the geometric centroid (x_c, y_c), and the location of each gauge within the coordinates of the images (x_i,y_i) from the slice corresponding to the location of the gauges. This was all accomplished using the Slice Geometry function.

First, the neutral axis was approximated in each test by using Funk and Crandall's method (2006). Assuming a linear strain profile throughout the cross section, the peak strain from each gauge was used to interpolate along lines between pairs of gauges to locate three points of zero strain. These three points were connected with a straight line

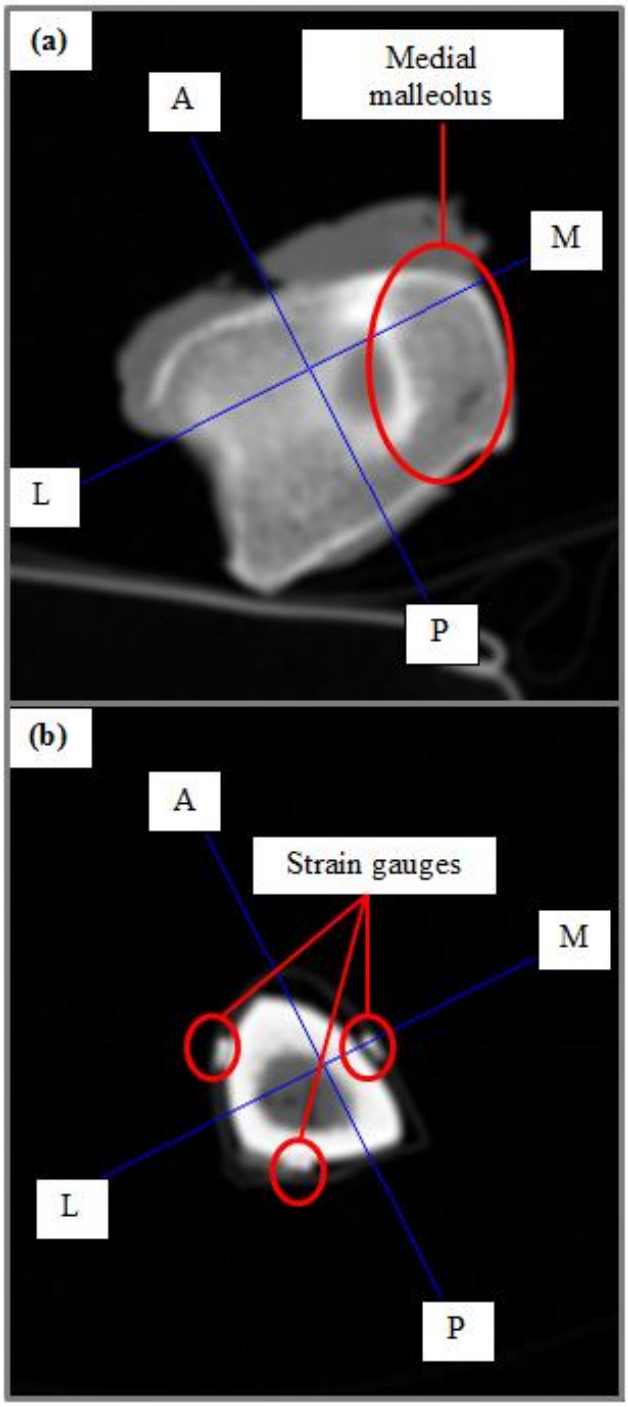

Figure 4-3: Slices of Interest Viewed in ImageJ
(a) Plafond and (b) gauge slices from one specimen. The AP and ML axes are identified on both slices, and the strain gauges are circled in red on the second slice.

that was taken as the neutral axis. The equation for this line (in the form $y=m_{NA}*x+b_{NA}$) was used to find the orientation of the neutral axis within the coordinates of the CT images (θ_{NA}) and the perpendicular distances from the gauges (c_i) and the geometric centroid (d_{NA}) to the neutral axis (Figure 4-4):

$$\theta_{NA} = tan^{-1}(m_{NA}) \quad \textbf{Equation 4-4}$$

$$c_i = \frac{m_{NA} * x_i - y_i + b_{NA}}{\sqrt{m_{NA}^2 + 1}} \quad \textbf{Equation 4-5}$$

$$d_{NA} = \frac{m_{NA} * x_c - y_c + b_{NA}}{\sqrt{m_{NA}^2 + 1}} \quad \textbf{Equation 4-6}$$

Using the Orientation function of ImageJ, the axes were shifted so that the AP axis was parallel to the neutral axis. The area moment of inertia (I'_{NA}) was calculated about this parallel axis which, by ImageJ's default, passed through the centroid. Parallel axis theorem was then used to calculate the area moment of inertia about the actual neutral axis:

$$I_{NA} = I'_{NA} + A_{CS} * d_{NA}^2 \quad \textbf{Equation 4-7}$$

To proceed from here, it was necessary to solve for a value of elastic modulus. This was taken from the AP and ML bending tests, in which the externally applied moment (M_{ext}) was already known based on test conditions. This magnitude of this moment applied about the neutral axis was calculated so that the area moment of inertia from Equation 4-7 could be used. This was done using the angle of the external load relative to ImageJ's coordinate system (θ_{ext}) (Figure 4-5, Equation 4-8).

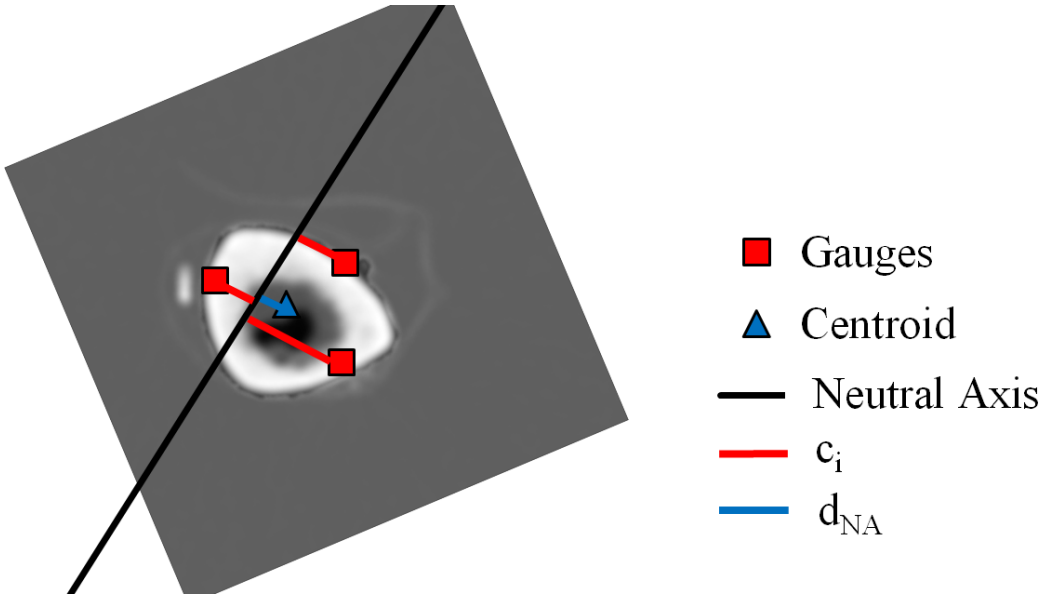

Figure 4-4: Gauge Locations, Geometric Centroid, and Neutral Axis Plotted For One Specimen

Values of c_i are graphically represented by red lines, while d_{NA} is represented in blue. Gauge locations were taken manually from ImageJ, centroid location was calculated by ImageJ, and the neutral axis and distances were calculated manually.

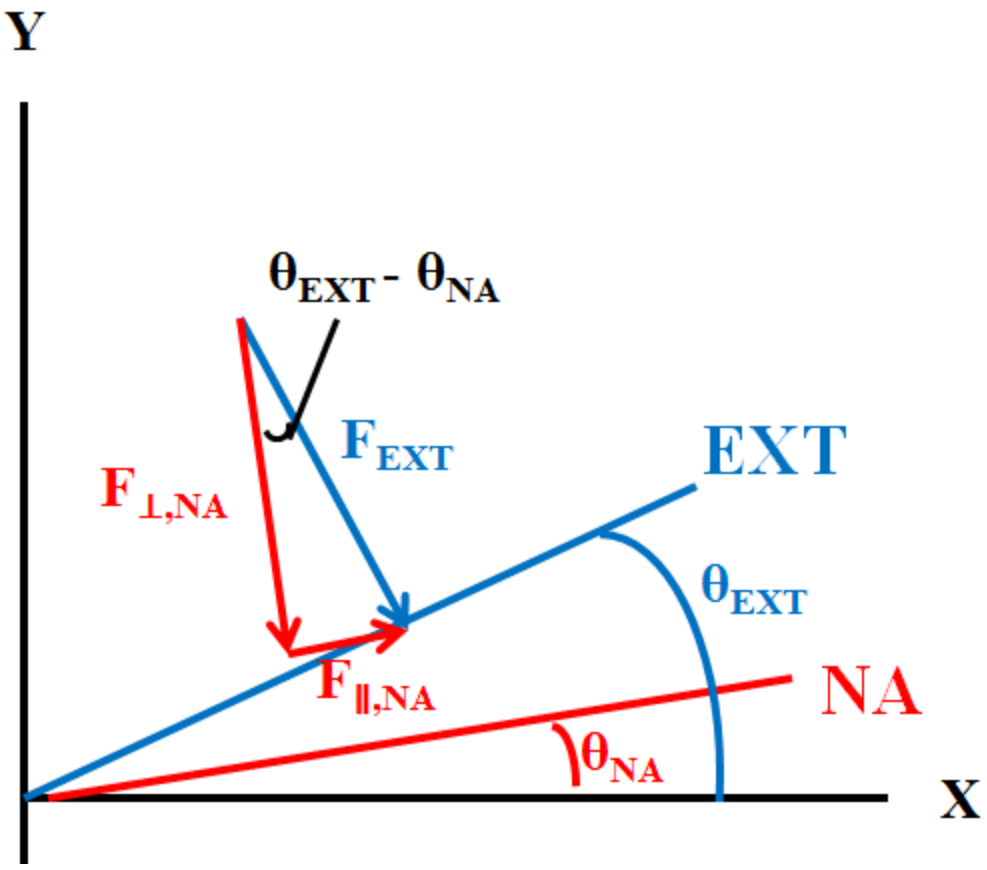

Figure 4-5: Visualisation of Various Coordinate Systems in Load Estimation
The figure shows how moments can be calculated in terms of different coordinate systems. The x and y in black refer to ImageJ's coordinate system, which was used to define the orientation of other axes as well as the location of the strain gauges and the geometric centroid. The blue axis (EXT) is the anatomical axis normal to the direction of external load application (*e.g.*, in the AP bend test, this would be the ML axis). The red axis (NA) shows the orientation of the neutral axis. M_{NA} (*i.e.*, a moment that can be induced by forces applied normal to the neutral axis) was calculated from the experimental tests. It is possible to determine the effective moment about the anatomical axis of interest (M_{ext}) using the angles of both the neutral axis and the anatomical axis relative to ImageJ's coordinate system.

$$M_{NA} = M_{ext} * \cos(\theta_{ext} - \theta_{NA}) \quad \textbf{Equation 4-8}$$

Bending stress was solved for using the moment about the neutral axis, the area moment of inertia, and the perpendicular distance between each gauge and the neutral axis. Based on the measured strain, the calculated bending stress could be used to calculate the elastic modulus.

$$\sigma_i = \frac{M_{NA} * c_i}{I_{NA}} \quad \textbf{Equation 4-9}$$

$$\varepsilon_i = \left(\frac{1}{E}\right) * \left(\frac{M_{NA} * c_i}{I_{NA}}\right) \quad \textbf{Equation 4-10}$$

$$E = \left(\frac{1}{\varepsilon_i}\right) * \left(\frac{M_{NA} * c_i}{I_{NA}}\right) \quad \textbf{Equation 4-11}$$

4.2.4.3 Load Estimation Based on Geometric and Material Properties

The elastic modulus and area moments of inertia were then used to calculate the loads M_{NA} and F_{axial} experienced at the cross section of interest in each specimen during the 45° bending calibration test as well as dynamic impact tests. This was done by assuming that the stress at each gauge was the sum of bending and axial stresses, similar to Equation 4-2:

$$\varepsilon_i = \left(\frac{1}{E}\right) * \left(\frac{M_{NA} * c_i}{I_{NA}} + \frac{F_{axial}}{A_{CS}}\right) \quad \textbf{Equation 4-12}$$

There are two unknowns in Equation 4-12: M_{NA} and F_{axial}. Therefore, strains from two gauges were required to solve for both unknowns. The two gauges with the greatest absolute values of strain were chosen to eliminate the risk of measuring noise instead of an actual signal. After M_{NA} had been found, it was possible to calculate the effective

moment about another axis of interest (such as M_{45}, the moment applied about an axis 45° between the AP and ML axes) using Equation 4-8.

This method was applied the same way to strains from both the 45° bending test and the impact tests. The estimation of load for the 45° bending test was compared with forces measured by the Instron multiplied by the predetermined moment arm. The predicted loads for the impact tests were compared with loads measured by the externally-mounted load cell in the test chamber: the resultant force (the vector summation of the forces measured in the x, y, and z directions) and the moments about the load cell's x axis, M_x (which corresponded to roughly the ML axis in the specimen, and therefore would correspond to anteroposterior bending).

4.2.4.4 Repeatability Test

In order to assess repeatability, strain data were gathered from five repetitions of the quasistatic AP bending test. Between repetitions, the specimen was removed from the test jig, the materials testing machine was returned to the home position, and then the specimen was set up again from the beginning of the test protocol. The peak strain and peak applied moment were then taken from each test to calculate the coefficient b_i in order to assess the repeatability of the calibration tests, the identification of peak strain, and the calculation of the peak bending moment.

Results

4.2.5 Linear Combination Method

The predicted values of strain based on the coefficients a_i and b_i for each gauge are compared to the actual measured values in the 45° cantilever bending test in Figure 4-6. The relative error ranged from 0-93% across all gauges, with the AL gauge giving the best agreement when inspected individually: this gauge only had relative errors ranging from 0-4%. Due to the poor overall agreement between the predicted and measured strains, the linear combination method of analysis was not extended to the results of compression testing, or those of impact testing.

4.2.6 Load Estimation Based on Geometric Properties

The neutral axes were calculated and plotted for the AP bending, ML bending, and compression calibration tests as well as for the impact test leading to fracture and the non-injurious impact test preceding the test leading to fracture (denoted as 'pre-fracture') for all four of the specimens inspected. The value of peak strain from each gauge, taken as the greatest absolute value achieved during a given test, was used to determine the orientation of the neutral axis (Figure 4-7).

The bending calibration tests consistently produced neutral axes that passed either directly through or close to the centroid of the cross section of interest. In each case, the distance from the neutral axis to the centroid was calculated and the plots (Figure 4-8, Figure 4-9, Figure 4-10, Figure 4-11) were inspected visually, but no pattern could be

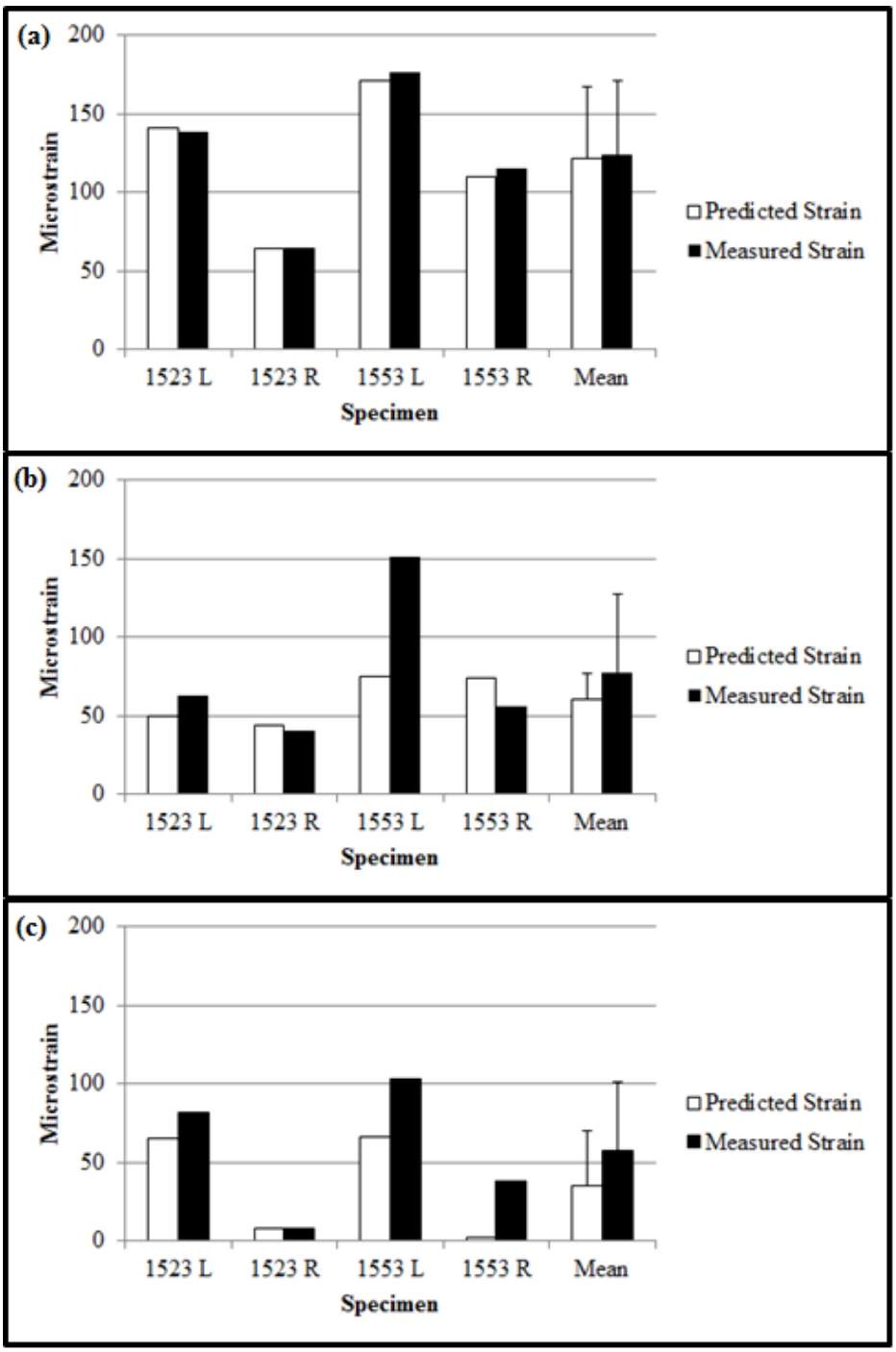

Figure 4-6: Predicted vs Measured Strain in 45° Bend Test
(a) Anterolateral gauge, (b) anteromedial gauge, (c) posterior gauge

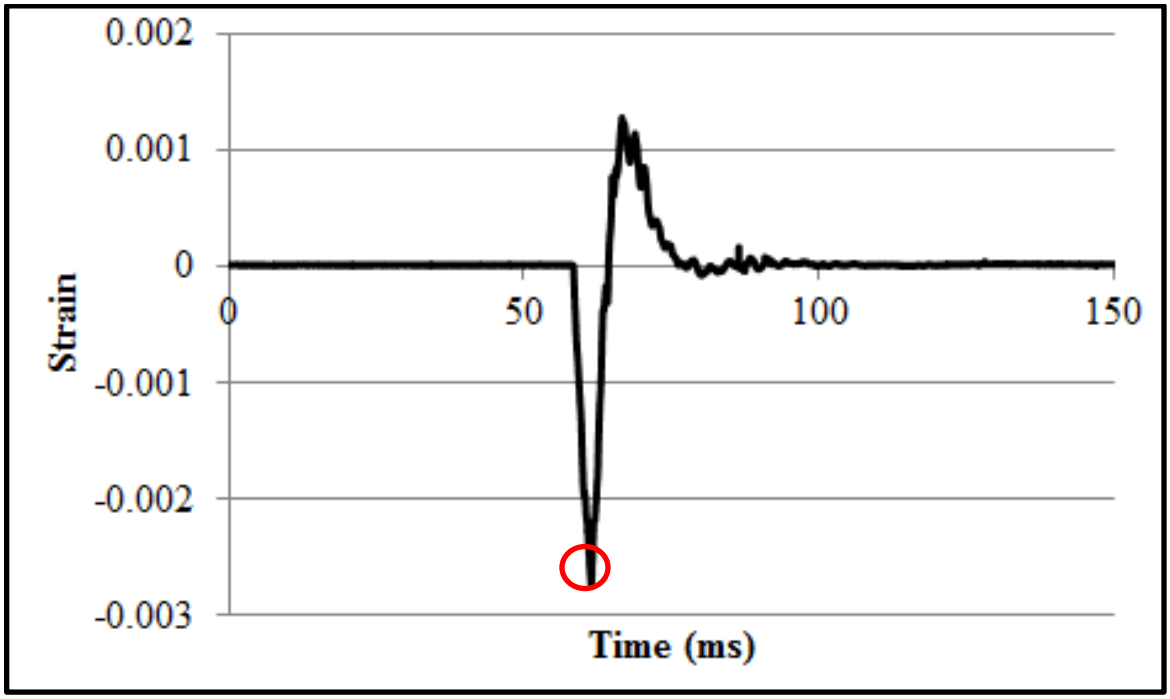

Figure 4-7: Representative Strain-Time Plot for Impact Test
The peak value taken for neutral axis calculation is circled in red. These data were taken from the test resulting in fracture for specimen 1523L.

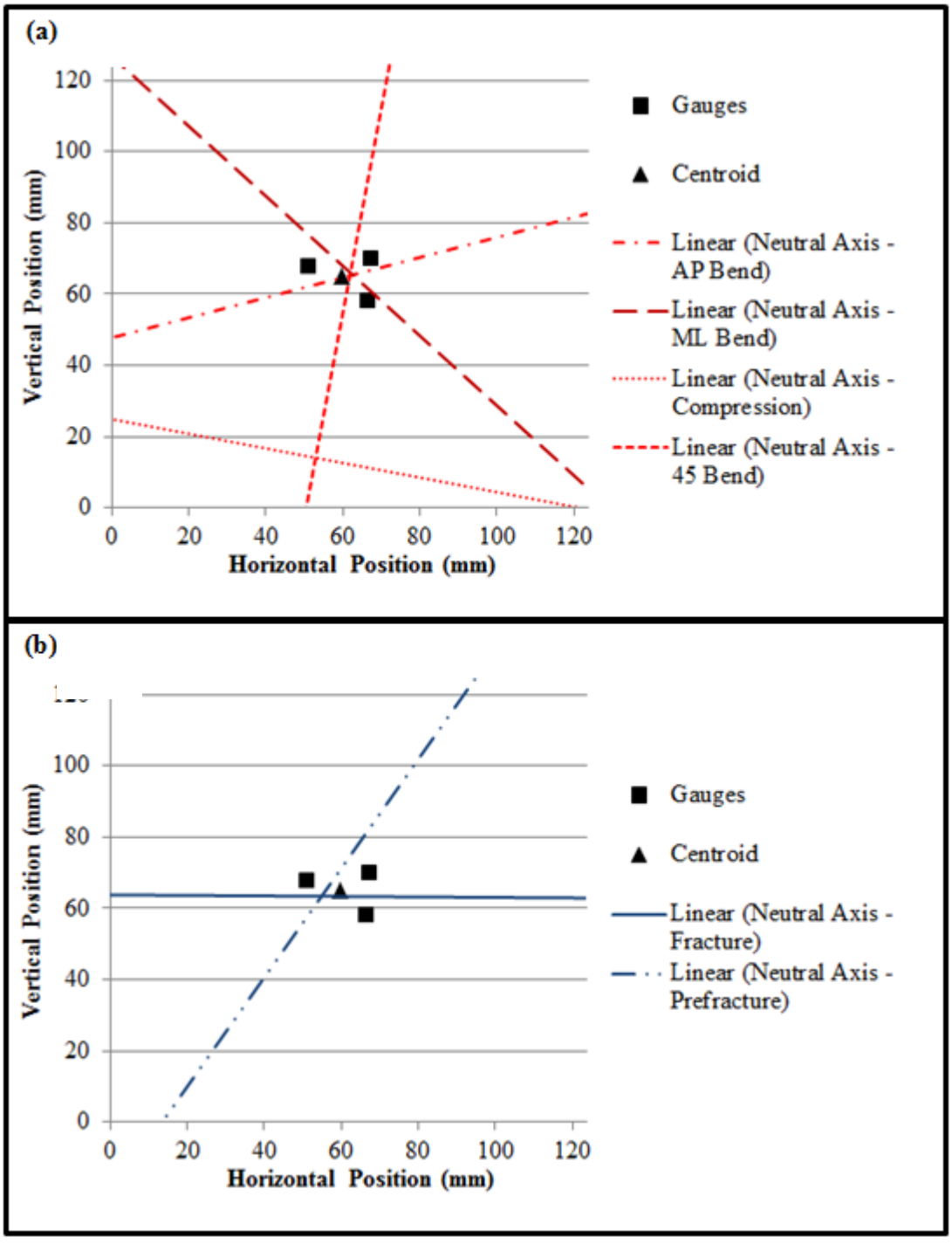

Figure 4-8: Neutral Axes Calculated for Various Loading Configurations on Specimen 1523L, Tested at 30°.

Neutral axes for (a) calibration tests, including bending and compression, and (b) impact tests.

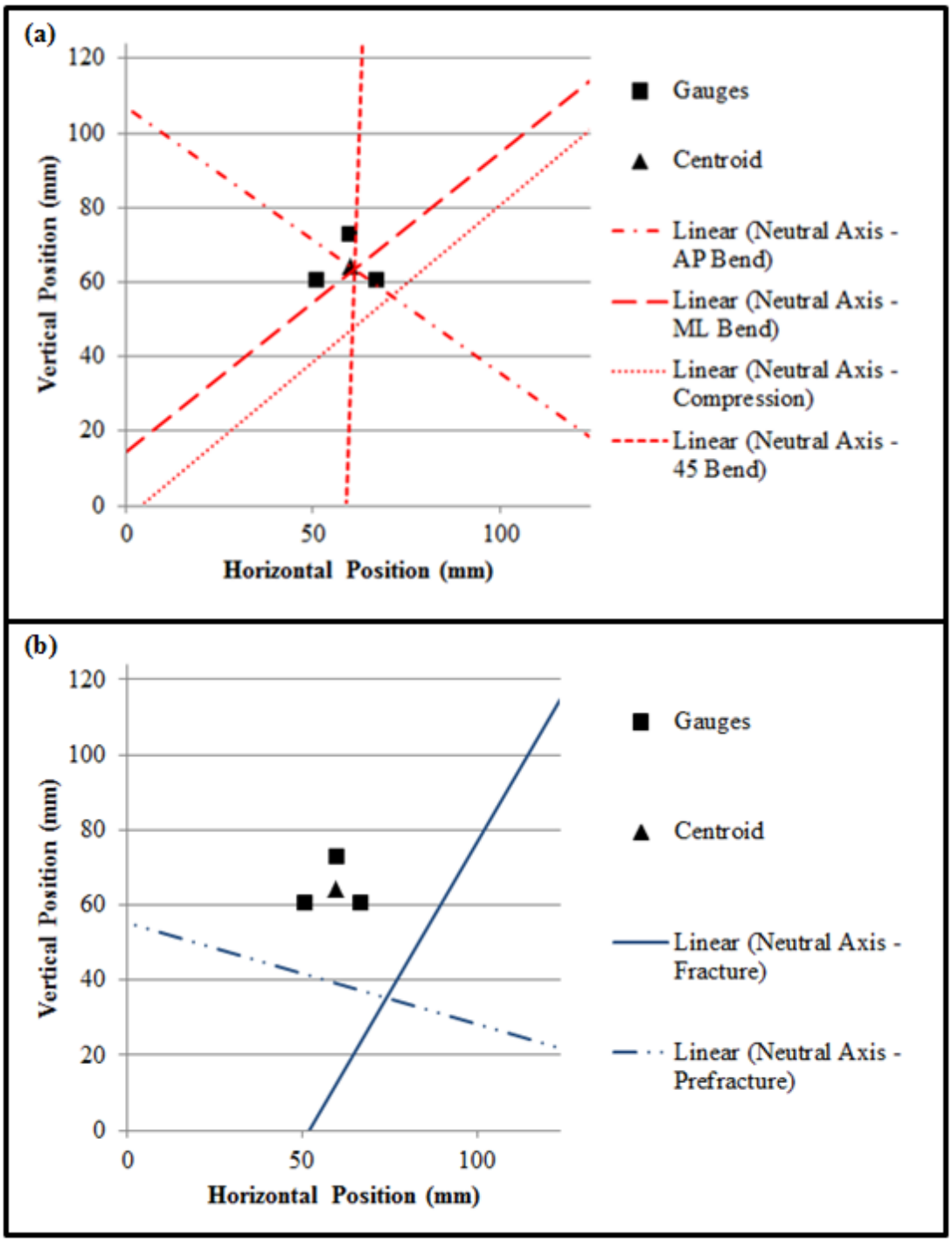

Figure 4-9: Neutral Axes Calculated For Various Loading Configurations on Specimen 1523R, Tested at 15°.

Neutral axes for (a) calibration tests, including bending and compression, and (b) impact tests are shown.

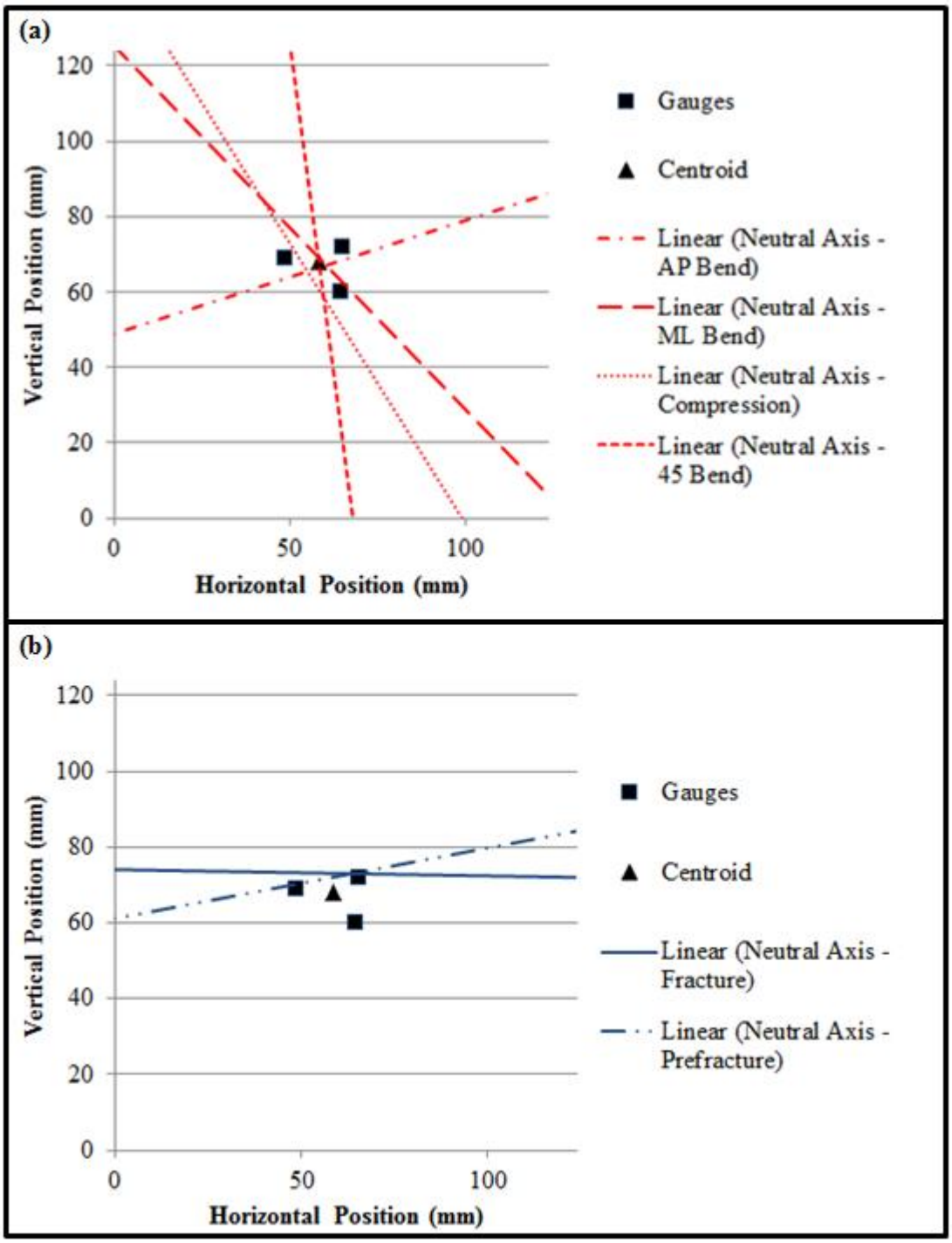

Figure 4-10: Neutral Axes Calculated For Various Loading Configurations on Specimen 1553L, Tested at 30°

Neutral axes for (a) calibration tests, including bending and compression, and (b) impact tests are shown.

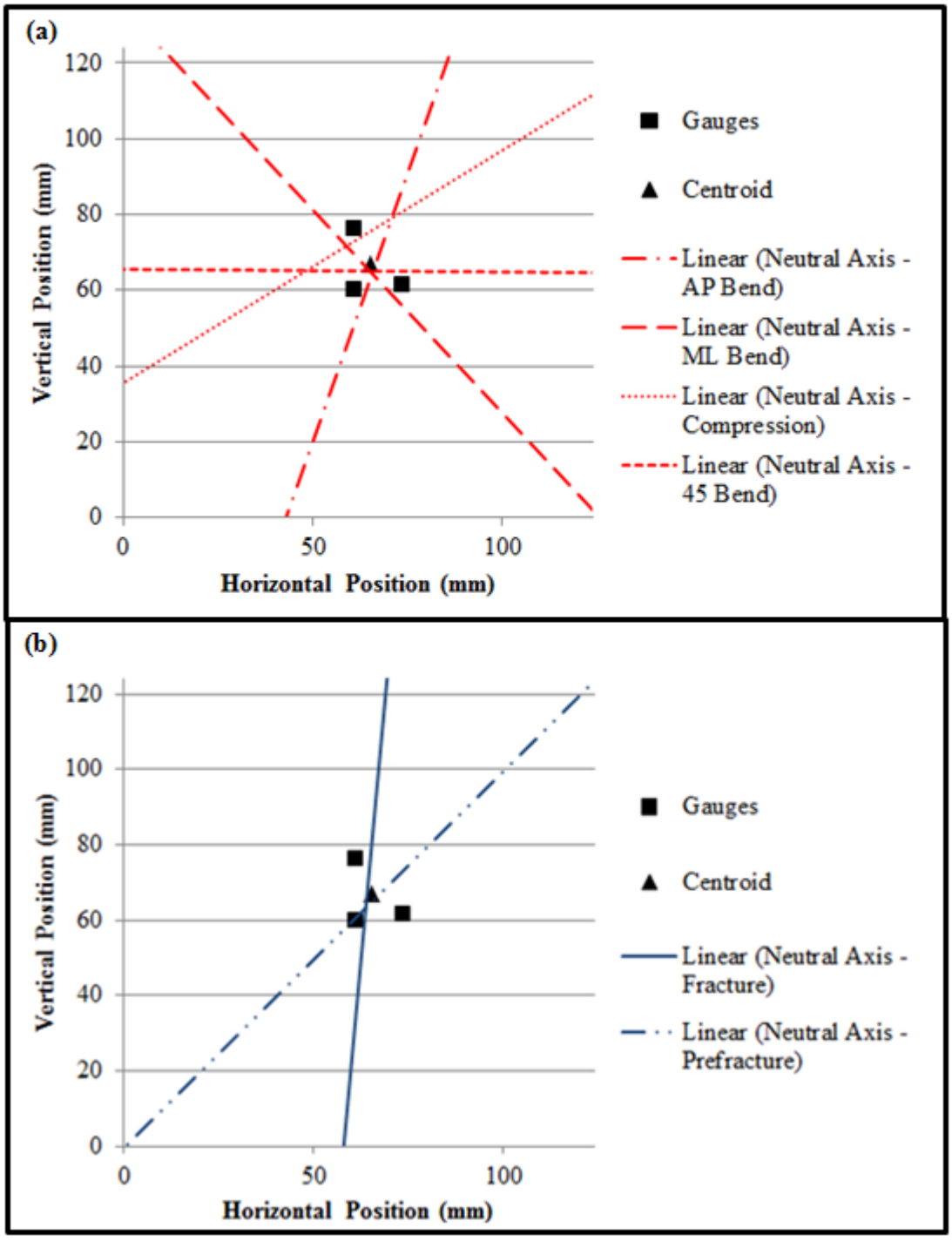

Figure 4-11: Neutral Axes Calculated For Various Loading Configurations on Specimen 1553R, Tested at 15°

Neutral axes for (a) calibration tests, including bending and compression, and (b) impact tests are shown.

discerned in the placement and/or orientation of the neutral axes in the compression or impact tests.

Elastic moduli were calculated based on the results of the AP and ML bending calibration tests (Table 4-1). Based on the AP tests, the mean (standard deviation) elastic modulus was 12.8 (2.0) GPa and based on the ML tests, the mean was 13.6 (3.5) GPa. Based on a paired t-test, these values were not significantly different (p=0.71). The values calculated from the AP bending tests were selected for use in the calculation of loads in impact testing due to the fact that the non-standard postures tested were assumed to produce more bending about the ML axis than the AP axis.

The resultant bending moment and resultant force were estimated for each specimen's 45° bending calibration test (Table 4-2) as well as its impact test resulting in fracture (Table 4-3) and its pre-fracture test (**Table 4-4**Table 4-4). For the 45° bending test, relative error ranged from 25-90% in the estimated bending moment. For the impact test, the relative error was very large, with estimated forces lower by many orders of magnitude, and with bending moments also underestimated by approximately an order of magnitude.

3.1.1 Repeatability Test Results

The coefficient $b_i = M_{AP}/\varepsilon_i$ was calculated for each gauge and for each of the five repetitions of the AP bending protocol on specimen 1523R (Table 4-5. As with the results of the linear combination method, the AL gauge gave the most consistent results.

Table 4-1: Calculated Values of Elastic Modulus from Calibration Bending Tests
Results of elastic modulus calculation for each specimen's quasistatic AP and ML bending tests.

Specimen	Elastic Modulus from AP Bending Test (GPa)	Elastic Modulus from ML Bending Test (GPa)
1523L	12.0	10.5
1523R	14.6	17.2
1553L	10.3	16.1
1553R	14.2	10.7
Mean (SD)	**12.8 (2.0)**	**13.6 (3.5)**

Table 4-2: Comparison of Estimated and Externally-Measured Loads in 45° Bending Test
Results of load estimation compared with values taken from the external load cell for the quasistatic 45° bending test on each specimen.

Specimen	Estimated Axial Force (N)	Estimated M_{45} Bending Moment (Nm)	Externally Measured M_{45} Bending Moment (Nm)	Relative Error in Moment Estimation
1523L	$1.2*10^{-2}$	1.2	1.8	36%
1523R	$1.2*10^{-2}$	0.7	1.3	32%
1553L	$1.0*10^{-3}$	0.9	2.5	90%
1553R	$3.1*10^{-2}$	1.2	1.6	25%

Table 4-3: Comparison of Estimated and Externally-Measured Loads at Fracture

Results of load estimation compared with values taken from the external load cell for injurious impact tests on each specimen.

Specimen (Leg Angle)	**Estimated Axial Force (N)**	**Externally Measured Resultant Force (N)**	**Estimated Bending Moment About M-L Axis (Nm)**	**Externally Measured Bending Moment About X-axis (Nm)**
1523L (30°)	$1.7*10^{-3}$	6403	38.4	199
1523R (15°)	$2.3*10^{-3}$	4838	28.5	132
1553L (30°)	0.51	4954	38.3	178
1553R (15°)	1.0	5422	47.7	129

Table 4-4: Comparison of Estimated and Externally-Measured Loads Preceding Fracture

Results of load estimation compared with values taken from the external load cell for the impact test preceding fracture for each specimen.

Specimen (Leg Angle)	**Estimated Axial Force (N)**	**Externally Measured Resultant Force (N)**	**Estimated Bending Moment About M-L Axis (Nm)**	**Externally Measured Bending Moment About X-axis (Nm)**
1523L (30°)	$3.9*10^{-4}$	3526	19.9	92
1523R (15°)	$6.4*10^{-4}$	8023	341.8	226
1553L (30°)	0.42	3122	31.0	102
1553R (15°)	0.30	3527	57.8	132

Table 4-5: Results of Repeatability Testing On Coefficient Calculation

Calibration coefficients computed for specimen 1523R in the AP bending configuration over five trials.

	Coefficient for AL Gauge	**Coefficient for AM Gauge**	**Coefficient for P Gauge**
Test 1	$-4.62*10^{-5}$	$8.10*10^{-6}$	$3.78*10^{-5}$
Test 2	$-4.96*10^{-5}$	$6.46*10^{-6}$	$2.76*10^{-5}$
Test 3	$-4.66*10^{-5}$	$6.64*10^{-6}$	$2.64*10^{-5}$
Test 4	$-4.30*10^{-5}$	$6.29*10^{-6}$	$2.00*10^{-5}$
Test 5	$-4.23*10^{-5}$	$7.73*10^{-6}$	$1.77*10^{-5}$
Mean (Standard Deviation)	$-4.56*10^{-5}$ ($2.96*10^{-6}$)	$7.04*10^{-6}$ ($8.14*10^{-7}$)	$2.59*10^{-5}$ ($7.86*10^{-6}$)
Standard Deviation as % of Mean	6.5%	11.6%	30.4%

4.3 Discussion

The purpose of this analysis was to assess the feasibility of estimating internal loads using strain data gathered from the outer surface of a tibia by modelling the bone as a simple beam under bending and compression. These internal loads are analogous to those measured by ATD legforms in crash tests, which come with in-line load cells to measure force parallel to the long axis. However, in cadaveric impact tests, it is extremely difficult to measure these internal loads, which makes it difficult to apply load limits defined for ATD testing to these experiments.

If a load cell is used in cadaveric testing, it must either be mounted external to the specimen (which makes alignment challenging in the case of axial configurations, due to the curvature and irregular cross-sectional geometry of long bones, and which requires the computation of resultant loads in the case of off-axis loading) or implanted into the bone (thereby compromising material and geometric properties that may affect injury tolerance and load distribution). Strain gauges, however, are small and non-invasive, and can be applied to the outside of a bone at any location that is relatively flat (or that can be sanded flat). They therefore present an opportunity to develop a method to relate strain gauge signals to forces and moments.

Two approaches to estimating load based on strain were outlined in this chapter. The first (and the more simple) approach assumed that strain from any of the three gauges would be a linear combination of forces and moments applied externally to the bone, and that the coefficients of this linear combination would remain constant among loading configurations. However, it was shown that this was not a feasible method of load

estimation, due to the fact that when a strain gauge was too close to the neutral axis, its strain measurement was indistinguishable from noise. The best way to avoid this would be to calculate coefficients based off of compression testing, which was more likely to produce neutral axes that fell outside of the cross section of interest compared with bending tests. Theoretically, this would reduce the risk of intersection with the location of any gauges. However, this would require a thorough investigation of bone curvature to be able to determine the moments induced at the distal diaphysis by compression. This would also be very challenging, and therefore this method is not recommended for further use.

The other approach relied on geometric data acquired from CT scans and a more rigorous application of mechanical beam theory. The neutral axis was estimated based on an assumption of a linear strain profile for a variety of loading configurations on each specimen, which itself relied on an assumption of uniform material properties through the cross section. Additionally, the calculation of the neutral axis was very sensitive to the measurement of peak strain and the identification of the gauges' locations within the CT scan coordinates, all of which are subject to human error. It is therefore not surprising that a pattern did not emerge from such a small sample.

If these factors contributed to error in the calculation of the neutral axis, that error would have been carried forward into the following calculations of stress and load. However, it should be noted that the bending tests consistently resulted in a neutral axis that passed very close to the centroid of the cross section, as is expected from pure bending in a simple beam. In compression and under dynamic off-axis loading, the

neutral axis was expected to be shifted away from the centroid, but this was not found to be consistently true, and no pattern could be discerned in the direction or magnitude of the axis's displacement. It is possible that the axial components of load induced bending moments (due to the bone's curvature) at the region of interest that dominated over compression in these scenarios. It should be noted that a previous attempt to estimate applied loads based on strain (Funk & Crandall 2006) also found that induced moments dominated over compression in supposedly axial loading configurations. It had been hoped that the method described here would perform better than this previous attempt due to the use of isolated tibias and the movement of the region of interest from midshaft to the distal diaphysis. It would seem, however, that these issues were not avoided.

Elastic moduli were calculated from the bending tests, with the AP tests yielding an average modulus of 12.8 GPa, while the ML tests yielded an average modulus of 13.6 GPa. Experimentally-derived values of the elastic modulus of cortical bone can vary depending on the loading method used and the type of sample analysed (Rho *et al.* 1998), although one study looking at the macroscopic modulus of cortical bone in tension and compression found values ranging from 11.4 to 19.7 GPa (Reilly *et al.* 1974). The values obtained in this work mostly fall in this range, with a few values just below the lower bound. This may be attributed to the use of older female specimens in this work, which may be expected to be smaller and to have less bone mass than male specimens, contributing to lower whole bone stiffness. It was therefore thought that this method was acceptable for determining this property.

The loads estimated based on the geometric properties from CT data were very different from the loads measured by the externally-mounted load cell used in impact testing. It was not expected that these values would be equal, as the load cell was not in line with the specimen due to the dynamic off-axis loading simulated, and in some cases contact was not maintained between the specimen's distal articular surface and the load cell due to geometric variations. It was also found in the analysis of impact tests that the moments measured by the load cell were not significantly different when comparing between the two non-standard postures used in this study, which was contrary to expectations. Specimens held at a higher angle relative to the direction of impact broke at lower loads than those held closer to an axial posture. This was assumed to be due to a higher component of bending in the specimen held at the higher angle. Because of this, the ability of the externally-mounted load cell to measure bending moments experienced in the bone's diaphysis was called into question. Therefore, it was not expected that the estimated loads would line up with those from the load cell.

What was surprising, however, was that the estimated moments and forces were so low compared to those measured by the load cell. Based on the performance of the method in estimating loads for the 45° bend test (25-90% relative error), it was not expected that the estimated impact loads would be smaller than those measured by the load cell by orders of magnitude. This may have been due to an underestimation of the elastic modulus, which tends to be higher in bone at higher strain rates (Currey 1975). Additionally, the calculations of small magnitudes of axial force make sense given that the estimated neutral axes passed fairly close to the centroid, which would suggest that

bending was the dominant loading mode. Once again, however, the approximation of the neutral axis was subject to several sources of error and may have ultimately led to an underestimation of axial force.

Ultimately, it is clear that this method of non-invasively estimating internal bone loads needs to be refined. The placement and alignment of strain gauges, which are both subject to human error and which can be affected by inter-specimen variability, have a strong effect on the values of peak strain measured. Additionally, the measurements taken by ImageJ are affected by the accuracy of alignment of the specimen within the CT scanner, and the measurement of external bending moments are affected by the proper measurement of moment arms and alignment of the specimen within the test apparatus. Finally, the calculation of loads from strain data relies on the assumption that the bone behaves as a linear elastic material with uniform properties along its length and that the mechanical properties will be the same under quasistatic, non-injurious loading (as was used in the calibration process) and under dynamic loading resulting in fracture (as was used in the impact test protocol). This goes against the previously-established finding that bone tends to be stiffer at higher strain rates (Currey 1975). A more precise protocol for gauge application, a more sophisticated test set up for calibration, and a more complex material model for bone may be used to refine this process in the future. In addition, increasing the sample size in the future may also allow for statistical analysis that was not possible in this work.

Previous attempts to correlate strain with loading in long bones have been reported in the literature, indicating that there is a need for a method to non-invasively estimate

internal bone loads. Implanted load cells can compromise experimental results, and externally-mounted load cells may not accurately capture internal loading. This was the first attempt to calculate loads using geometric data acquired from CT scans and ImageJ open source software, and to apply this method to the evaluation of dynamic off-axis loading. It was shown that the elastic modulus of cortical bone may be estimated reasonably well using strain and force data gathered from a quasistatic bending test in conjunction from CT images. The results of the load estimation method performed poorly under dynamic impact conditions, but this work may serve as a starting point for refining the process in the future.

4.4 References

Currey, J. D. 1975. “The Effects of Strain Rate, Reconstruction and Mineral Content on Some Mechanical Properties of Bovine Bone.” *Journal of Biomechanics* 8 (1).

Doube M, Kłosowski MM, Arganda-Carreras I, Cordeliéres F, Dougherty RP, Jackson J, Schmid B, Hutchinson JR, Shefelbine SJ. 2010. "BoneJ: free and extensible bone image analysis in ImageJ." *Bone* 47: 1076-1079.

Funk, James R., and Jeff R. Crandall. 2006. “Calculation of Tibial Loading Using Strain Gauges.” *Biomedical Sciences Instrumentation* 42 (2): 160–65.

Funk, James R, Rodney W Rudd, Jason R Kerrigan, and Jeff R Crandall. 2004. “The Effect of Tibial Curvature and Fibular Loading on the Tibia Index.” *Traffic Injury Prevention* 5 (2): 164–72.

Henderson, Kyvory A, Ann M Bailey, John J Christopher, Fred Brozoski, and Robert S Salzar. 2013. “Biomechanical Response of the Lower Leg under High Rate Loading.” *2013 IRCOBI Conference Proceedings*, 145–57.

McKay, Brian J, and Cynthia A Bir. 2009. “Lower Extremity Injury Criteria for Evaluating Military Vehicle Occupant Injury in Underbelly Blast Events.” *Stapp Car Crash Journal* 53: 229–49.

Rasband, W.S., ImageJ, U. S. National Institutes of Health, Bethesda, Maryland, USA, http://imagej.nih.gov/ij/, 1997-2016.

Reilly, Donald T., Albert H. Burstein, and Victor H. Frankel. 1974. “The Elastic Modulus for Bone.” *Journal of Biomechanics* 7 (3).

Rho, Jae Young, Liisa Kuhn-Spearing, and Peter Zioupos. 1998. “Mechanical Properties and the Hierarchical Structure of Bone.” *Medical Engineering and Physics* 20 (2): 92–102.

Schreiber, P.; Crandall, J.; Hurwitz, S.; Nusholtz, G.S. 1998. “Static and Dynamic Bending Strength of the Leg.” *International Journal of Crashworthiness* 3 (3): 2950398.

Takebe, K, A Nakagawa, H Minami, H Kanazawa, and K Hirohata. 1984. “Role of the Fibula in Weight-Bearing.” *Clinical Orthopaedics and Related Research* 184: 289–92.

Untaroiu, Costin, Jason Kerrigan, Check Kam, Jeff Crandall, Kunio Yamazaki, Keisuke Fukuyama, Koichi Kamiji, Tsuyoshi Yasuki, and James Funk. 2007. “Correlation of Strain and Loads Measured in the Long Bones with Observed Kinematics of the

Lower Limb during Vehicle-Pedestrian Impacts." *Stapp Car Crash Journal* 51 (October): 433–66.

Yoganandan, Narayan, Frank a Pintar, Melbourne Boynton, Paul Begeman, Priya Prasad, Shashi M Kuppa, Richard M Morgan, and Rolf H Eppinger. 1996. "Dynamic Axial Tolerance of the Human Foot-Ankle Complex." *Society of Automotive Engineers, Inc.* 962426: 207–18.

Chapter 5: General Discussion and Conclusions

5.1 Summary

The bulk of cadaveric experimental work on the tibia's injury tolerance under dynamic loading has been conducted with the specimen in an idealised neutral posture. In this posture, load is directed along the long axis of the leg, with a 90° angle between the shank and foot. However, this does not encompass the range of postures a vehicle occupant may assume during a traumatic event, and the effect of non-standard postures on injury tolerance has not been well quantified. These non-standard postures may induce higher proportions of bending relative to axial compressive loads, which, according to a widely cited injury criterion for the tibia (Tibia Index), should increase the risk of fracture. Commonly-used lower leg surrogates such as the Hybrid III and MIL-LX legforms (Humanetics Innovative Solutions, Plymouth, MI, USA) also do not have established limits specifically to account for testing in non-standard postures.

The overall purpose of this work was to study and quantify the effect of non-standard postures on the tibia's injury tolerance under dynamic loading typical of a frontal collision, and to develop and evaluate a method for non-invasively estimating loads internal to the tibia during impact tests.

The first phase of this work was to design and install a system of pneumatic components to generate impacts representative of a frontal automotive collision (*i.e.*, Objective #1a, Chapter 2). These components formed a subsystem of a larger test apparatus, the design and construction of which began before the start of this work. The pneumatic system was installed and calibrated to propel projectiles of varying mass (as

low as 2.8 kg and as high as 28 kg) to achieve a range of impact velocities, including 6 m/s, which was targeted as representative of a frontal collision.

The apparatus was then used to perform impact testing on six pairs of isolated cadaveric tibias in two different postures: 15° relative to the direction of impact, and 30° relative to the direction of impact (*i.e.*, Objective #1b, Chapter 3). It was found that the specimens held further from the direction of impact fractured at significantly lower forces than the specimens held closer to the direction of impact (*i.e.*, Hypothesis #1 accepted). The Hybrid III and MIL-LX legforms were also subjected to impact testing (*i.e.*, Objective #2, Chapter 3), and it was found that the MIL-LX was projected to register a force close to its existing load limit under injurious conditions, even in non-standard postures. The Hybrid III's response was more strongly affected by posture and did not perform well based on its current load limit (*i.e.*, Hypothesis #2 accepted).

Prior to impact testing, four specimens (two pairs) were instrumented with three uniaxial strain gauges each at the distal diaphysis. These specimens were subjected to calibration tests in a materials testing machine and Computed Tomography (CT) scans were used to extract geometric properties. These data, combined with strain gathered during the impact tests, were used to estimate internal bone loads (*i.e.*, Objective #3 Chapter 4). Due to challenges with alignment of the gauges and the specimens, as well as assumptions of the beam model used to estimate internal loads, the calculated loads were not in good agreement with those measured by an externally mounted load cell. In both cases of high and low measured strains, the estimated axial force was orders of magnitude lower than what was expected based on readings from the load cell. Estimated bending

moments were lower than expected as well, although the differences were not as great as for axial force (*i.e.*, Hypothesis #4 rejected).

5.2 Strengths and Limitations

The specific strengths and limitations of each phase of the study were discussed in their respective chapters. However, there are general strengths and limitations applicable to the whole of this work.

The use of paired specimens was considered a strength as it allowed a direct comparison of the effects of the two non-standard postures while controlling for variation among the individual donors. The use of isolated specimens also allowed for a clear understanding of load transmission, which would not be present in a study using an intact lower leg (in which there are more degrees of freedom due to the presence of foot and ankle joints, and in which it is difficult to quantify load dissipation by soft tissues). Testing on an isolated long bone also makes the results of this work potentially applicable to other long bones, such as those of the upper extremity. The injury risk curves generated from the impact study showed that posture does have an effect on the tibia's injury tolerance, indicating that this is a factor that should be considered in future injury studies. The Tibia Index, which has previously been based on the results of quasistatic testing, was also evaluated and reformulated under dynamic conditions. There was also a direct comparison between cadaveric and ATD testing. The design of the test apparatus also allowed the user to employ a wide range of projectile masses while keeping impact velocity at a consistent level representative of a frontal collision. Finally, while the tested

methods for estimating internal bone loads from surface strain data did not yield the expected results, suggestions have been made to improve the estimation in the future.

A limitation of this work is that delivering impact to an isolated bone along a linear path does not, of course, accurately recreate the conditions of a frontal collision, in which the structural components of the vehicle would play a role in loading the lower leg, and in which the tibia would not be loaded in isolation. However, efforts were made to represent collision loading in terms of impact velocity and duration, and the goal of this work is to ultimately make recommendations for protecting against tibia fractures in non-standard postures. Therefore, characterising the mechanical behaviour of the tibia in this simplified impact scenario should give insight into the mechanics of injury in a more complex loading event. Additionally, injury assessments using ATD legforms are based only on tibia forces, and therefore an inspection of the isolated tibia was warranted. Another limitation was the use of repeated impact testing, although steps were taken to minimise the number of strikes to reduce concerns about accumulated damage. Finally, several simplifying assumptions were made in the described methods of using measured strains to estimate internal bone loads during impact tests. These simplifications may have contributed to the poor results reported, and any further work on these methods should take a closer look at how acceptable the assumptions are.

5.3 Future Directions

Previous investigations into lower leg injury tolerance that take posture into account have identified contact area between the talus and tibial plafond as a potential factor in injury risk. In real life crash events, the complex mechanics of the ankle joint

likely play a role in load dissipation and transmission. Therefore, now that the effects of posture on injury risk in the isolated tibia have been quantified, it should be easier to analyse injury in experiments also incorporating an intact fibula and ankle. This would also ensure that contact at the ankle was realistic. The test apparatus used for this work was designed to be versatile, and would be able to accommodate these larger and more complex specimens.

The test apparatus is also capable of producing impacts at higher velocities and shorter impact durations than were used in this study, which would allow for the expansion of this work into a military application (with the impacts representing an in-vehicle mine blast). The MIL-LX legform was developed specifically for this application, and therefore its posture-specific response should also be evaluated under military-focused test conditions.

The evaluated methods for estimating internal bone loads rely heavily on the proper alignment of strain gauges relative to an anatomical coordinate system, and the alignment of the specimen by this system within the CT scanner. The design and construction of a fixture specifically for keeping alignment consistent may be necessary in future attempts to improve this method. Additionally, the use of more strain gauges (either through rosettes or simply a higher number of uniaxial gauges) may improve accuracy by providing more data points from which calculations can be made and compared. It may also be worthwhile to replace strain gauges entirely with high speed digital image correlation, a non-contact method for measuring full-field strain measurements.

5.4 Significance

This work represents the first quantification of the isolated tibia's posture-specific response to dynamic off-axis loading. New guidelines for predicting injury risk have been suggested, and two commonly-used ATDs have been evaluated in non-standard postures. A method for estimating internal bone loads during complex dynamic loading based on strain data has been described in detail, including an analysis of its strengths and weaknesses, which should be useful to anyone looking to continue this line of investigation. The experimental apparatus developed for this work is highly versatile, and may be used to conduct further studies into injury tolerance for other types of specimens in a wide variety of postures. It is hoped that the results of this work will allow for the more rigorous design and evaluation of protective devices in automobiles, ultimately leading to a reduction in debilitating lower leg injuries.

Appendix A: Glossary of Anatomical Terms

anterior	Towards the front of the body
Achilles tendon	Tendon at the back of the leg and heel, allowing plantarflexion at the ankle
articulation	The formation of a joint
cadaveric	Of, or pertaining to, a dead body
cancellous bone	Porous, lattice-like tissue that is found at the ends of long bones
cortical bone	Dense, rigid tissue that forms the outer shell of long bones
diaphysis	The hollow shaft of a long bone, made of cortical bone
distal	Further away from the centre of the body
dorsiflexion	Motion of the ankle caused by lifting the toes upwards
epiphysis	The rounded end of a long bone, made of cancellous bone surrounded by a cortical shell
fibula	The smaller of the two long bones that make up the lower leg
frontal plane	Plane dividing the front and back of the body
in situ	Translates to "on site", in this context meaning placed within an anatomical structure
in vivo	Translates to "within the living", meaning taking place within a living organism
inferior	Towards the feet
lateral	Away from the body's midline
malleolus	Bony projection on either side of the ankle
medial	Towards the body's midline
plafond	The distal articular surface of the tibia, which articulates with the talus at the ankle

plantarflexion	Motion of the ankle caused by pointing the toes downwards
posterior	Towards the back of the body
proximal	Closer to the centre of the body
saggital plane	Plane dividing the medial and lateral sides of the body
shank	The portion of the lower extremity between the knee and ankle
superior	Towards the head
talus	The ankle bone lying inferior to the tibia and fibula
tibia	The larger of the two long bones that make up the lower leg
tibial plateau	The proximal articular surface of the tibia, which articulates with the femur at the knee

Appendix B: Apparatus Standard Operating Procedure

Name of SOP	Pneumatic Impactor Operation
Effective Date	September 28, 2015
Author	Avery Chakravarty
Reason for SOP	[x] Procedure/Process could cause critical injury . [x] Procedure/Process could cause occupational illness [ ] Procedure/Process could cause environmental impairment . [x] Procedure/Process could damage University property [ ] Not critical, but requesting a review Provide Details: Procedure involves pneumatically accelerating a projectile down a tube. While the projectile is restrained from exiting the tube, there is potential for injury to operator should it misfire while they are setting up a specimen (as it protrudes a few inches) or if they are not wearing hearing protection; any malfunction of the high pressure system could also cause damage to the surrounding lab equipment.
Approved by (supervisor)	Cheryl Quenneville
Date reviewed by JHSC	October 14, 2015
Date Last Reviewed	October 14, 2015

Definitions

Terms	Anthropomorphic Test Device (ATD): a device designed to act as a surrogate for human body parts during high impact testing, especially car crash tests
Acronyms	RMM – Risk Management Manual JHSC – Joint Health and Safety Committee

Requirements

Applicable OHSA regulations and / or codes of practice. 1. RMM #101 - McMaster University Risk Management System
Training and Competency 1. Biosafety Level 1 (required for lab access) 2. EOHSS Asbestos Awareness 3. EOHSS Chemical Handling and Spills 4. EOHSS Fire Safety 5. EOHSS Health and Safety Orientation 6. EOHSS Machine Guarding 7. EOHSS Slips, Trips, and Falls 8. EOHSS WHMIS Core 9. EOHSS Lockout/Tag Out All persons working with the apparatus should speak to the lab supervisor for equipment-specific training

Description of the Task

Location and time of work	Biomechanics Lab (ETB 428); testing may occur at variable times but usually will be during normal business hours
Individuals involved	Supervisors and graduate students working with the pneumatic impactor
Equipment and supplies required	Impactor apparatus and associated components
Personal protective equipment required	Standard biohazard (level 1) lab PPE: gloves, lab coats, long pants, closed-toed shoes Equipment-specific PPE: hearing protection (pending EOHSS approval)

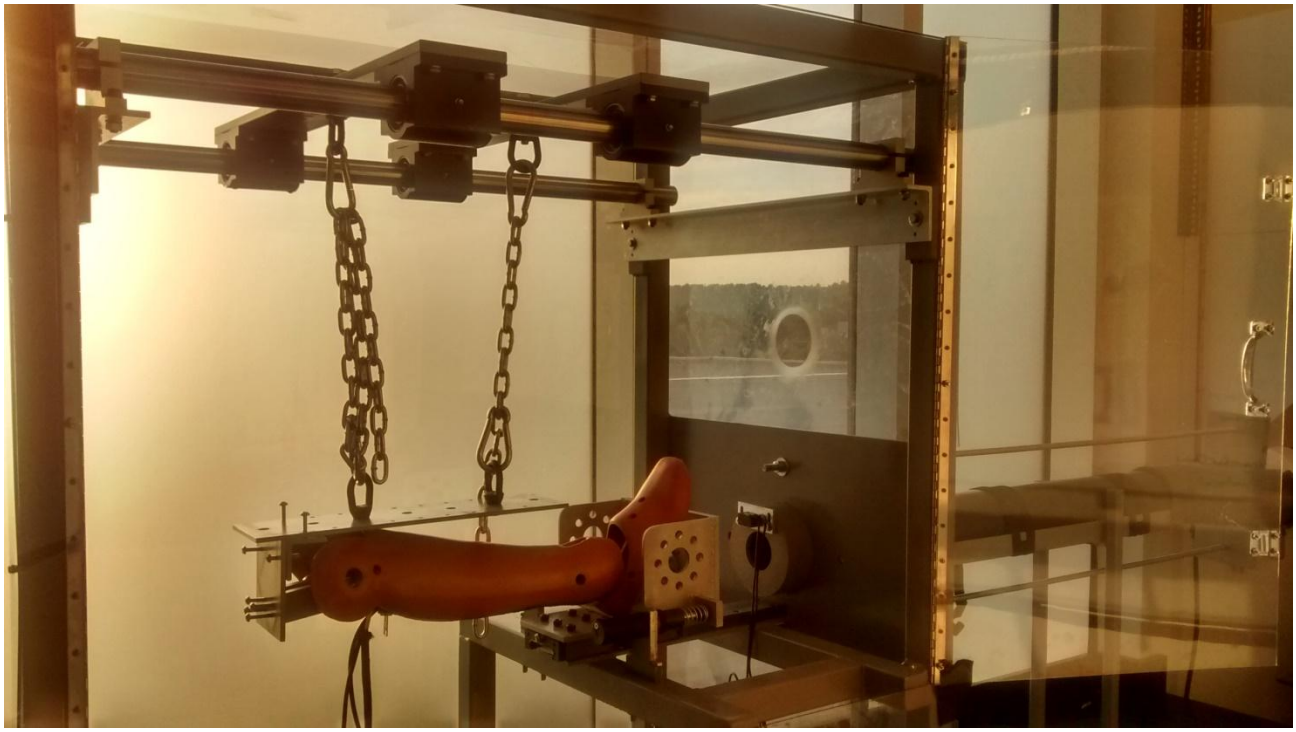

Figure B-1: Overall View of the System, with a Specimen Installed

Sequential Steps to Complete the Work Safely

1. *General Safety*
   - 1.1 When testing is not in process, the system should be completely de-energised (see step 7) and the test chamber doors must be closed and locked.
   - 1.2 All testing should be done with at least two people present.
   - 1.3 Anyone handling cadaveric specimens should be wearing gloves, a lab coat, long pants, and closed-toed shoes, as per biosafety guidelines (see RMM # 600).
   - 1.4 Anyone in the lab while the impactor is in use should have access to hearing protection, and hang a sign up on the outside of the door indicating that testing is in process and hearing protection is required. The sign will be kept inside the lab when not in use.

2. *Preliminary Inspection*
   - 2.1 Prior to testing, all researchers must conduct a brief inspection of the system for cracks in the structural and pneumatic elements, debris from specimens left in the test chamber, and any other irregularities.

3. *Installing the Specimen*
   - 3.1 a) Cadaveric bone specimens will be potted with cement inside 4-inch PVC pipe sections. These pipe sections will fit inside a custom-designed bracket,

held in place by four set screws (see Figure B-2). Before testing, the operator must ensure that that these set screws are tightened using a hex key until the pipe is rigidly secured. If a specimen is to be used for multiple impacts, the user must ensure that the set screws have not loosened between tests due to vibrations.

b) An alternative to testing bones is the testing of Anthropomorphic Test Device components (ATDs). The exact model will vary based on the body part represented and the style of loading being used. Custom-designed brackets will be used to support the ATDs within the enclosure. As an example, see Figure B-3. The bracket has two holes allowing for bolted connections with the ATD parts. The user of the system should verify that the bolted connection (if using this or a similar style of bracket) is tight, and the tightness should be verified between impact tests to protect against loosening from vibrations.

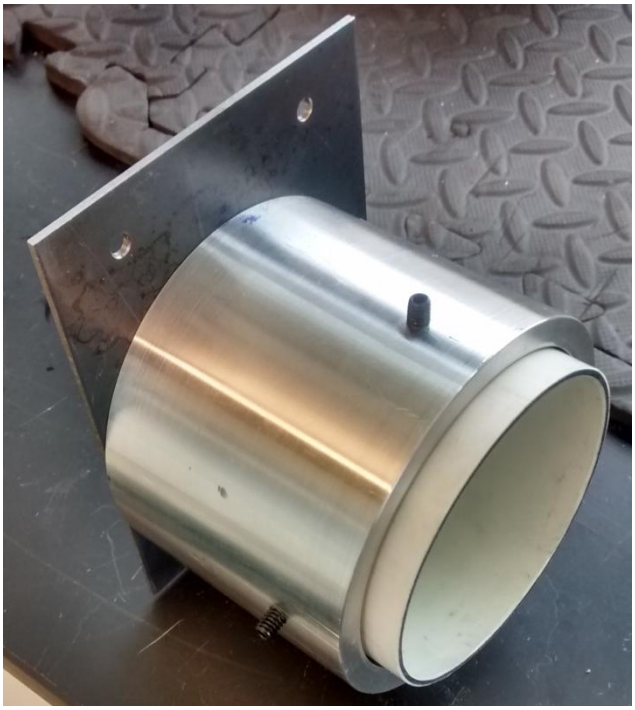

Figure B-2: A Close-Up View of the Cadaveric Specimen Bracket with a 4" PVC Section Secured in Place

Figure B-3: A Close-Up View of an Example ATD Bracket

3.2 Once the specimen to be tested is fixed in place, the mounting bracket will be bolted to a long steel attachment plate, shown in Figure B-4. There is a carabiner connected to an eye bolt at each end of the plate, and these carabiners can be used to attach the specimen and bracket assembly to the overhead suspension chains inside the test chamber. If it is necessary to change the posture of the specimen within the test chamber, the lengths of the suspension chains can be varied by clipping the carabiners into different links.

3.3 It may also be necessary to adjust the specimen's angle in the horizontal plane. To do this, change the orientation of the specimen support system relative to the secondary angle adjustment plate, shown in Figure B-5. The figure shows the configuration for holding a specimen in a neutral angle within the horizontal plane, with the specimen support system connected to the secondary angle adjustment plate by the central hole. Before making a change to the angle, remove the specimen and unclip the carabiners leading to the specimen support system. Once the hardware has been removed, undo the hex bolt and eye nut attaching the central plate to the secondary angle adjustment plate. Line a hole on the central plate up with another hole on the secondary angle adjustment plate that provides the desired angle, then refasten the hex bolt and eye nut and reattach the specimen support hardware.

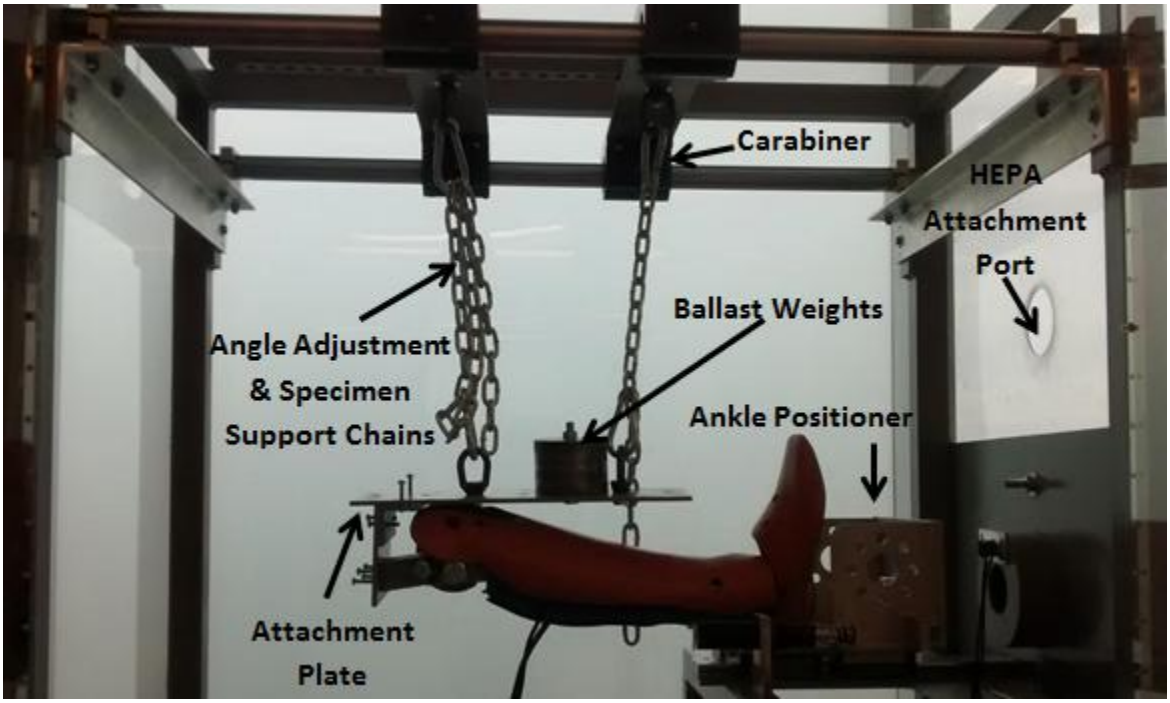

Figure B-4: An ATD Component Suspended in the Test Chamber

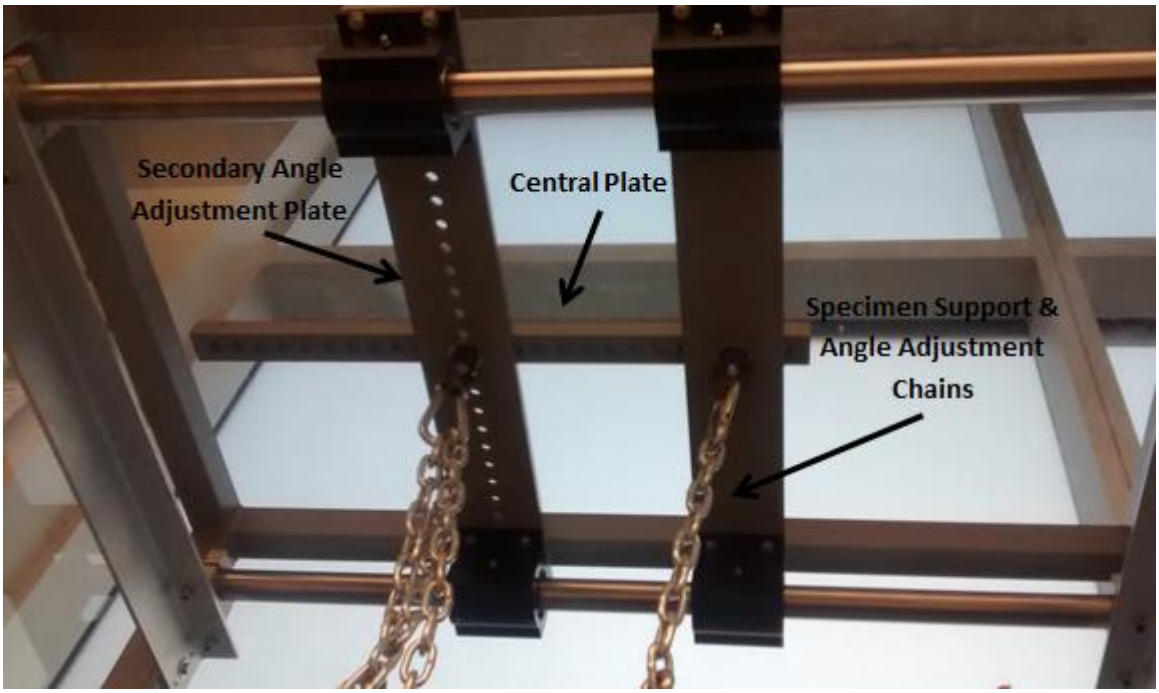

Figure B-5: Horizontal Angle Adjustment

3.4 It may also be necessary to add mass to simulate the inertia of other body parts. This may be done by fixing disc weights to the attachment plate. To do this, insert a long hex bolt through one of the central holes in the attachment plate, slip the desired number of weights onto the bolt's shaft, and a hex nut may be used to secure the weights in place. These ballast weights are identified in Figure B-4.

3.5 The ankle positioner must then be moved back against the projectile's entrance point to the test chamber to ensure that the projectile can make contact with it. Next, use the suspension chains and the overhead linear bearings to slide the specimen and its attached bracket so that it rests against the ankle positioner.

3.6 Instrumentation (including strain gauges, accelerometers, etc) will be mounted on specimens prior to testing. Thread the wires from these instruments through one of the ports in the test chamber shielding (see Figure B-6) and make the appropriate connections to the data acquisition system.

3.7 Place a drop sheet on the bottom of the test chamber to catch debris.

3.8 Once the specimen is securely supported, close the test chamber doors and lock them by closing a padlock through one hasp and clipping a carabiner through the other, as shown in Figure B-7.

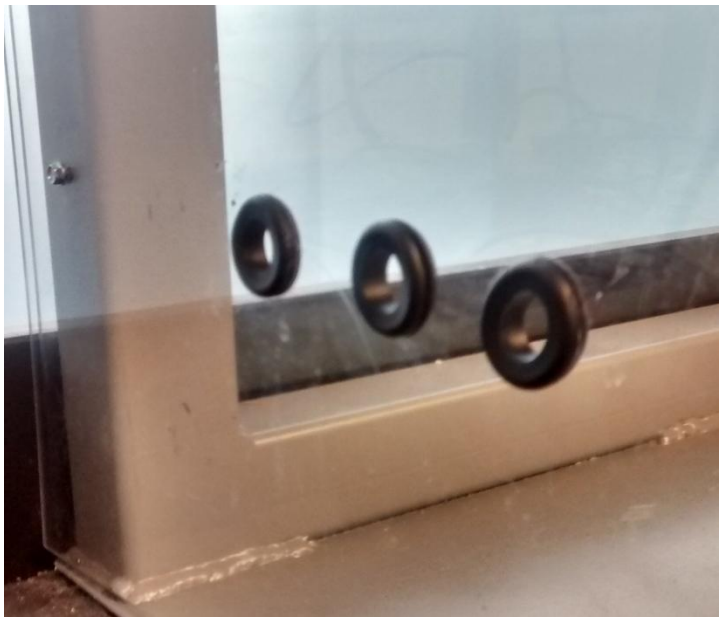

Figure B-6: Wire Ports in Back of Test Chamber

Figure B-7: Test Chamber Doors Secured with a Padlock

4. *Loading the Projectile*

4.1 The projectile is designed so that its mass can be varied based on the desired impact magnitude. To assemble the projectile, refer to Figure B-8. Screw the projectile head onto one end of the threaded rod, then slide one stabilising washer and the required number of disc weights from the other end and secure them in place with a hex nut. The second stabilising washer (which is attached to the extraction rope) can then be secured in place at the tail end with two hex nuts, and must be located at the end of the rod for the projectile to be stable. Once the projectile is secured to the desired mass, the projectile can be inserted into the acceleration chamber by removing the projectile-bay cap. (If the projectile has been loaded to a high mass, care must be taken to ensure that the projectile is lifted safely. A lab supervisor may be notified of any ergonomic concerns.) Figure B-9 shows the projectile loading bay, the inlet for compressed air ("Pressure In"), and the far end of the acceleration tube.

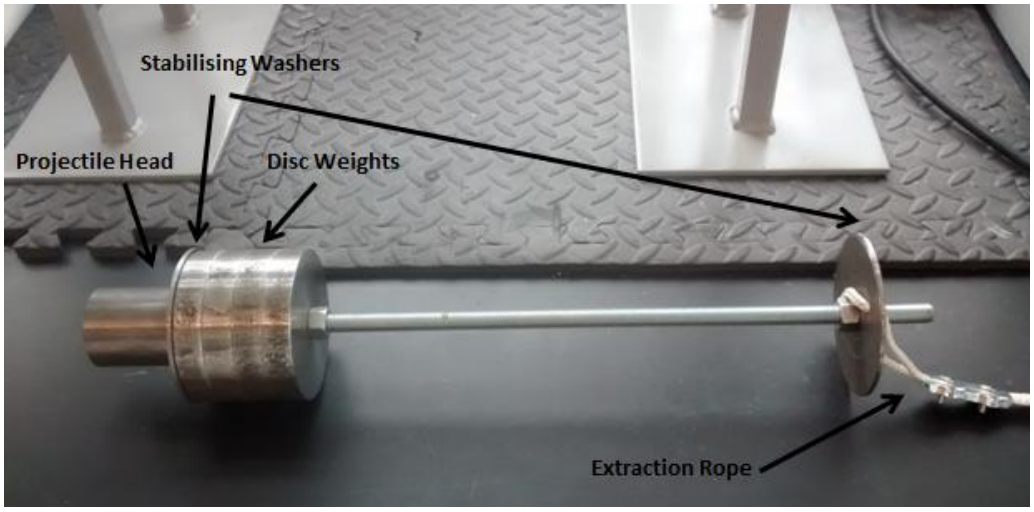

Figure B-8: Assembled Projectile with Various Components Identified

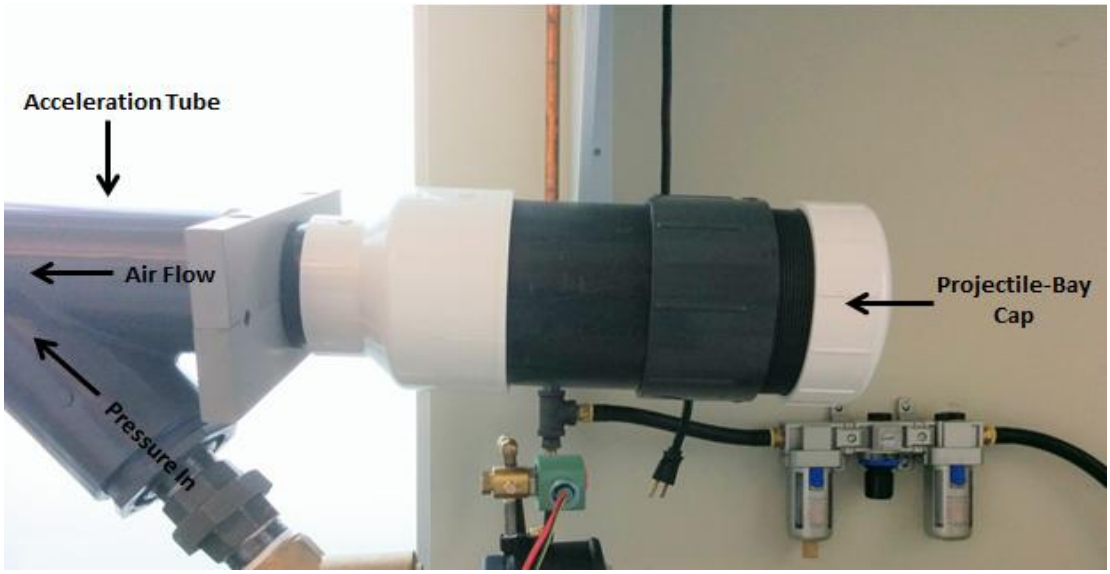

Figure B-9: A Close-Up View of the Projectile Extraction System Showing the Direction of Air Flow Down the Acceleration Tube

4.2 The projectile is then inserted into the projectile-bay door and positioned to the set starting distance using a laser distance measure. Screw the end cap on tightly to seal off the acceleration tube with the tethering extraction rope tucked neatly inside. The user must check that the rope is not tangled or knotted, which may impede the projectile's travel.

5. *Energising the System*

5.1 There are several valves required for the operation of the system, which have been identified in Figure B-10. Ensure ball valve #4 is closed before starting to fill the tank. Then open ball valves #1, #2, and #3 to begin energising the system.

5.2 Based on the calibration curve, manually select the desired air pressure by twisting the knob on the bottom of the regulator. The maximum allowable pressure of the regulator is 100 psi. Air pressure in the tank is monitored using the digital gauge attached to the tank's top port. When adjusting the tank pressure, allow time for the pressure to stabilize between adjusting the knob and reading the pressure off the digital gauge.

5.3 The electrical panel needs to be turned on. First, make sure it is connected to the solenoid valve by the three banana jacks called out in Figure B-11. Using the key kept in the drawer labelled "Impactor" located in the lab bench below the data acquisition system, turn the lock in the electrical panel to the "On" position. The green light will turn on. The solenoid valve is normally closed, and requires a 5VDC signal to trigger.

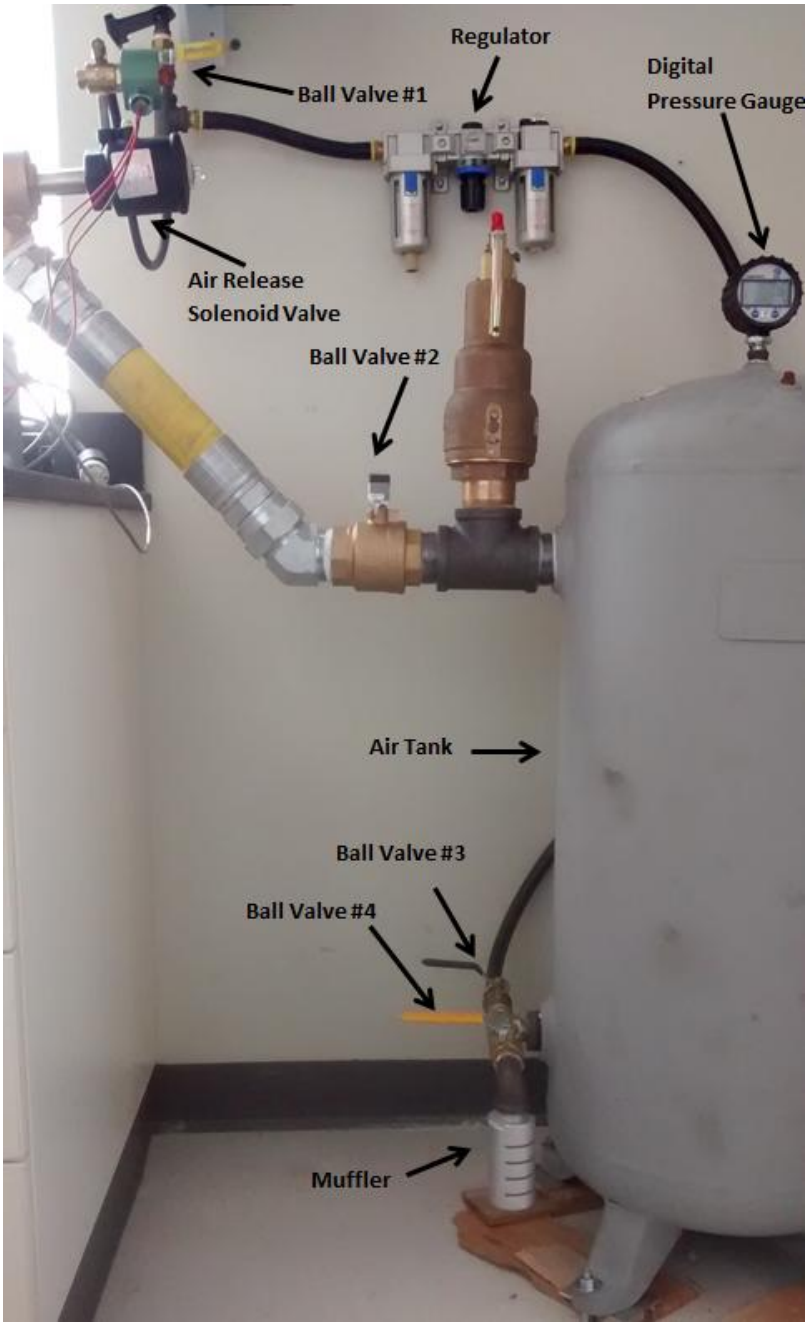

Figure B-10: Pneumatic System Main Components

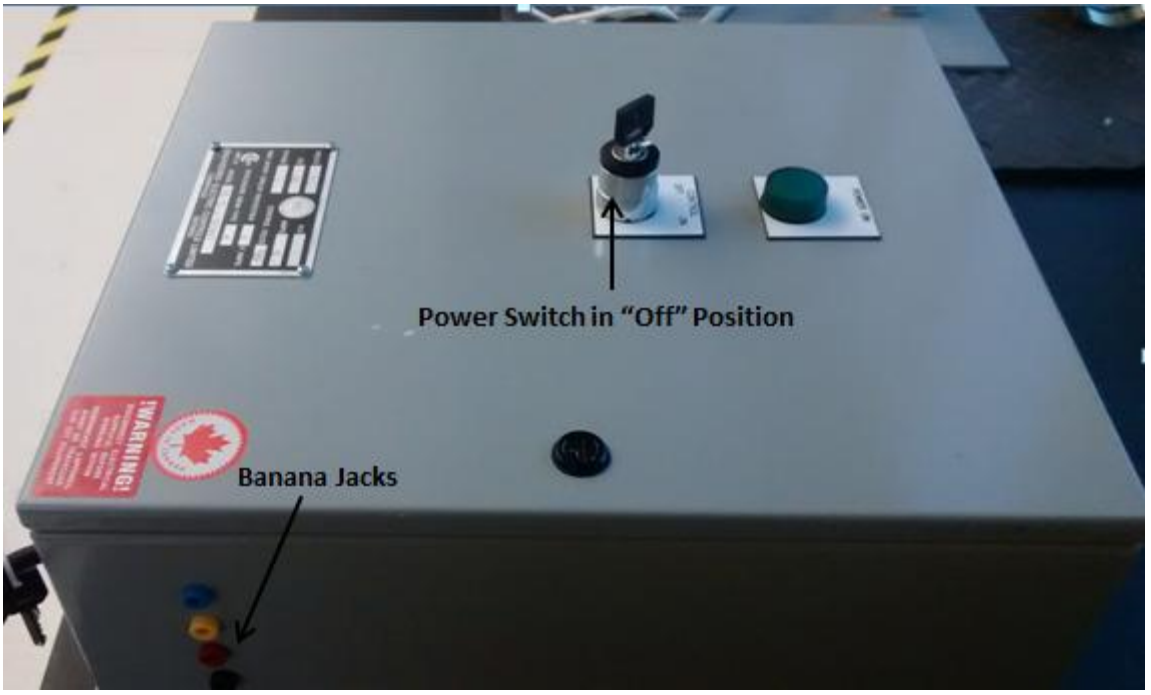

Figure B-11: Electrical Panel

6. *Setting up the High-Speed Camera*
   - 6.1 The high-speed camera is stored with its lens in the drawer labelled "High-Speed Camera" located in the lab bench below the pneumatic impactor test chamber.
   - 6.2 In order to setup the high-speed camera, first attach the lens to the camera body. The tripod is located on the second level lab shelves across from the pneumatic impactor test chamber. The camera can be mounted to the tripod and the power, trigger, and acquisition cables can be connected.
   - 6.3 Open the Fastec FasMotion software to begin acquisition from the camera.

7. *Firing the System*
   - 7.1 When working with cadaveric specimens, ensure that the HEPA filtration system is attached via hose to the test chamber and is running before firing the system. The attachment port has been called out in Figure B-4, and the filtration system can be seen in Figure B-12.
   - 7.2 All persons who are in the lab during impact testing must stand away from the lab bench, behind the safety tape on the floor (see Figure B-13). Only the operator of the data acquisition system may stand at the lab bench to operate the computer.
   - 7.3 Ensure that all people in the lab during testing are wearing hearing protection before firing.

Figure B-12: HEPA Filtration System

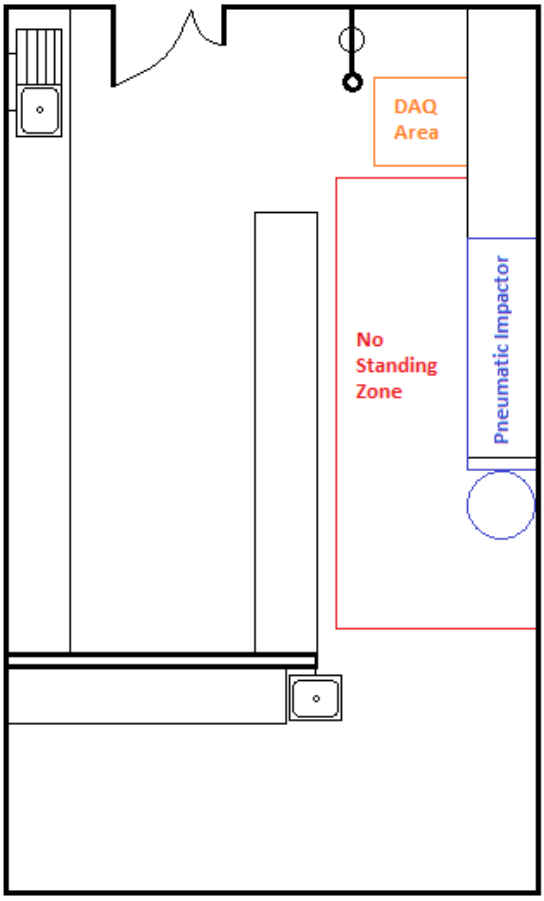

Figure B-13: Lab Floor Plan with "No Standing" Zone Identified

7.4 The operator will loudly announce their intention to trigger the solenoid valve by loudly saying "Firing!" before each test.

7.5 The operator of the data acquisition system will open Solenoid Valve Trigger Signal.vi from the desktop. Pressing the run button will generate a sine signal of voltage, triggering the valve once. The generated signal will be displayed on the chart titled "Solenoid Valve Trigger Signal".

8. *Repeat Testing*

8.1 When performing multiple impacts within a single session, the electrical panel powering the solenoid valve must be switched and locked into its "off" position. The power to the panel must then be locked out, by unplugging it from the wall supply and placing a locking cover over the plug. A hasp will be used to allow all workers to apply a personal lock. This will ensure that the normally-closed valve controlling the release of air into the acceleration tube and test chamber will not accidentally fire while users are working with specimens or instruments inside the chamber.

8.2 Ensure that the specimen and ankle positioner are placed up against the end of the acceleration tube, and the projectile retracted to its desired position.

8.3 Check all bolted connections for looseness in between repeated tests, and tighten as needed.

8.4 When testing is complete, the system must be completely de-energised, as outlined below.

9. *De-energising the System*

9.1 After the impact, the system must be fully discharged. Reduce the regulator pressure as much as possible. Close ball valve #1and #3. Slowly and incrementally open ball valve #4 to discharge the stored air through the muffler. Care must be taken at this step because of the large volume of air to be discharged, so ensure that hearing protection is still being worn and that hands and feet are not between the muffler's exit end and the floor. The higher the pressure of air to be discharged, the more care that must be taken at this step.

9.2 When the air has been fully discharged from the tank (which will be indicated by a pressure reading of 0 psi on the digital pressure gauge), close ball valves #2, #3, and #4. Turn off the digital pressure gauge. Lock the electrical panel in the "off" position.

9.3 Clean the chamber of any particles from biological specimens using a10% bleach solution.

10. *Lock Out/Tag Out for Maintenance*

10.1 If maintenance is required on the system, then both pneumatic and electrical energy must be locked out. The panel controlling the solenoid valve will be locked out as described in section 8, and compressed air will be locked out at ball valve #1, using a plastic valve cover. All individuals performing maintenance will place a lock at each location and verify that the system cannot be re-energised before starting work, as per the Lock Out/Tag Out policy.

Contingency Plan and Reporting

Accident / injury response
Cease all testing in the event of an injury or accident. Notify a lab supervisor of any injuries and seek medical attention for any injuries. When it is safe to do so, lock out the compressed air, and shut off the electrical panel and data acquisition system.
In the Case of Serious/Critical Injuries
Dial 88 (from a campus phone) or 905-522-4135 (from a cell phone)

Equipment Malfunction
Cease all testing in the event of an equipment malfunction. Notify a lab supervisor, and if it is safe to do so, discharge the system, lock out the compressed air, and shut off the electrical panel and data acquisition system. Testing will resume when the necessary repairs or replacements have taken place.

Equipment Shutdowns
Cease all testing in the event of an equipment shutdown. Notify a lab supervisor, and if it is safe to do so, discharge the system, lock out the compressed air, and disconnect the power to the electrical panel and data acquisition system. Testing will resume when normal conditions have been reached again.

Environmental Responsibility

Waste disposal procedures: Follow biohazardous waste disposal guidelines (see RMM # 502 and # 600)

Building air quality: n/a

References

1. RMM #100 McMaster University Environmental Health and Safety Policy
2. RMM #300 Safety Orientation and Training Program
3. RMM #301 Standard Operating Procedures
4. RMM #324 Job Hazard Analysis Program
5. RMM #403 Noise Control and Hearing Protection Program
6. RMM #405 Ergonomics Safety Program
7. RMM # 502 Hazardous Waste Management Program
8. RMM #504 Compressed and Liquified Gases Safety Program
9. RMM #600 Biosafety Programme

Distribution

1. Faculty of Engineering JHSC (for review)
2. All personnel of the Injury Biomechanics Lab

Legal Disclaimer

The Standard Operating Procedures on this website are provided for the use of the McMaster University employee and/or student community. The procedures outlined in the above referenced document are intended to reflect best practices in this field; as such they are provided to the community for guidance and/or direction. However, these recommendations should not be construed as legal advice.

Appendix C: Pneumatic System Calibration Curves

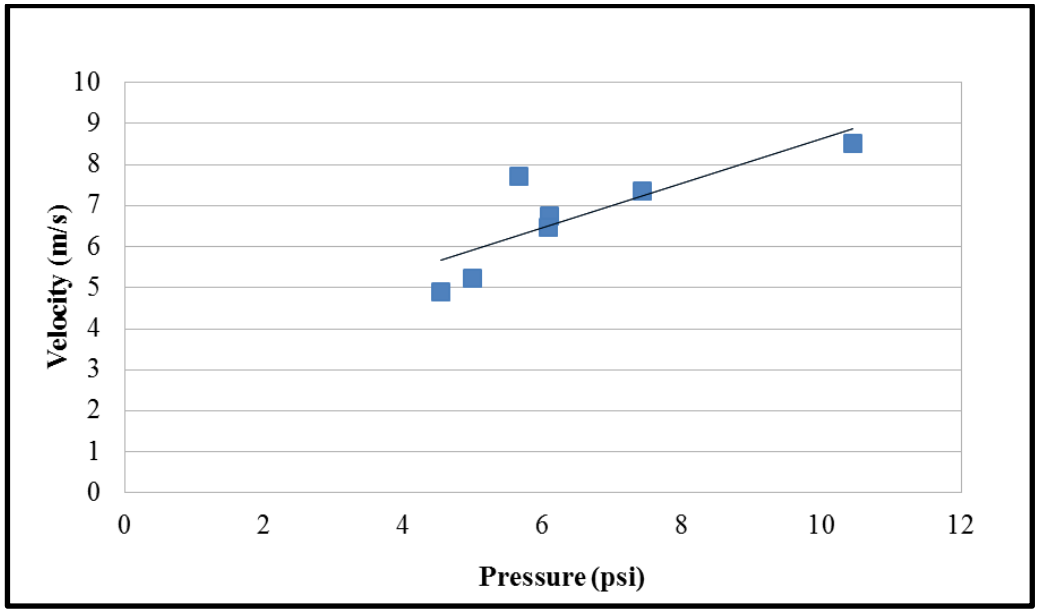

Figure C-1: Calibration Curve for 5.9 kg Mass.
$R^2 = 0.677$

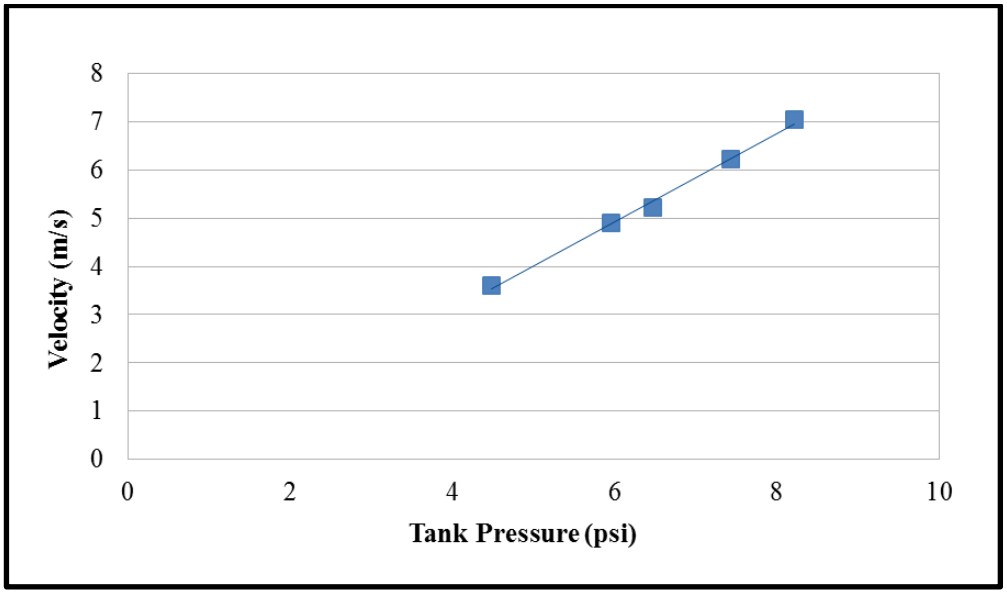

Figure C-2: Calibration Curve for 8.8 kg Mass
$R^2 = 0.996$

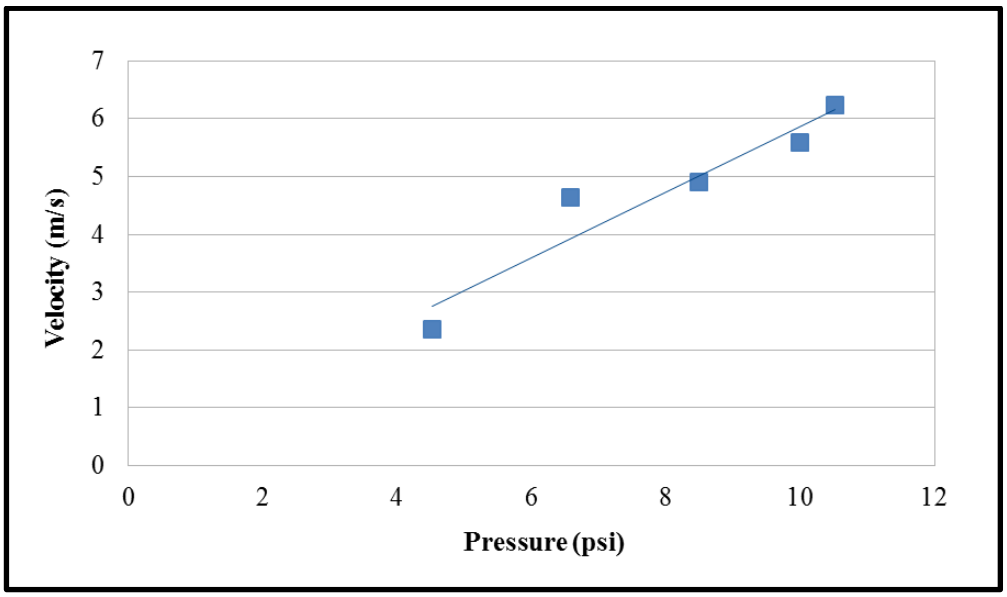

Figure C-3: Calibration Curve for 11.6 kg Mass
$R^2 = 0.913$

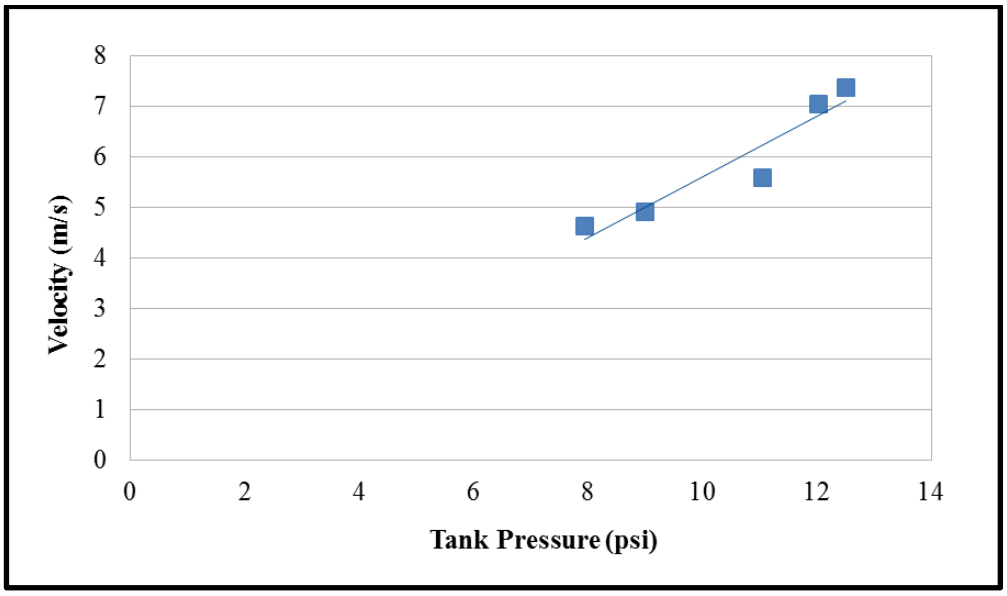

Figure C-4: Calibration Curve for 11.6 kg Mass
$R^2 = 0.900$

Appendix D: Specimen Information

Table D-1: Specimen Information

Age, potted mass, and length of the intact tibia are listed for each specimen.

Donor	Age (years)	Right/Left	Potted Specimen Mass (kg)	Tibia Length (m)
1523	69	R	1.41	0.37
		L	1.46	0.36
1547	48	R	1.51	0.37
		L	1.49	0.37
1553	70	R	1.43	0.37
		L	1.45	0.38
1582	53	R	1.50	0.36
		L	1.53	0.38
1640	73	R	1.45	0.37
		L	1.44	0.37
1653	71	R	1.41	0.40
		L	1.51	0.39

Appendix E: Drawings

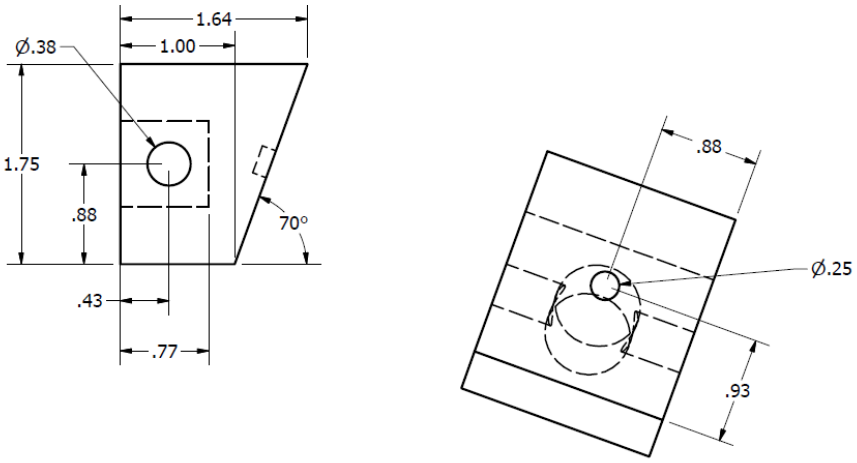

Figure E-1: Acrylic Wedge for Low-Angle ATD Tests
All dimensions in inches.

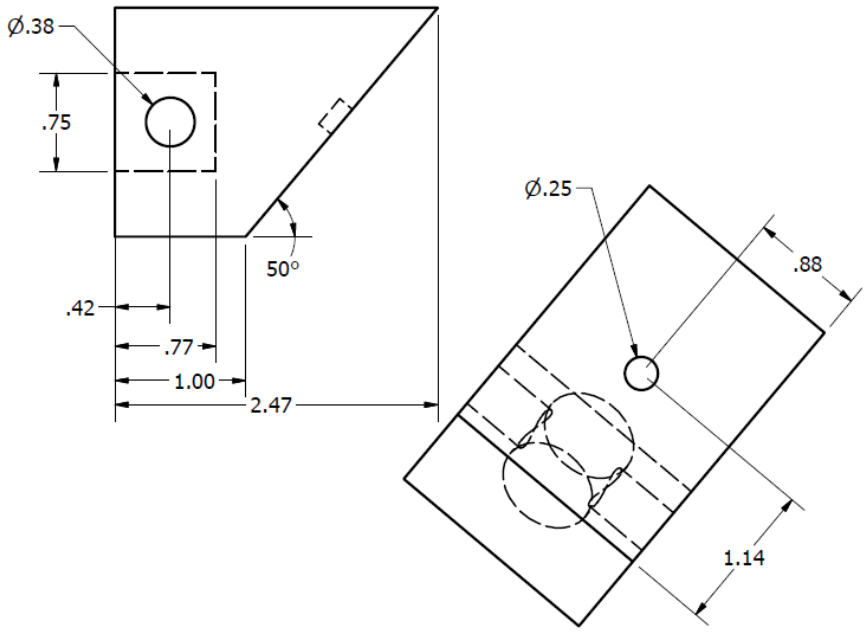

Figure E-2: Acrylic Wedge for High-Angle ATD Testing
All dimensions in inches.

Appendix F: Principal Strains

Table F-1: Principal Strains Gathered in Fracture Impact Tests
Values taken from strain gauge rosettes were used to calculate principal strains for each specimen's impact test resulting in fracture.

Specimen	Leg Angle (°)	Distal – 1st Principal Strain (Microstrain)	Distal – 2nd Principal Strain (Microstrain)	Proximal – 1st Principal Strain (Microstrain)	Proximal – 2nd Principal Strain (Microstrain)
1653R	15	490948	-80683	1103	-35563
1653L	30	624839	-243838	2030	-1579
1640R	30	1057	-3740	1368	-1031
1640L	15	n/a	n/a	n/a	n/a
1547R	30	746	-2885	1620	-1270
1547L	15	4624	-11140	230940	-283279
1582L	15	n/a	n/a	662	-1957
1582R	30	n/a	n/a	1853	-3091
1523R	15	n/a	n/a	1230	-3697
1523L	30	n/a	n/a	n/a	n/a
1553R	15	n/a	n/a	1082	-3466
1553L	30	n/a	n/a	n/a	n/a
Mean for 15° Leg Angle (SD)		**247786 (343883)**	**-45911 (49175)**	**47003 (102824)**	**-65592 (122505)**
Mean 30° Leg Angle (SD)		**208881 (360231)**	**-83488 (138868)**	**1718 (287)**	**-1743 (926)**

Table F-2: Principal Strains Gathered in Pre-Fracture Impact Tests
Values taken from strain gauge rosettes were used to calculate principal strains for each specimen's impact test preceding fracture.

Specimen	**Leg Angle (°)**	**Distal – 1st Principal Strain (Microstrain)**	**Distal – 2nd Principal Strain (Microstrain)**	**Proximal – 1st Principal Strain (Microstrain)**	**Proximal – 2nd Principal Strain (Microstrain)**
1653R	15	2131	-6484	1298	-4150
1653L	30	233336	-285807	2258	-2379
1640R	30	2082	-7238	1048	-2820
1640L	15	n/a	n/a	n/a	n/a
1547R	30	846	-3376	654	-1894
1547L	15	1231	-3392	1405	-2925
1582L	15	n/a	n/a	1115	-3115
1582R	30	n/a	n/a	828	-2492
1523R	15	n/a	n/a	2927	-3762
1523L	30	n/a	n/a	n/a	n/a
1553R	15	n/a	n/a	1185	-3645
1553L	30	n/a	n/a	n/a	n/a
Mean for 15° Leg Angle (SD)		**1681 (636)**	**-4938 (2186)**	**1586 (758)**	**-3519 (497)**
Mean 30° Leg Angle (SD)		**78755 (133873)**	**-98807 (161958)**	**1197 (726)**	**-2397 (383)**

Appendix G: Geometric Data from CT Scans

Table G-1: Summary of Geometric Data Obtained From CT Scans

Geometric properties taken from each specimen used for load estimation. All data taken from slices corresponding to the location of applied strain gauges. Values obtained from ImageJ software (National Institutes of Health, Bethseda, MD, USA) using BoneJ plugin version 1.4.0.

Specimen	**Cross-Sectional Area, A_{CS} (mm^2)**	**Area moment of inertia about AP axis, I_{AP} (mm^4)**	**Area moment of inertia about ML axis, I_{ML} (mm^4)**	**Angle of ML Axis Relative to ImageJ's Coordinate System (°)**
1523L	284.5	8244.5	9504.3	12
1523R	306.4	8401.0	11612.3	333
1553L	243.1	5851.2	8732.1	211
1553R	284.5	7433.582	11534.431	57